Image Guidance in Cardiac Electrophysiology

by

Zachary John Malchano

Submitted to the Harvard-MIT Division of Health Sciences and Technology
in partial fulfillment of the requirements for the degree of

Master of Engineering in Biomedical Engineering

at the

MASSACHUSETTS INSTITUTE OF TECHNOLOGY

June 2006

Author .....
Harvard-MIT Division of Health Sciences and Technology
May 18, 2006

Certified by .....
Vivek Y. Reddy
Instructor in Medicine, Harvard Medical School
Cardiac Arrhythmia Unit, Massachusetts General Hospital
Thesis Supervisor

Certified by .....
William M. Wells, III
Associate Professor of Radiology, Havard Medical School
Surgical Planning Laboratory, Brigham and Women's Hospital
Thesis Supervisor

Certified by .....
W. Eric L. Grimson
Bernard Gordon Professor of Medical Engineering
Department Head, Electrical Engineering and Computer Science, MIT
Thesis Supervisor

Accepted by .....
Martha L. Gray
Edward Hood Taplin Professor of Medical and Electrical Engineering
Director, Harvard-MIT Division of Health Sciences and Technology

Image Guidance in Cardiac Electrophysiology

by

Zachary John Malchano

Submitted to the Harvard-MIT Division of Health Sciences and Technology
on May 18, 2006, in partial fulfillment of the
requirements for the degree of
Master of Engineering in Biomedical Engineering

Abstract

Cardiac arrhythmias are characterized by a disruption or abnormal conduction of electrical signals within the heart. Treatment of arrhythmias has dramatically evolved over the past half-century, and today, minimally-invasive catheter-based therapy is the preferred method of eliminating arrhythmias. Using an electroanatomical (EA) mapping system, which precisely tracks the position of catheters inside the patient's body, it is possible to construct three-dimensional maps of the ventricular and atrial chambers of the heart. Each point of these maps is annotated based on bioelectrical signals recorded from the electrodes located at the tip of the catheter. These maps are then used to guide catheter ablation within the heart. However, the electroanatomical mapping procedure results in relatively sparse sampling of the heart and a significant amount of time and skill are require to generate these maps.

In this thesis, we present our software system for the integration of pre-operative, patient-specific magnetic resonance (MR) or computed tomography (CT) imaging data with real-time electroanatomical mapping (EAM) information. Following registration between the EAM and imaging data, the system allows allows for real-time catheter navigation within patient-specific anatomy. We then evaluate candidate registration strategies to rapidly and accurately align the pre-operative imaging data with the intra-operative mapping data using simulated electroanatomical mapping data using the great cardiac vessels including the aorta, superior vena cava, and coronary sinus. Based on these *in vitro* results, we focus on a registration strategy which is constrained by the ascending and descending aorta. *In vivo* prospective evaluation of the resulting image integration was then performed (n>200) in both experimental and clinical electrophysiology procedure. To compensate for residual error following registration or patient movement during a procedure, we present and evaluate warping strategies for deforming the pre-operative imaging data into agreement with the intra-operative mapping information.

Thesis Supervisor: Vivek Y. Reddy
Title: Instructor in Medicine, Harvard Medical School
Cardiac Arrhythmia Unit, Massachusetts General Hospital

Thesis Supervisor: William M. Wells, III
Title: Associate Professor of Radiology, Havard Medical School
Surgical Planning Laboratory, Brigham and Women's Hospital

Thesis Supervisor: W. Eric L. Grimson
Title: Bernard Gordon Professor of Medical Engineering
Department Head, Electrical Engineering and Computer Science, MIT

Acknowledgments

During my time in Boston, I have been very fortunate to work and learn at MIT, HMS, and MGH. An extremely vibrant community of both medicine and engineering exists at these institutions, and I have greatly enjoyed my time working at the boundary between these disciplines. I would like to thank the numerous people who were instrumental in my work for the past four years. I am especially grateful to Vivek Reddy for his continued support of my research. His energy, enthusiasm, and guidance have been invaluable in my quest to understand medicine from an engineer's perspective. Sandy Wells, Eric Grimson, and Jeremy Ruskin have always been extremely helpful throughout my experience. They have continually supported my work, encouraged my exploration of new areas and new ideas, and been available to answer my questions both about my research and my future.

The Cardiac Arrhythmia Unit at Massachusetts General Hospital and the Cardiostimulze at Homolka Hospital in Prague, Czech Republic, were fantastic environments in which to have learned about medicine and conducted my research. I am very grateful to the staff at both locations for their eternal patience with the continued evolution of my software.

I am also very thankful to my collaborators in the many disciplines of engineering and medicine which this research spanned. I would especially like to thank my collegues at MGH, MIT, Homolka including Petr Neuzil, Ray Chan, Ehud Schdmidt, Andre d'Avila, Fred Holmvang, Stepan Kraolec, Ricardo Cury, Ragu Vijaykumar, Nimi Ocholi, Robert Mankze, and the Medical Vision Group at CSAIL. I would like to thank Rob Pike of Biosense-Webster for his early and continued support of my work. Futhermore, I am grateful to many individuals from GE Healthcare and GE Glocal Research including Ehud Schmidt, Harvey Cline, Rich Mallozzi, Bill Lorenson, Renee Ghude, and their collegues at GE Global Research for providing valuable assistance to me in the form of VTk answers and software including Cardiac++.

My time at MIT has been greatly enhanced by all of my friends. Thank you all for getting me away from my work.

Finally, this thesis is dedicated to my family - Mom, Dad, and Matt for their love and support throughout the years.

Contents

List of Figures

List of Tables

Chapter 1

Introduction

1.1 Motivation

Cardiac arrhythmias are a significant cause of morbidity and mortality in industrialized societies. Arrhythmias are characterized by abnormalities in electrical impulse formation or conduction within the heart [1]. These abnormalities disrupt the coordinated mechanical contraction and can result in reduced or insufficent cardiac output or other complications. Arrhythmias may or may not manifest clinical symptoms; however, clinical sequelae can be extremely serious including elevated risk of stroke, congestive heart failure, and/or sudden cardiac death. Even when clinical sequelae are non-fatal, arrhythmias are responsible for significant morbidity and healthcare cost. Current treatment options range from non-invasive, such as lifestyle modification and pharmaceutical therapy, to minimally- or highly-invasive, including catheter-based ablation, device implantation, and cardio-thoracic surgery. While non-invasive therapies can suppress the occurrence of arrhythmias and mitigate their secondary effects, these treatments have may significant side-effects, which make them less ideal for long-term patient management of arrhythmias. Interventional procedures remain the only method for *curing* a patient with an arrhythmia [1]. Minimally-invasive catheter-based procedures result in less operative trauma, cause less pain and scarring, and reduce hospitalization time and healthcare cost with success rates comparable to more traditional surgical methods [2]. Therefore, catheter-based radio frequency (RF) ablation of cardiac arrhythmias has become the preferred treatment by both patients and healthcare institutions.

However, the catheter-based treatment paradigm has matured only relatively recently

for complex arrhythmias such atrial fibrillation (AF) or ventricular tachycardia (VT). Treatment of these arrhythmias require extensive RF ablation within the heart, and treatment with the introduction of catheter-based, "electroanatomical mapping" (EAM) systems; these systems precisely track one or more "mapping" catheters within a patient's heart in real-time. The EAM systems record electrical information from electrodes on the catheter as well as record the position of RF ablation lesions. This information is then used to create a 3D map of the electrical characteristics of the heart and ablations applied to the heart (Figure 1-7). Under EAM guidance, the efficacy of catheter-based treatments now approaches surgical success rates. However, there are several limitations of the current EAM paradigm. First, catheter-based mapping is time intensive, and the resulting map is largely dependent on the skill and experience of the operator. Second, catheter mapping is a point sampling technique which results in a relatively sparse representation of the chamber(s) of interest within the heart. Finally, patient movement during an EAM procedure can result in significant disparity between pre-movement and post-movement EAM information, which requires the time-consuming remapping of the relevant cardiac chambers.

In the ideal situation, an electrophysiologist would have sufficent information to plan an appropriate treatment for each patient *prior* to an interventional procedure. For surgical planning, pre-operative magnetic resonance (MR) and computed tomography (CT) imaging can provide important, patient-specific, anatomical and physiological information. However, this information would be most useful if integrated directly in with the intra-procedural EAM data. The goal of this thesis is to develop and validate new methods for the rapid and accurate integration of pre-operative imaging data with intra-operative electroanatomical mapping information. The methods to be presented extend the capabilities of conventional catheter-based electroanatomical mapping so that reliable registration and image-guided catheter ablation of cardiac arrhythmias can be performed using patient-specific imaging information.

1.2 Pathophysiology of Cardiac Arrhythmias

A normal human heart can be thought of two pumps connected in series which are responsible for circulation of oxygenated blood throughout the body and circulating deoxygenated blood through the lungs so that gas-exchange can occur (Figure 1-1). Deoxygenated blood

enters the right atrium of the heart from the superior vena cava, the inferior vena cava, and the coronary sinus. This blood then passes the tricuspid valve into the right ventricle. Upon ejection from the right ventricle through the pulmonic valve, the blood enters the pulmonary circulation via the pulmonary artery. Within the lungs, gas-exchange occurs, and the oxygenated blood returns to the left atrium of the heart via the pulmonary veins. From the left atrium, the blood is then emptied through the mitral valve into the left ventricle. The muscular left ventricle then contracts to exceed the diastolic blood pressure at the aortic valve. When the isometric contraction exceeds this pressure, blood is ejected from the left ventricle into the systemic arterial circulation.

1.2.1 Cardiac Electrophysiology

The human heart has an intrinsic electrical conduction system which is responsible for synchronized contraction of the cardiac chambers and maintaining sufficient arterial blood pressure for the perfusion of the body. In a resting state, there is a potential difference across the cell membrane of myocytes resulting from an ion concentration difference. Ion channels and pumps span the cellular membrane to passively and actively maintain this difference between the intracellular and extracellular space. These cells have the ability to undergo a trasient depolarization and repolarization known as an action potential (AP), which can be triggered from external mechanisms or via spontaneous mechanisms. During depolarization, rapid efflux and influx of sodium, potassium, and calcium ions result in a net positive current out of the cell. Immediately following depolarization, repolarization occurs, and the ion channels and pumps re-establish the concentration gradients and therefore the potential difference acrss the cellular membrane.

In a normal heart, contraction is initiated by an action potential originating from the main pacemaker cells within the sinoatrial (SA) node located near the junction of the superior vena cava (SVC) and the right atrium (RA). This electrical impulse then spreads across the right and left atria, via gap junctions connecting individual myocardial cells (Figure 1-2). The coordinated excitation of the myocardial cells results in contraction of the atria. After a short delay in the Atrio-Ventricular (AV) Node, which permits optimal filling of the ventricles, the electrical impulse is conducted to the apical region of the ventricles via the Bundle of His and then the left and right bundles branches. Through excitation-contraction coupling, the impulse results in synchronized contraction of the left and right

Figure 1-1: Cardiac anatomy. (Plate 505 of [3])

ventricles, thereby propelling blood into the systemic and pulmonary arterial circulation.

Following a depolarization, a myocyte enters an absolute refractory period followed by a relative refractory period. During absolute refractory, an action potential cannot be elicited from the cell. When the cell is in relative refractory, an increased stimulus is required to depolarize the cell and initiate an actional potential. The refractory period can have an important role in the initiation and continuation of an arrhythmia, which will be explained further in the next section.

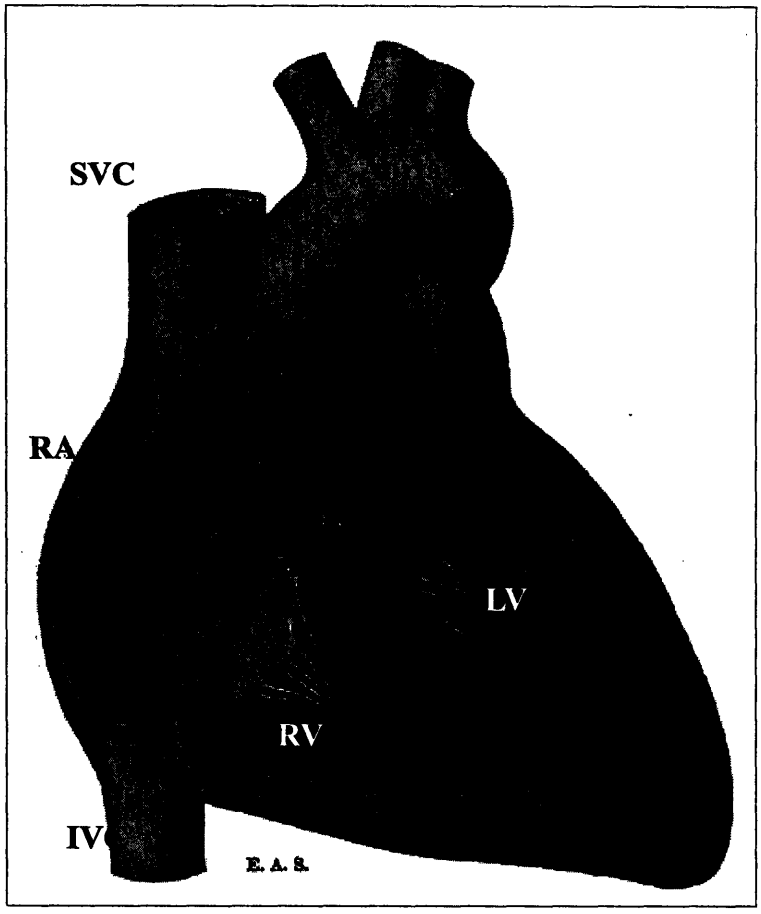

Figure 1-2: Cardiac conduction pathways of the heart. In a normal heart, cellular cautomaticity within the Sinoatrial (SA) node initiate an electrical cascade within the heart that results in synchronized mechanical contraction of the heart. The SA node is on the posterior aspect of the right atrium near the junction of the superior vena cava and the right atrium. From the SA node, the impulse spreads across the right atrium at a conduction velocity of approximately 1 m/s, and the impulse is conducted from the SA node directly to the left atrium via Bachmann's bundle (interatrial myocardial band). The atrioventricular (AV) node, in a normal individual, is the only route for the electrical impulse to reach the ventricles. At the cellular level, the AV node contains similar cells to the SA node, and in certain cases, it may assume the role of cardiac pacemaker for a diseased or damaged heart. At the AV node, there is a physiologically relevant conduction delay. The impulse is then conducted via the bundle branches and Purkinje fibers to the apical regions of the heart. These cells begin the mechanical contraction of the heart, and the electrical impulse is now conducted at a slower rate via gap junctions between cells (Plate 501 of [3]).

1.2.2 Pathogenesis of Arrhythmias

By disrupting the normal electrical conduction of the heart, arrhythmias may result in a significantly reduced efficiency of the heart and can lead to life-threatening side effects. Arrhythmogenic mechanisms are classified based broadly on the distinction between electrical impulse generation and impulse conduction (Table 1.1). The resulting cardiac arrhythmias can be divided into two categories based on heart rate: 1) bradyarrhythmias or bradycardias in which the heart rate is less than 60 beats per minute and 2) tachyarrhythmias or tachycardias in which the heart rate is in excess of 100 beats per minute for three beats or more. Bradyarrhythmias are most often treated with an implantable pacemaker described below.

Table 1.1: Arrhythmogenic Mechanisms (from [4])

Abnormal impulse initiation
Automaticity
Normal Automaticity
Abnormal Automaticity
Triggered Activity
Early afterdepolarizations
Delayed afterdepolarizations
Abnormal impulse conduction
Conduction block leading to ectopic pacemaker escape
Unidirectional block and reentry
Ordered reentry
Random reentry
Reflection

Tachyarrhythmias are the result of one of three mechanisms. They can be caused by increased or enhanced cellular automaticity, triggered activity, or unidirectional conduction block and reentry. Tachyarrhythmias are broadly divided into two categories based on the location of the arrhythmia. A supraventricular tachyarrhythmia (SVT) arises above the ventricles, while a ventricular tachycardia (VT) occurs within the ventricles. In general, a 12-lead electrocardiogram (ECG) can be used to accurately differentiate these types of arrhythmias based on several characteristics of the recorded bioelectrical signals. There are several distinct SVTs including sinus tachycardia, atrial premature beats, atrial flutter, ectopic atrial tachycardia, AV nodal reentrant tachycardia (AVNRT), and atrial fibrillation (AF or AFib).

The remaining portion of this dissertation will focus on two complex arrhythmias of great clinical importantce: atrial fibrillation and ventricular tachycardia.

1.2.3 Atrial Fibrillation

Atrial fibrillation is a cardiac arrhythmia which eliminates any coordinated contraction of the left atrium as a result of extremely high rate of excitation by multiple foci located within the pulmonary veins [5]. Over time, AF results in structural remodeling of the left atrium. Atrial fibrillation is a significant healthcare problem; it is the most common cardiac arrhythmia requiring treatment with an estimated prevalence of 2.3 million patients in the United States in 2001 [6]. In addition, the prevalence of atrial fibrillation increases with age; AF occurs in 3.8 percent of individuals over 60 years old and 9.0 percent of people 80 years of age and older [6, 7]. Although atrial fibrillation can be asymptomatic or "silent" in many patients, the consequences of the disease can be devastating. Thrombo-embolism from the left atrial appendage can result in a stroke or cerebral vascular attack (CVA). Of high-risk patents with atrial fibrillation who are only taking aspirin, incidence of stroke ranges from 5.0 percent to 9.6 percent per year [6, 8, 9].

In most patients, atrial fibrillation is associated with other etiologies such as cardiovascular disease, hypertension, coronary artery disease, cardiomyopathy, and valvular heart disease [6]. Cardiac surgery, myocarditis, pericarditis, and other factors are also considered predisposing factors for atrial fibrillation. Beyond the risk of stroke, atrial fibrillation eliminates so-called atrial kick which affects left ventricular filling. Therefore, patients with impaired left ventricular function from congestive heart failure can be further compromised.

Atrial fibrillation is classified into three types: 1) paroxysmal 2) persistent and 3) permanent or chronic atrial fibrillation. These classifications are based on the duration of the arrhythmia:

Paroxysmal Transiently occurring episodes of AF with spontaneous initiation and termination of the arrhythmia.

Persistent atrial fibrillation will continue until a treatment such as external cardioversion defibrillation is administered.

Permanent (chronic) cardioversion and drug treatments are ineffective in restoring a patient to sinus rhythm.

From an electrophysiology standpoint, atrial fibrillation is a complex and difficult disease to treat. It now has been shown by many studies that rapidly firing foci within the pulmonary veins are responsible for the spontaneous initiation of paroxysmal atrial fibrillation; however, treatment options are limited by patient safety concerns. There is a high-risk of stenosis following RF ablation of these foci deep within the pulmonary veins. Pulmonary vein stenosis or a narrowing of the pulmonary veins is a serious complication that 2-41 percent of patients who undergo ablation may develop [10]. Treatment of PV stensosi may require stenting or balloon dilatation. Relevant interventions to minimize paroxysms of atrial fibrillation, the risks associate with the disease, and the peri- and post-operative complications are discussed below (Section 1.3).

1.2.4 Ventricular Tachycardia

Cardiovascular disease remains the most common cause of death in developed countries around the world [11]. It is estimated that 50 percent of all deaths from cardiovascular causes are a result of malignant ventricular tachyarrhythmias [11]. In the setting of a prior myocardial infarction (MI), the predominate pathogenesis of ventricular tachycardia (VT) is reentry in the region of the scarred myocardium [12, 13]. The myocardial tissue can be divided into three types: dense scar tissue, healthy myocardial tissue surrounding the affected region, and the "border zone" at the interface between healthy and scarred myocardial tissue. It is important to think about these regions as a complex structure in three-dimensions; the border zone includes any interfaces between normal tissue and dense scar. In this border region, electrically-active myocardial fibrils are interspersed with the fibrotic scar tissue. These regions are characterized by abnormal electrophysiologic properties including slowed conduction velocity and decreased cell-to-cell coupling.

As with reentrant circuits in other locations within the heart, the self-perpetuating arrhythmia requires a unidirectional conduction block and a substrate with slow enough conduction to allow for recovery of the excitability of the initially blocked region (Figure 1-3). Once the reentrant circuit has been initiated, the cycle length of the wavelength of the tachycardia circuit must be short enough or the conduction pathway must be long enough so that the wavefront of the arrhythmia is always encountering excitable tissue.

Over the past decade, significant advances have been made in the treatment of ventricular tachyarrhythmias; however, they remain a clinical challenge. From a clinical standpoint,

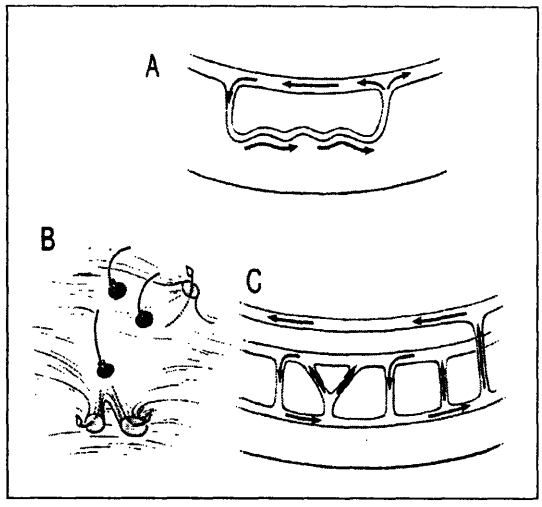

Figure 1-3: Extensive surgical mapping experience demonstrated a sheet of viable myocardial fibers located in the sub-endocardium (A) with multiple entrance and exit sites (B and C). While a single re-entrant circuit is all that is need for a sustained monomorphic ventricular tachycardia, the sub-endocardial network is a complex interdigitation of viable myocardial fibrials with scar tissue. This complex network can result in many morphologies of ventricular tachycardia, and it is also extremely difficult to map and treat in a clinical setting (Image reproduced from [13]
).

ventricular tachycardias can be broadly divided into two categories: stable and unstable. A "stable" VT refers to a hemodynamically tolerable state during the arrhythmia; however, with an elevated heart rate and decreased left-ventricular end diastolic filling time, the arterial pressure is often reduced. If the VT is stable, the reentrant circuit can be mapped during the arrhythmia; this mapping can be used to identify critical entrance, exit, and conduction sites which sustain the tachycardia. Likewise, an "unstable" VT refers to a hemodynamically intolerable VT during which arterial blood pressure is to low to ensure adequate perfusion of the major organ systems, which can lead to organ failure and ultimately death.

Unfortunately, it is estimated that only approximately 10% of patients have a sustained VT which is hemodynamically tolerable for the duration of an activation map [14]. Furthermore, in this small population, it is common that secondary VTs can be initiated which are unstable and, therefore, unable to be mapped. Clinical VT is also classified based on morphology of the 12-lead electrocardiogram (ECG). Monomorphic VT has a single, repeating waveform as seen on a 12-lead ECG recording. In contrast, polymorphic VT presents as

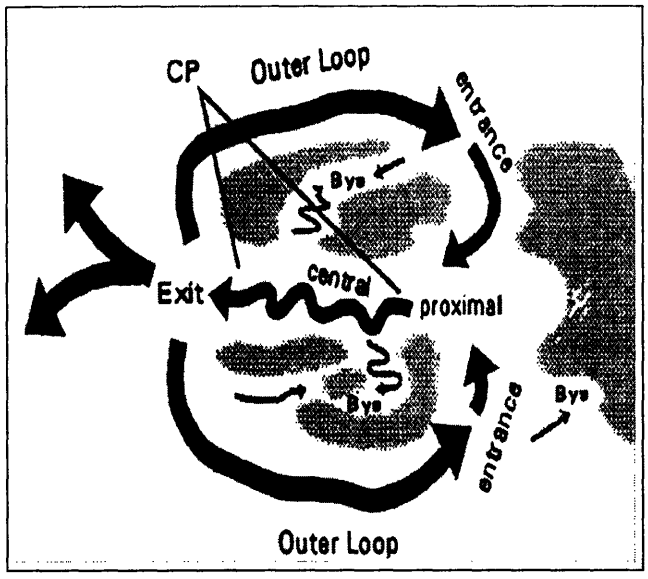

Figure 1-4: Theoretical ventricular tachycardia circuit with multiple entrance sites. In this picture, the gray areas represent regions of conduction block which could result from structural changes such as fibrotic scar tissue or functional block from wavefront collision and refractory. The black arrows represent the movement of the reentrant wavefront. In this reentrant circuit, the main conduction pathway (CP) has two entrance sites and multiple bypass tracts (Bys), which could lead to several morphologies of ventricular tachycardia. (Image reproduced from [16].)

a continuously evolving waveform, suggesting multiple pathways interacting in a complex manner to sustain reentry. It is not surprising that this occurs considering the complex, three-dimensional pathology with multiple entry and exit sites (Figure 1-4) [15]. Options and strategies for treating patients with stable and unstable ventricular tachycardias are discussed next.

1.3 Interventions

There is a wide spectrum of treatments for cardiac arrhythmias including pharmacological therapy, implantable devies, surgical interventions, and catheter-based therapies. A succinct review of current and historically releavent treatment options for arrhythmias including benefits and limitations of these interventions will now be presented.

1.3.1 Pharmacological

Specific drug therapies are targeted at the mechanism causing an arrhythmia. While extensive details are beyond the scope of this thesis, a brief discussion of antiarrhythmic drugs will be included. At this time, there are no long-lasting drugs to treat patients with slow heart rate arrhythmias (bradyarrhythmias). For short-term management of these patients, anticholinergic drugs and β_1-receptor agonists are available. For long term management of tachyarrhythmias, there are four classes of antiarrhythmic drugs commonly used; these drugs target different cellular channels and signaling pathways to alter depolarization and/or repolarization characteristics of myocytes. In addition to antiarrhythmic drug therapy, patients with atrial fibrillation or other cardiovascular disease may be treated with antithrombotic and/or anticoagulant drugs to reduce the change of thrombus formation via platelet function and coagulation cascade.

However, there are many common and potential side effects associated with these drugs. Amiodarone, a commonly prescribed Class III antiarrhythmic drug, can reduce sinus node firing, suppresses automaticity, and interrupts reentrant circuits; however, the side effects can include pulmonary toxicity leading to pneumonitis and pulmonary fibrosis, cardiac toxicity, QT interval prolongation, and gastrointestinal side effects such as anorexia, nausea [17]. Neurological side effects can also include muscle weakness, peripheral neuropathy, ataxia, tremor, and sleep disturbances [17]. From a patient management perspective, these potential side effects must be carefully evaluated versus quality of life for a patient and versus other treatment which are discussed below.

1.3.2 Implantable Devices

The majority of implantable devices in cardiac electrophysiology are pacemakers. These devices are made by a number of manufacturers and have similar features. In general, a pacemaker is a battery-powered, electronic device which is responsible for stimulating the heart to contract at a regular interval. Leads (wires) with electrodes from the device are advanced via the left or right subclavian vein into the right side of the heart, where they are affixed to the wall of the heart. Depending on the patient's condition, leads made be placed in the right atrium or in both the right atrium and right ventricle. Pacemakers may be permanently or temporarily placed to assist patients with acute or transient symptoms fol-

lowing an intervention or secondary to a drug toxicity. Pacemakers are predominantly used to treat patients with bradyarrhythmias (slow-heart rate); however, bi-ventricular pacemakers are increasingly used for cardiac resynchronization therapy for patients with congestive heart failure. In this case, a third-pacemaker lead is implanted within the coronary sinus along the left ventricle of the heart to coordinate the exact contraction timing between the left and right ventricles.

Implantable cardioversion defibrillators (ICDs) and their variants, such as pacemaker-ICDs, are commonly used for patients who have both bradyarrhythmias or conduction blocks as well as a propensity for life-threatening tachyarrhythmias. These devices are able to terminate tachycardias by delivering a high-voltage shock through leads placed within the heart. This shock depolarizes the entire heart simultaneously, and it is used to "reset" the heart from the tachycardia.

Another class of implantable devices relevant to cardiac electrophysiology are left atrial appendage (LAA) occlusion devices; while not clinically approved in the United States at the time of this writing, these are devices which will likely become commonplace for patients with atrial fibrillation. Although strategies differ among the different manufacturers, these devices block blood flow to the left atrial appendage, a structure with relatively low blood flow and a high incidence of thrombo-embolism formation. The goal of these devices are to decrease the risk of stoke and other embolic events in patient populations with atrial fibrillation. Atrial fibrillation disrupts the normal contractile function of the left atrium; therefore, there is an increased prevalence of stasis within that chamber. Stasis of blood leads to thrombosis, which can then embolize to other part of the body resulting in infarction. Many of the methods developed in this thesis could be used to guided positioning of LAA occlusion devices, implantation of other medical devices, or injection of biologically active substances.

1.3.3 Surgical Interventions

While percutaneous catheter ablation using radio frequency (RF) energy has supplanted surgery for most electrophysiology interventions, many key observations and breakthroughs in the treatment of arrhythmias have come from the surgical experience. In terms of surgical treatment of atrial fibrillation, the single-procedure success rate of the Cox maze III procedures (97-99 percent) remains unparalleled by catheter ablation (60-90 percent)

[18, 19, 20, 21]. During a Cox maze procedure, maze-like incisions are made in both atria to prevent multiple macrorentrant circuits necessary to sustain atrial fibrillation. Surgical and catheter based interventions remain the only available curative interventions.

In terms of patient management, catheter-based interventions remain preferred; however, in patients with valvular insufficiency or ventricular aneurysm requiring a surgical procedure, concurrent surgical treatment for arrhythmias is routinely performed. We will now review important observations and developments in treatment which have major implications for catheter-based interventions.

In treatment for Wolff-Parkinson-White (WPW) syndrome, an arrhythmia caused by accessory conduction pathways from the atria to the ventricles, the surgical paradigm for ablative treatment emerged. This paradigm includes three important steps. First, electrode mapping enabled surgeons to elucidate the mechanism(s) for an arrhythmia. Second, an anatomical location of the arrhythmia was localized. This then allowed for the third step: ablation of these pathways to eliminate the arrhythmia. Surgical and experimental procedures and observations demonstrate the feasibility for mapping and ablating arrhythmias using catheterization during a minimally-invasive electrophysiology procedure.

From this paradigm, surgical methods to treat complex arrhythmias including atrial fibrillation and ventricular tachycardias emerged. In terms of atrial fibrillation, high density electrode mapping demonstrated multiple wavelet reentry, during which there is irregular, very rapid, and random activation of the atrium [22]. To eliminate the substrate for these multiple-wavelet circuits, the surgical Maze procedure aimed to compartmentalize the atrium, but it originally allowed for a conduction pathway from the SA node to the AV node. This procedure, along with the later insights of a focal triggers of atrial fibrillation located in the pulmonary veins has resulted in the catheter-based procedure which are described below.

For VT treatment, catheter-ablation methods evolved directly from the surgical modification of arrhythmogenic substrate in post-MI patients. Since the reentrant circuit is predominantly located within the border zone between normal and scarred myocardium, the initial surgical experience with simple aneurysmectomy was disappointing [23, 24]. Further experimentation over time resulted in two effective strategies: subendocardial resection and encircling endocardial ventriculotomy (Figure 1-5). The resection involves surgical removal of the subendocardial layer contain the arrhythmogenic substrate in the border zone

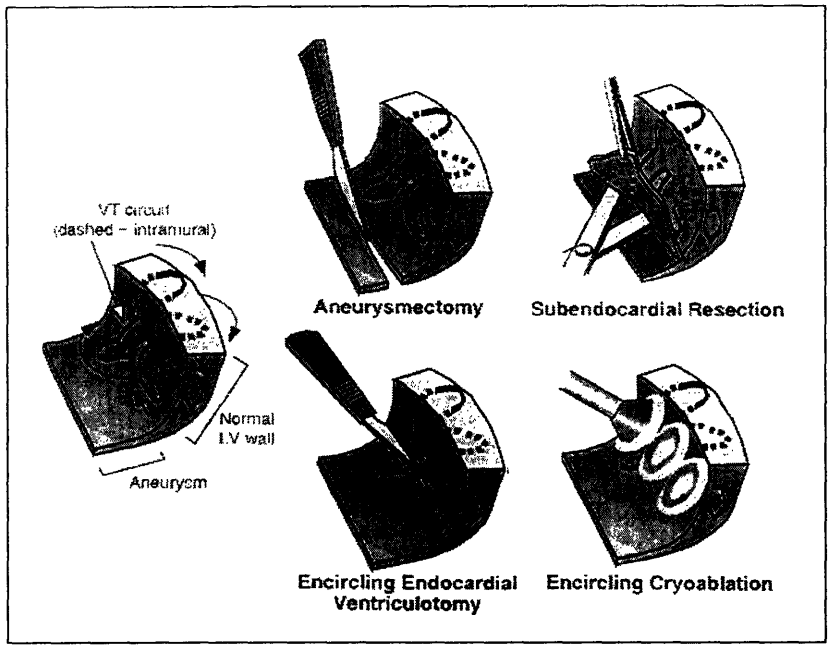

Figure 1-5: Surgical substrate modification for treatment of VT. At the border between infarcted or aneurysmal myocardium, a VT circuit is represented predominantly on the endocardial surface of the heart with some transmural portions. Surgical procedures including subendocardial resection and ventriculotomy are thought to remove or transect and disable critical endocardial portions of the reentrant circuit, respectively. Using this knowledge, electroanatomical mapping allows the border zones to be identified based on electrogram characteristics (described below). Ablations are then placed at entrance and exit sites in an attempt to disrupt these critical portions of the reentrant circuit. Figure reproduced and adapted with permission from [25].

[25, 26, 27]. Endocardial ventricullotomy consists of the placement of circumferential surgical lesions through the border zone, which presumably disrupts the reentrant circuits which sustain VT [28, 29]. In place of or as an adjunct to subendocardial resection, cryoablation has been used as an intervention during surgery; likewise, the incorporation of cryoablation with endocardial ventriculomoty was similarly effective [30, 31]. This ablative modality is effective in destroying myocardial cells without disrupting the fibrous stroma in the regions surrounding the scar.

Several important lessons learned from the surgical experience treating ventricular tachycardia remain relevant for modern catheter-based approaches. First, intraoperative mapping was initially performed as an additional guide for surgical resection. A multi-electrode plaque would be placed on the endocardial surface of the ventricle, and the origin of the VT would be removed or transected using a scalpel blade. During evolution of this surgical

procedure, however, it was determined that equivalent results were obtained by visualizing the scar and either simply resecting it or placing cryoablation or laser ablation lesions along its border. These "empiric" lesions are thought to eliminate critical portions of the reentrant pathway, and therefore render the VT non-inducible.

1.3.4 Cardiac Catheterization

While highly efficacious in the long-term, these surgical procedures are associated with significant peri- and post-operative morbidity and mortality (3-14%). Because of the high success rate and low morbidity, catheter-based electrophysiology procedures are now the preferred intervention for the treatment of most arrhythmias. During this procedure, one or more catheters are advanced percutaneously through the vasculature into contact with cardiac tissue. Femoral veins and arteries are the most common entry sites for catheterization of the heart; additional access can be gained at the subclavian and jugular veins, but these sites are less commonly used. A hemostatic sheath is placed at the access site, which allows for easy exchange of catheters and guidewires with minimal blood loss to the patient. Catheters are then advanced up the femoral vein into the inferior vena cava and the right atrium of the heart. For access to the left heart, a catheter can be advanced retrograde up the femoral artery into the descending then ascending (arch) aorta; the catheter is then advanced across the aortic valve plane into the left ventricle of the heart (Figure 1-6).

Additional access, if needed, to the left heart is commonly gained via a transseptal puncture across the septum separating the left atrium and the right atrium. Transseptal access is the major access avenue during catheter-based atrial fibrillation ablation procures, and it is also commonly used to reach difficult positions in the left ventricle during other procedures.

Catheter ablation has been highly successful in the treatment of accessory pathways, AV nodal reentrant tachycardia (AVNRT), and AV junction ablation. However until the introduction of electroanatomical mapping systems, treatment of complex arrhythmias such as atrial fibrillation and ventricular tachycardia remained extremely difficult. Without a catheter mapping system, electrophysiologists were challenged with integrating in their minds information including 1) fluoroscopic catheter position information 2) bioelectrical characteristic recorded at various catheter locations 3) ablation lesion placement and 4) post-ablation electrical information.

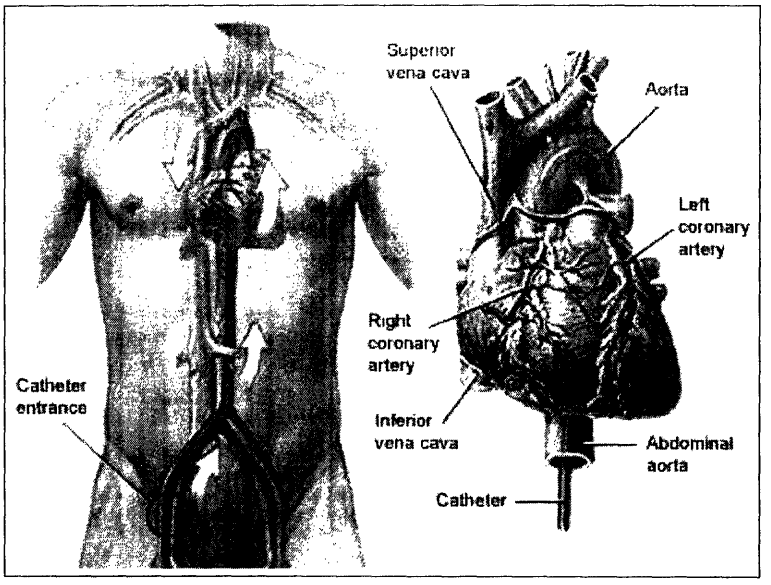

Figure 1-6: Cardiac catheterization. During a catheterization procedure, percutaneous access is gained at the femoral arteries and veins near a patient's groin. The catheter is then advanced up either the aorta or the inferior vena cava into the left ventricle or right atrium, respectively. While catheters are used for a wide variety of diagnostic and interventional procedures, electrophysiology studies are focused on electrogram information recorded from the distal electrodes on the catheter.

1.3.5 Catheter-Based Electroanatomical Mapping

To overcome these difficulties, catheter localization and arrhythmia mapping systems have been developed, and these systems have resulted in effective, catheter-based treatments of complex arrhythmias. These electroanatomical mapping (EAM) systems simultaneously record both the position and bioelectrical information for one or more electrode on one or multiple catheters (Figure 1-7). These biolectrical recordings are known as *electrograms*. The electrogram information is then annotated relative to the surface ECG signal. Common annotations include maximum unipolar voltage at the distal electrode on the mapping catheter, maximum bipolar voltage between the two most distal electrodes on the mapping catheter, and local activation time (LAT) which indicates the starting time of the electrogram relative to the ECG reference (Figure 1-7). While these three annotations have been most commonly used, there has been some additional work with electroanatomical mapping using annotations including dominant electrogram frequency, electrogram fractionation indexing, electrogram duration, and impedance mapping [32, 33].

Currently, there are three types of localization commonly used: 1) ultra low-field mag-

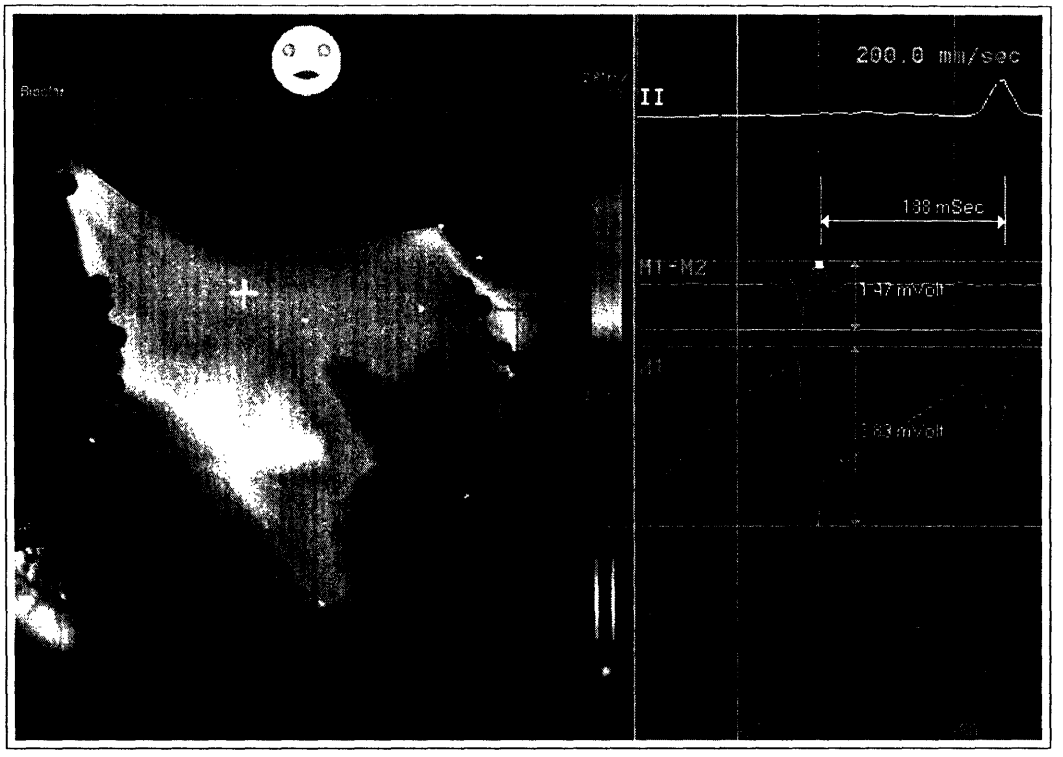

Figure 1-7: Electrogram Annotation. In the left frame, an anterior-posterior (AP) view of a left atrial electroanatomical map produced with the Carto XP system. The white cross-hair cursor indicates the selected point on the map. The corresponding electrogram annotation is shown on the right-hand side of the image. At the top of the electrogram annotation window, Lead II of the 12-lead ECG is displayed. The red point and dotted line on the right indicate the reference annotation, which is made on the maximum value of Lead II a consistent point of the QRS complex during ventricular contraction. Below, Lead II, the bipolar (M1-M2) and unipolar (M1) electrogram recording made from the distal tip of the catheter are shown. The maximum bipolar voltage (M1-M2) for this point is indicated by the vertical calipers (1.47 mV). Likewise, the maximum unipolar voltage (M1) is also annotated (3.83 mV). Finally, the Local Activation Time (LAT) is the relative time measured from the reference annotation to the annotation made on the electrogram information (yellow dot; left hand dotted line). For the point selected, the LAT is -188 ms, which indicates this spot is excited 188 ms before ventricular contraction.

netic 2) sonomicrometry and 3) bioimpedance. The predominant magnetic electroanatomical (MEAM) platform is the CARTO system (Biosense-Webster, Diamond Bar, California, USA), which creates three-dimensional (3D) maps of electrophysiology characteristics and chamber anatomic definition by continuously tracking and annotating catheter locations (Figure 1-8) [34]. The CARTO EAM system creates low-intensity magnetic fields from a device placed beneath the operating table to localize the catheter in space with 6 degrees

of freedom (position in x, y, and z; rotation of roll, pitch, and yaw) [34]. With this system, a single mapping catheter is manipulated in various spaces in and around the heart and great vessels proximal to the heart; the position is tracked relative to a reference patch or catheter usually temporarily fixed to the upper back of a patient. The accuracy of this system is estimated at 0.8 mm in position and 5 degrees in rotation.

1.4 Diagnostic Modalities

In many cases, overt symptoms of cardiac arrhythmias may be absent or subtle, and many patients may not recognize a problem for which they should seek medical attention. Patients may present with a range of symptoms including syncope, dyspnea, palpations, angina, or chest discomfort, overt heart failure, or myocardial infarction [35]. An overview of important diagnostic modalities is presented in Table 1.2. Details of imaging and other diagnostic modalities are presented below.

Table 1.2: Imaging modality comparison.

Modality	Cardiac Device Compatability	Spatial Dimension	Approx. Spatial Resolution (mm^2/mm^3)	Radiation Dose	Soft tissue contrast
Fluoroscopy	Yes	2D	0.3 x 0.3	Med-High	−−
MRI	No	3D	0.5 x 0.5 x 1.2	0	+++
CT	Yes	3D	0.3 x 0.3 x 0.5	High	+
Ultrasound	Yes	2D/3D	0.35 x 0.35	0	+

1.4.1 Electrocardiogram

The 12-lead electrocardiogram (ECG) is the primary way to initally diagnosis arrhythmias. This non-invasive test uses a combination of limb-leads and precordial chest leads to record the change of the principle heart vector over time. While the ECG is a powerful tool for identifying abnormal cardiac rhythms, it is significantly limited in its ability to localize the focus or reentrant circuit which is initiating and/or sustain an arrhythmia.

1.4.2 Fluoroscopy

Fluoroscopy is an x-ray imaging modality used extensively during interventional catheterization procedures. While this imaging modality is fast, providing real-time ciné images of

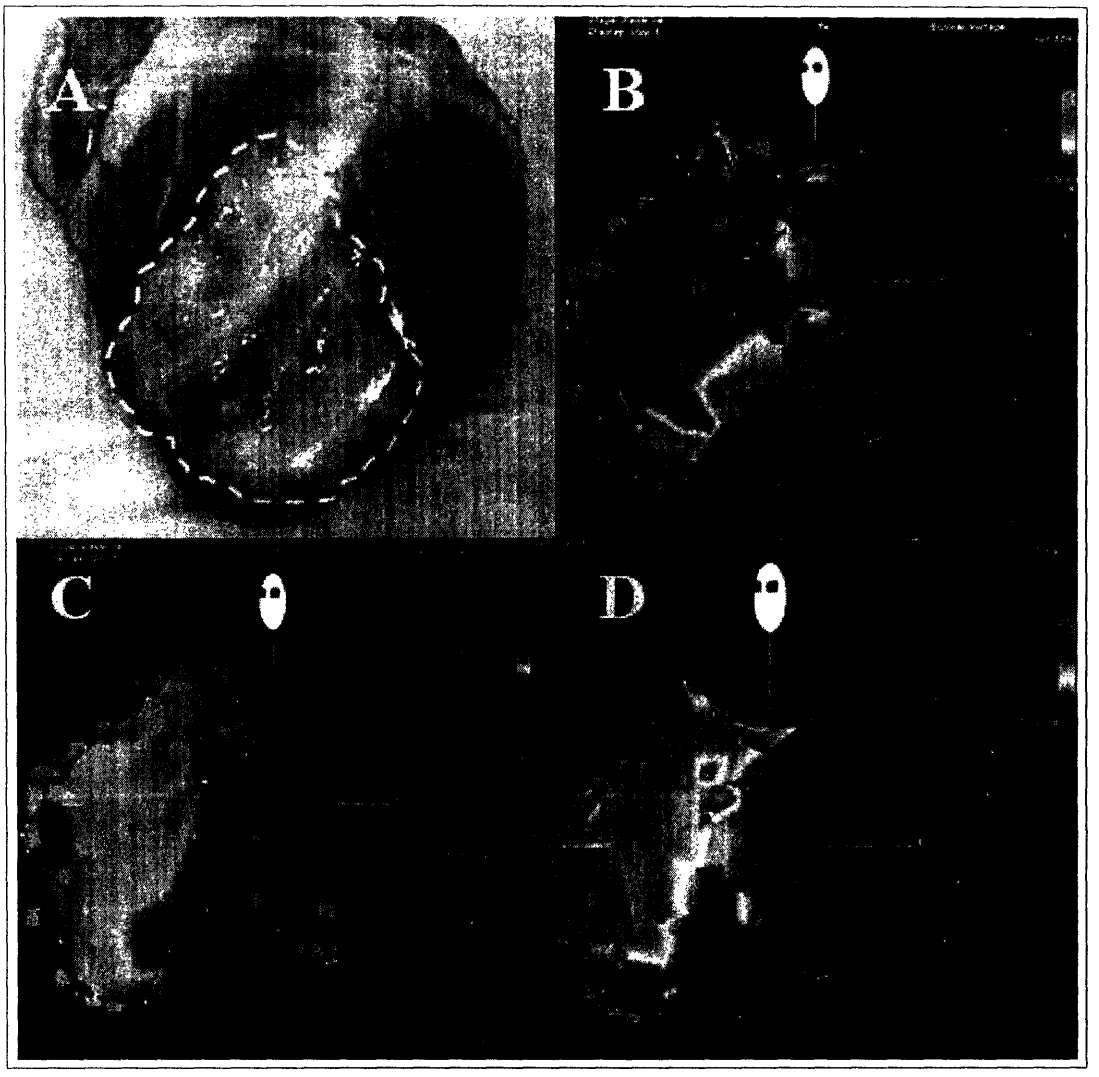

Figure 1-8: Electroanatomical mapping of porcine model of chronic myocardial infarction. In this model, an infarction is created by occluding the left anterior descending coronary artery with agarose microspheres. Eight weeks following the infarction, electroanatomical mapping of the left ventricle is performed using the CARTO mapping system. Upon gross pathological examination (A), the transmural scar is visible from the epicardial surface of the anterior wall. *In vivo* electroanatomical mapping identified this anterior wall infarct by bipolar voltage amplitude criteria (B), unipolar voltage amplitude criteria (C), or bipolar EGM duration criteria (D). The projections are LAO in B-D; note the characteristic leftward rotation of the porcine heart. The color ranges in the bipolar voltage, unipolar voltage and EGM duration maps are 0.5 1.5 mV, 2 7 mV, and 50 80 msec; purple and red represent normal and severely diseased tissue in the bipolar and unipolar voltage maps, while the opposite is true for the ECG duration map.

the thoracic cavity, it has a limited ability to image soft tissue.

Rotational angiography is an emerging technology which utilizes a fluoroscopy system

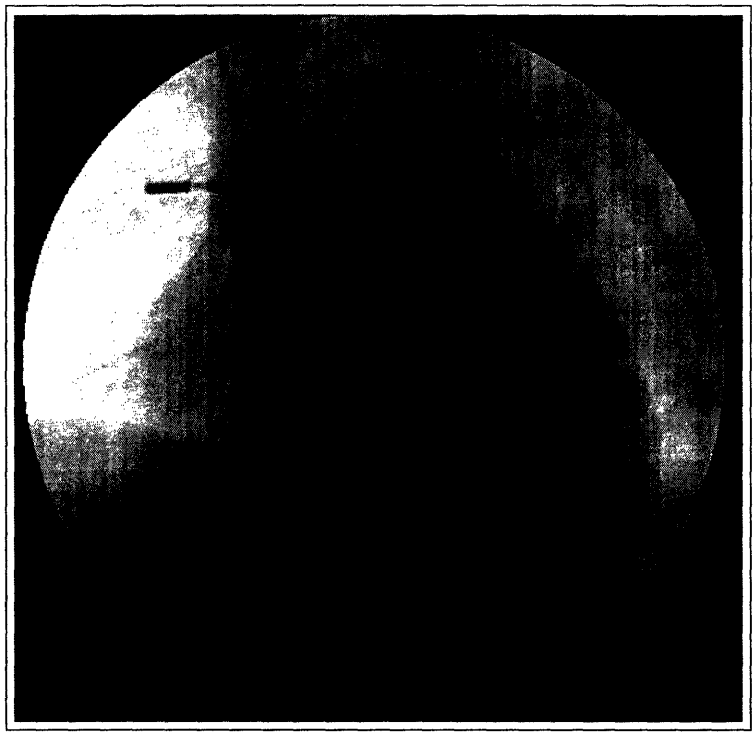

Figure 1-9: Anterior-Posterior (AP) fluoroscopic image showing a patient undergoing electrophysiology study. In this image, a patient has a decapole catheter within the coronary sinus, a 10-pole lasso catheter within the right superior pulmonary vein, and an 8-mm tip electroanatomical mapping catheter within the right superior pulmonary vein of the left atrium. While fluroscopic imaging provides real-time imaging of catheter orientation, the standard view is a 2D projection of a 3D space, and there is minimally soft-tissue contrast available discern cardiovascular structures.

to capture a series of images from multiple rotational angles about an isocenter. A typical rotational acquisition requires only 4 to 8 seconds of normal fluoroscopic exposure, a small amount considering the several hours of fluoroscopy patients may receive during an extremely complex ablation procedure. A back-projection algorithm can then be used with cardiac gating information to reconstruct various chambers and vessels of the heart. While these systems are currently commercially available, further work is being performed to optimize the acquisition and reconstruction of the data. Rotational angiography has the potential to provide intra-procedural 3D reconstructions of the cardiac anatomy.

1.4.3 Magnetic Resonance Imaging

Cardiovascular magnetic resonance imaging (MRI) is effective for imaging structures and function of the heart without the use of ionizing radiation (Figure 1-10). The standard clinical cardiac MRI system has a main magnetic field strength of 1.5 T with 3.0 T systems becoming increasingly common. The advantages of cardiac MR include its three-dimensional imaging capabilities and its soft tissue differentiation. However, implantable cardiac devices such as pacemakers and ICDs remain contraindications for MR examination.

Current and future efforts include parallel channel image acquisition to increase imaging speed through interleaving and interventional magnetic resonance imaging (iMRI) during which catheters will be tracked under real-time MR guidance using a combination of pre-intervention and intra-interventional imaging.

1.4.4 Computed Tomography

Computed Tomography (CT) imaging now provides high spatial-resolution (0.3 x 0.3 x 0.5 mm voxel size), ECG-gated imaging (Figure 1-11). Image reconstruction is retrospectively gated to the electrocardiogram. For an atrial reconstruction, the exam is gated to 65 percent of the R-R interval (time between heart beats), which should represent atrial diastole before atrial contraction. Likewise, for ventricular imaging, the exams are reconstructed at ventricular diastole before ventricular contraction (90 percent R-R interval).

1.4.5 Ultrasound

Ultrasound or echocardiography is an essential diagnostic and long-term monitoring modality for numerous cardiac conditions. Briefly, high-frequency sound waves (5-9 MHz) are

Figure 1-10: Contrast-enhanced magnetic resonance angiography (MRA) of the heart. The two left images are oblique reformats of the left atrium and pulmonary veins from a 3D MRA imaging dataset. In the left frame, the relationship of the posterior wall of the left atrium to the descending aorta is seen as well as that of the pulmonary veins to the branching pulmonary artery. In the middle frame, a clear view demonstrates the proximity of the left main branch of the pulmonary artery next to the left upper pulmonary vein. The right frame is a 3D surface reconstruction showing the intricate relationship of the left atrium, pulmonary veins, and pulmonary arteries from a right posterior oblique view. These images were acquired on a 1.5 T GE Signa CVi MRI with a 25.0 x 25.0 cm FOV. The reconstructions were performed on an GE Advantage Workstation.

emitted from a probe. These waves travel through and are reflected back by various tissues and structures within the body. These reflections are then used to create 2D or 3D images of the heart.

There are three main types of ultrasound commonly used in conjunction with cardiac electrophysiology. First, trans-thoracic echocardiography (TTE) is commonly used pre-operatively to assess cardiac parameters such as ejection fraction, valve insufficiencies, and wall motion. During a TTE exam, the ultrasound transducer is placed on the patient's skin to create one of many common views (apical four chamber, apical two chamber, parasternal long axis). Second, transesophageal echocardiography (TEE) uses a miniature transducer on an endoscope type probe to image from the esophagus located posterior to the left atrium.

Intracardiac Echocardiography (ICE) is commonly imaging modality used during catheter-based interventions. A single linear ultrasound array is located on the tip or a deflectable 8- or 10-French catheter (2.3 or 3.2 mm diameter). The catheter is typically placed within the right atrium or coronary sinus to image various aspects of the left atrium during pulmonary

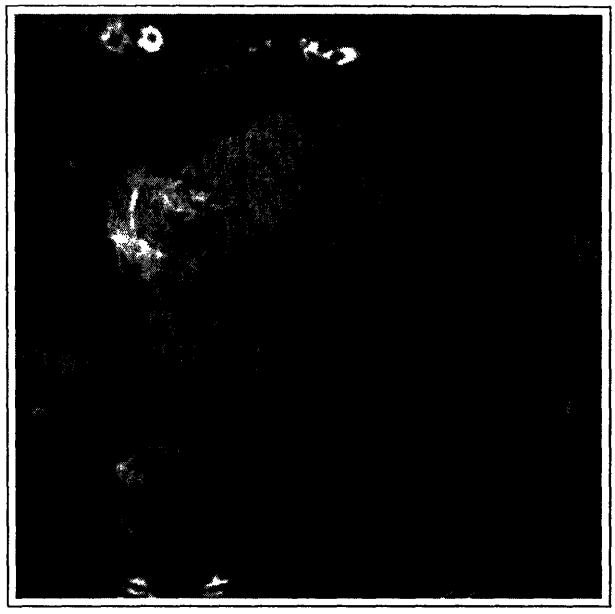

Figure 1-11: Axial slice from CT imaging of the heart showing a four chamber view of the heart. This acquisition was made using iodinated contrast give as a bolus from a peripheral intravenous line. CT can provide high spatial resolution but does not provide extensive soft-tissue contrast. The heterogeneous distribution of contrast agent can cause imaging artifacts; as demonstrated in this image, the high contrast concentration in the right atrium causes scattering artifacts. Besides contrast, pacemaker and ICD leads can also cause significant artifacts; however, CT imaging does not interfere with the normal operation of these devices. The reconstruction was retrospectively cardiac gated. This image was acquired on a Siemens Sensation 16-slice CT scanner.

vein isolation to eliminate atrial fibrillation.

1.5 Surgical Planning and Imaged-Guided Surgery

Surgical planning and image-guided surgery enhance a physician's understanding of reality by augmenting the normal senses with additional information provided by the various diagnostic modalities described above. Surgical planning uses this information to understand the extent of a disease process and optimize the intervention to the specific needs of a patient. Image-guided surgery uses the pre-operative data in combination with intra-operative information to assist a physician during an intervention.

In terms of electrophysiology procedures, surgical planning and image-guidance could be useful in many ways. The preferred treatment for atrial fibrillation is pulmonary vein isolation, where RF ablations are placed circumferentially around the ostium of the pul-

monary vein. As described above, pulmonary vein stenosis resulting from ablation within a pulmonary vein is a serious complication of these procedures. Therefore, surgical planning could be useful for identifying per-patient anatomical variations in pulmonary vein type. Additionally, this information could be used to plan an optimal ablation lesion set which minimizes the risk of complications yet requires the fewest RF lesion applications. Within a procedure, image-guidance could augment the relatively sparse EAM mapping with high resolution, patient-specific anatomical information. For treatment of ventricular tachycardia, this paradigm could also provide important physiological information regarding the location and extent of myocardial scar tissue in which reentrant circuits predominantly reside.

1.6 Thesis Goals

Electroanatomical mapping is widely used to guided catheter-based ablation of complex cardiac arrhythmias. While electroanatomical mapping allows a physician to create relatively sparse but relevant representations of the endocardial and epicardial surfaces of the heart, pre-operative imaging could provide both anatomic and physiologic information not available to physicians. This information could be used pre-operative to understand important anatomical variations and pathological disease state. During an electrophysiology intervention, this information could then be used as a patient-specific guide for ablation to eliminate an arrhythmia.

In this thesis, we examine these problems and propose solutions which not only allow for the incorporation of pre-operative cardiac imaging with intra-operative electroanatomical mapping data, but which also allow a physician to understand the robustness of the registration and to compensate for differences between pre-procedure and intra-procedural information. First, in Chapter 2, we describe our surgical planning platform, the Myo system, which incorporates pre-operative imaging data with real-time catheter mapping data to visualize the position of a catheter within patient-specific imaging data. Next, in Chapter 3, we present a variant of the iterative closest point algorithm as well as various clinical strategies to register or align the pre-operative imaging data with sparse intra-operative electroanatomical mapping information. To compensate for residual differences following a registration, methods are presented and evaluated in Chapter 4 to deform or warp the

pre-operative imaging data to more closely match the intra-operative information. Finally, in Chapter 5 we present a summary of our research and propose avenues for future development.

Chapter 2

Myo Surgical Planning System

In this chapter we describe the Myo software system which integrates pre-operative, patient-specific MR and/or CT imaging information with real-time electroanatomical mapping information. The system has been used for image-guided therapy in a large number of complex cardiac electrophysiology ablations, and it continues to evolve. We present the resulting application programmer interface (API) used to develop the modular Myo application as well as related, inter-communicating programs for ablation information, signal processing, and image processing. Although registration was the primary intent of the Myo software, the system has evolved into a platform which allows for integration of information from many sources during cardiac electrophysiology procedures.

2.1 Introduction

Image-guided surgery and surgical planning have become important tools to assist physicians with diagnostic, pre-procedural planning, and perioperative guidance. These systems are expected to provide advanced visualization, segmentation, and registration algorithms to process information within one environment, and they must be extremely robust through then entire duration of an intervention, which can last from 2-12 hours. Beyond these rigorous specifications, physicians and engineers must work together to streamline surgical planning into the clinical workflow of an intervention; while these systems provide valuable information to the physicians, they must accomplish these goals with minimal amount of distractions and data gathering requiring the attention of the interventionalists. From a research standpoint, a surgical planning system should be a flexible framework which allows

for rapid integration of new algorithms and information to further increase the utility of the system before, during, and after interventions.

Surgical planning has been and continues to be an active area of research between engineering and medicine. While the Myo surgical planning system will be presented in depth here, it is worth noting that there are several surgical planning systems available from academic research centers and commercial entities. The origins of the surgical planning field are found with the ANALYZE system developed by the Biomedical Imaging Resource at the Myo Clinic since the early 1970s [36, 37, 38]. It would be difficult to discuss surgical planning without acknowledging the open-source 3D Slicer platform and the advance research and development activities of the Surgical Planning Laboratory (SPL) at Brigham and Women's Hospital in Boston, Massachusetts. The SPL and the 3D Slicer software are actively developed and lead the fields in numerous area beyond image-guided neurosurgery using the open-bore magnetic resonance therapy (MRT) system [39, 40]. Finally, the National Alliance for Medical Image Computing (NA-MIC) is a research initiative to incorporate the best-of-practice from the countless on-going research projects in medical imaging, image processing, and surgical planning [41].

Surgical planning and image-guided therapies have been an active area of research; however, little work has been focused on surgical planning in the heart. To address this need we present the Myo image-guided therapy system. To fully utilize patient-specific imaging data before, during, and after a catheter-based cardiac intervention, the Myo system is capable of integrating both pre-operative imaging data with real-time intra-procedural data from multiple sources. In the following discussion, the constraints, design, and features of the Myo software system will be presented.

2.2 Myo Design Goals and Constraints

In designing the Myo surgical planning software, it is useful to review the operating constraints for the system. These constraints include practical restrictions in terms of patient management, the electrophysiology lab and procedures, and input data to the system.

An electrophysiology study is a complex procedure to identify and eliminate arrhythmogenic substrates from a patient's heart. These procedures involve a wide range of technologies including a fluoroscopic imaging system, an EP recording system, stimulator, an elec-

Source	Data Aquisition	I/O Source
MR Imaging	Pre-Operative	Binary File
CT Imaging	Pre-Operative	Binary File
Rotational Angiography	Pre-Operative	Binary File
Electroanatomical Mapping	Real-time	TCP/IP
RF Ablation	Real-time	Serial
Electrogram Information	Real-time	ADC Board
Robotic Guide Catheter System	Real-time	TCP/IP

Table 2.1: Myo information sources

troanatomical mapping system, an RF ablation generator, ultrasound imaging equipment, and possibly some sort of remote catheter manipulation system (Figure 2-1). Currently, these systems are largely independent, and it is the responsibility of the electrophysiologist to integrate information from these many sources.

From a practical perspective, the surgical planning software for use in the electrophysiology laboratory must be robust, fast, accurate, and easy to use. In addition, the system can be used to make powerful combinations of information already observed by the interventionalist. For example, pre-operative imaging data with electroanatomical mapping information and RF ablation information, pre-operative lesion placement can be planned and intra-operative assessment of RF lesions could be more accurate than current methods. Therefore, the system should integrate information in useful ways to facilitate a better understanding and treatment of an arrhythmia.

From a research and development standpoint, there are many desirable qualities for the Myo software. Stemming from the close collaboration of doctors and engineers for this project, there is rapid iteration, development, and evaluation of ideas constantly occurring. To facilitate this research, a software architecture which is highly modular and easy to extend is desired. Furthermore, a modular design allows development by several researchers to occur simultaneously as long as interface specifications are well defined.

2.2.1 Imaging, Navigation, and Electrophysiology Information

The Myo system is able to import and export real-time and pre-operative information from a wide variety of sources.

Catheter Position Information

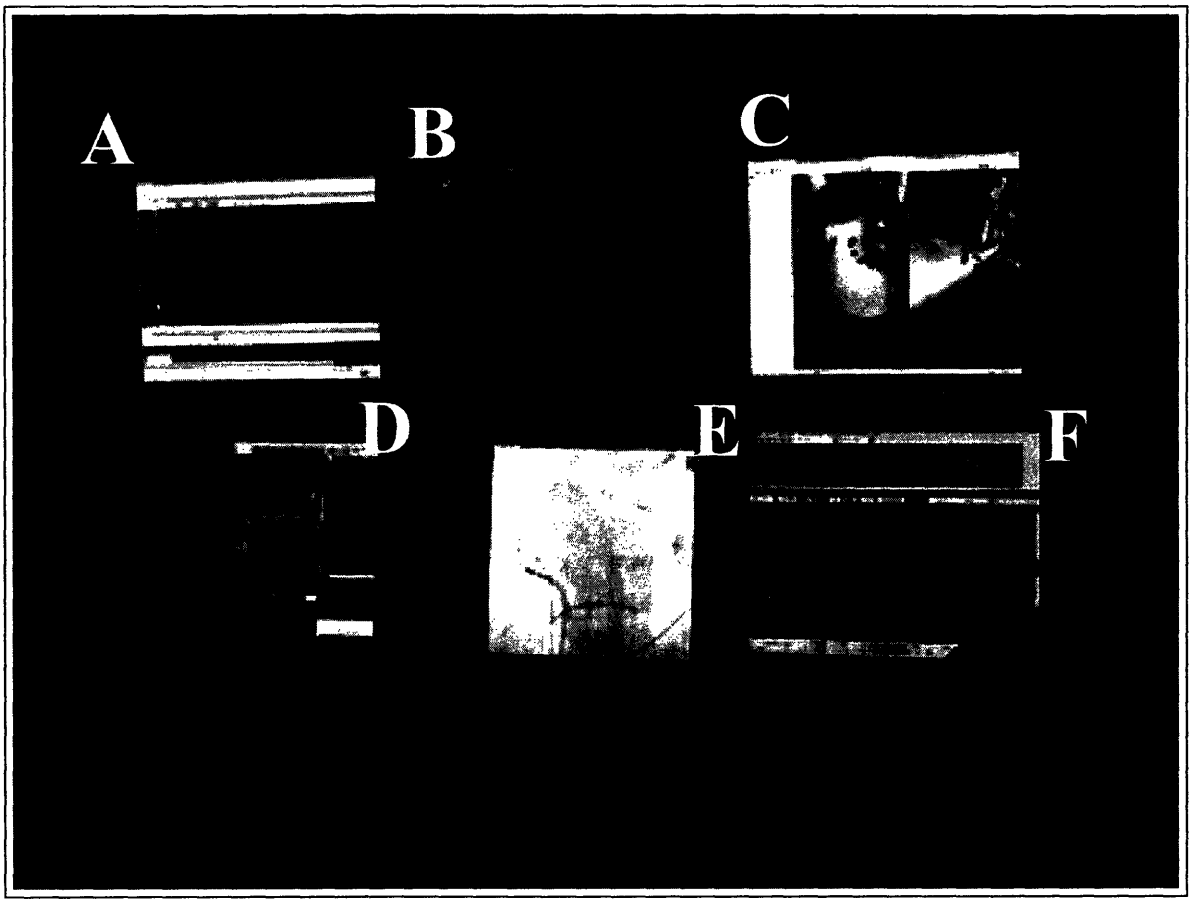

Figure 2-1: Information display during EP study. This photograph shows the numerous sources of information an electrophysiologist must integrate during a catheter-based electrophysiology study. In this photograph, the physician uses an EP recording (A, F) to display and review electrogram information from various catheters, an electroanatomical mapping system (D) to co-localize catheter positions with electrogram information, real-time and review screens (B, E) for fluoroscopy display, and the Myo software system (C) to provide patient-specific pre-operative catheter navigation information.

As discussed in the introduction to this thesis, there are several electroanatomical mapping systems currently used during electrophysiology interventions. The goals of these systems is to provide non-fluoroscopic guidance for catheter manipulation. While providing the physician with real-time feedback of the catheter location each system handles cardiac and respiratory motion directly or indirectly. Real-time data streams from both the Biosense-Webster CARTO system and the Medtronic LocaLisa system have been integrated into the Myo framework. We will now review the information provided by these systems.

In terms of the CARTO system, a continuous stream of three-space positions (x,y,z) and orientations (pitch, yaw, roll) for the single mapping catheter is provided. Additional information is provided to determine the proper gating of the catheter location to an isochronal point within the cardiac cycle. These measurements are relative to a reference patch adhered to the back of a patient. The use of an intravenous reference catheter within the coronary sinus would eliminate respiratory motion effects; however, both the additional expense and relative instability of this configuration have made it less common in clinical practice.

Medical Imaging Data

From a data accuracy point of view, it would be highly desirable for pre-operative imaging (CT or MR) to be completed immediately proceeding the catheter-based electrophysiology procedure in order to minimize the effects of hydration/fluid levels, rate, and rhythm changes between imaging and intervention. However, the reality of scheduling make this nearly impossible, and imaging studies can be performed anywhere from days to months before the electrophysiology. This results in the first constraint for the surgical planning software: it must eliminate the need for external marks on a patient for use a fiducials, as it is likely that semi-permanent marks would be erased before an intervention. From a practical perspective, external fiducial markers would be difficult to use, their utility for registration will be discussed in Chapter 3.

2.3 Myo System Architecture

To integrate the real-time and pre-operative information described above, we will now review the design of the Myo system.

2.3.1 Design Philosophy

The Myo system was designed to meet the needs of a specific area of medicine: cardiac electrophysiology. While the Myo system may not include many of the generalized features of the aforementioned surgical planning systems, a flexible but focused framework was designed and implemented to meet the specific needs of this medical specialty. By focusing the application domain, the system allows for easier and quicker yet powerful user interactions during a procedure. This system and the methods and strategies used for image integration in cardiac electrophysiology are designed to be streamlined in the current clinical workflow of an electrophysiology procedure. While many surgical planning systems have extensive features and capabilities, they also suffer from general and sometimes confusing user interfaces which require expert knowledge to use the system.

Besides ease of use, the Myo system was also designed to maximize efficiency for its developers. While the system started as a light-weight framework which wrapped the various libraries and toolkits that it integrated, the Myo system evolved to a heavy-weight framework which allowed developers to rapidly reuse high-level and complex objects for numerous applications; by abstracting common components into the MyoAPI, it reduced the overhead required to develop new modules within the application.

2.3.2 Development Platforms

The Myo system was developed in C++ using the Visualization Toolkit (VTk) for OpenGL graphic capabilities, the Insight Toolkit (ITk) for registration and segmentation algorithms, and the Qt application framework for the graphical user interface [42, 43, 44]. The resulting Myo system is cross-platform compatible.

The VTk provides advanced 2D and 3D rendering capabilities which are layered on top of the OpenGL graphics libraries. By using OpenGL, the VTk takes advantage of hardware acceleration now commonly available on mid- to high-end PCs and workstations. The VTk uses a pipeline design to visualization data. A visualization pipeline consists of sources which provide the data, filters which affect the data, and sinks which either store the data or allow the data to be interactively visualized. This pipeline design allows for computational efficiency through a lazy-execution model of the various pipeline components; when an object is modified in the pipeline, only the dependent objects following the modified

object are required to update.

The ITk provides an extensive set of segmentation, registration, and finite-element analysis (FEM) algorithms. Although it does not provide visualization algorithms itself, the ITk can be easily integrated with the VTk to display the information processing results. The ITk leverages the generic program concepts available in C++ to provide a framework that processes any dimensional data. The ITk makes use of processing pipelines which operate in an analogous fashion to the visualization pipelines of the VTk. The pipeline design of these toolkits has directly impacted the design of the Myo system, and we will return to this topic in the discussion below.

While the VTk and ITk provide a powerful set of tools to manipulate and visualize image data, these systems do not provide user interface. The Qt application framework was used to provide the graphical user interface to the Myo system.

2.3.3 Myo Module Design

The Myo system is comprised of many specific modules derived from the generic framework which use a common communication system (see below) to pass information objects within and between various modules (Figure 2-2). For each module, a single MyoProcessor is instantiated, and this class is responsible for controlling the information flow within each module as well as with other modules. The MyoProcessor is the parent to various MyoControllers, which are responsible for processing data, user interactions, and messages received from other modules. In terms of the classic model-view-controller design pattern, the MyoProcessor acts as the interface between the GUI components (view) and the data or model. In terms of data, a flexible tree data type has been implemented which can send and receive message from within the module as well as from other modules, if the parent of the data node delegates them to its children.

This modular, object-oriented design has many advantages including conceptual clarity, reusability, reliability, extensibility, robustness in the face of exceptions, and maintainability. In general, object-oriented design is conceptually focused on reducing complex problems into simpler objects; from a development standpoint, these complex objects can be derived from simpler objects through inheritance. Object-oriented design facilitates collaborative development through specification definition between various components of a system.

Within and between modules, the Myo architecture leverages many common design

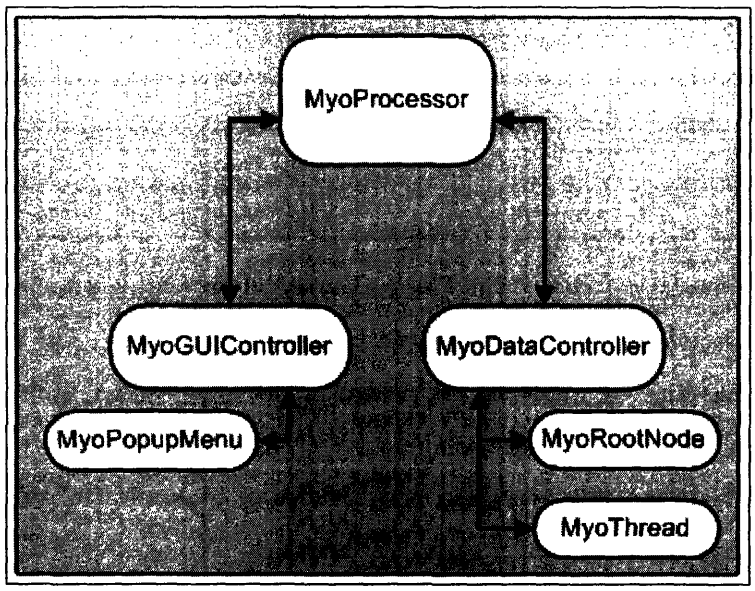

Figure 2-2: Generic Myo module diagram. A Myo module consists of a top-level MyoController Object which is responsible for handling inter- and intra-module communication. In addition, the module may include processors which are responsible for handling GUI actions, managing and processing module specific data, and

patterns to create the proper abstractions [45]. In the Myo architecture, all classes are derived from a basic MyoObjet class, which provides a unique hashcode, a method for comparing object equality, and a simple output method which converts the object's identity into a string representation.

2.3.4 Myo Communication

Layers of software abstraction are created via data hiding and encapsulation. A mechanism is needed which will allow various objects to send and receive messages. In the Myo system, there are three major types of messages which are handled via the Myo communication system: (1) inter-module communication (2) intra-module communication and (3) thread communication. To communication between modules, a MyoEvent is used. A concrete subclass of MyoEvent can be sent from any MyoObject-derived class. The event is then propagated up the object hierarchy to the MyoProcessor. The MyoProcessor then passes the message to the MyoApplication communication system, which will deliver the event to all other modules which have registered as listeners for this type of event. From communication between objects within a single module, a MyoSignal should be used. Fi-

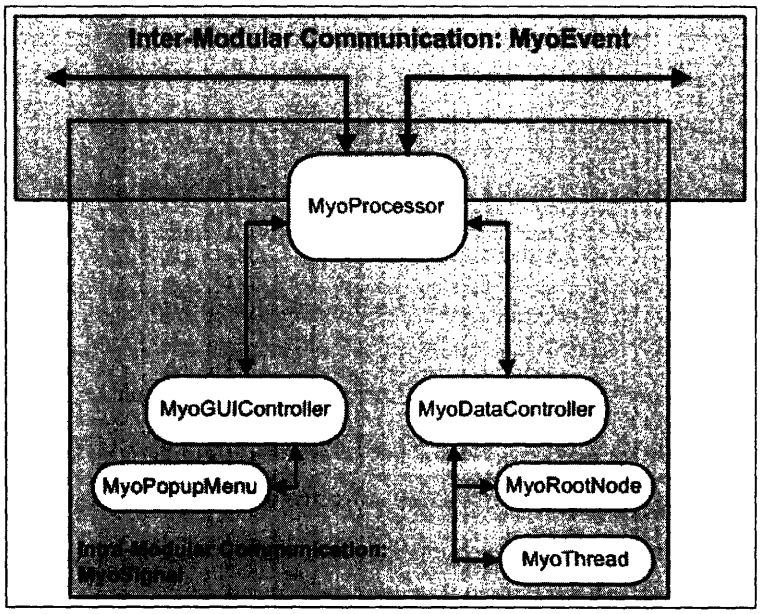

Figure 2-3: Myo communication. There are two main mechanisms in place for communication within the Myo framework. Events are messages which can be sent by any object; these messages are intended for communication between different modules. For localized message, such as communication between the GUI components and data representation, there are signals, which will not be propagated to other modules within the application. The signals are directional; they can be sent to the children of an object or they can be sent to the parent, who will redistribute the signal to its children or parent. In order for an event to be received and processed within a module, the module must be register as a listener for that event, and an appropriate event handler must catch the event.

nally, MyoThreadSignals are used to pass information from worker threads to the main GUI thread.

2.3.5 Myo Visualization Pipeline

The Myo architecture leverages the VTk and ITk packages for advanced 2D and 3D visualization, segmentation, and registration capabilities. These packages use a pipeline design which consists of objects that represent the data, objects which operate on the data, and a direction of data flow [42]. This pipeline model is built on the idea of having source data which is subsequently processed and multiple view of the data are available (Figure 2-4). The pipeline uses a lazy execution model which only executes processes down stream to a modification within the pipeline. Therefore, parallel branches within the pipeline do not need to be refresh if a modification is made after the branch point within the topology of

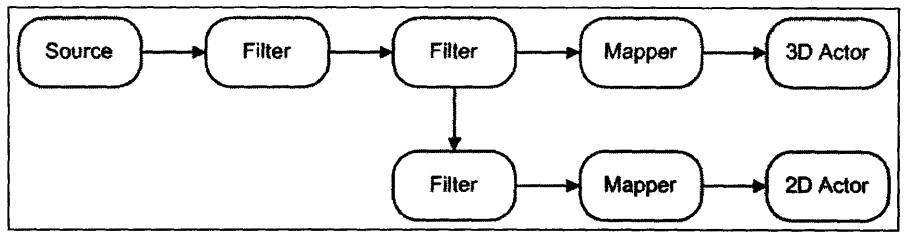

Figure 2-4: Myo visualization pipeline.

the pipeline. Controlling synchronization of arethe pipeline elements occurs through explicit and implicit execution control. For the purpose of the Myo system, the explicit execution is used to force timely updates of real-time information provided by the electroanatomical mapping system. Other information is updated as needed through implicit control.

In order to leverage the pipeline model within the Myo architecture, a wrapper was created which allows dynamic manipulation of the pipeline topology within the application.

2.4 Results and Discussion

The Myo architecture has evolved significantly since early functional prototypes of the system. To date, the Myo system has been used in over 200 electrophysiology procedures at the Cardiac Arrhythmia Unit at the Massachusetts General Hospital and at Homolka Hospital in Prague, Czech Republic. The system is a robust platform for simultaneously handling information to and from a variety of sources including electroanatomical mapping systems, RF ablation generators, data acquisition hardware, imaging systems, and remote catheter manipulation systems. The Myo system has been designed for easy and efficient user interactions during electrophysiology procedures and for flexible and powerful research capabilities. We will now present the major functions and features of the system.

2.4.1 Graphical User Interface

The Myo system was designed to be "data-centric", where data would be easily maniuplated by a user with a minimal number of menus to navigate. To create a data-centric application, the workspace of Myo system contains the MyoPatientTree, which includes top-level items for data, modules, settings, and tools (Figure 2-5). User interactions, such as loading data or performing a registration, are then added to the tree to allow for rapid manipulation

by a user. Manipulations can include globally altering the representation of data within all MyoWindows (see below) or establishing a connection with an external data source via TCP/IP network connection, serial port, or ActiveX object.

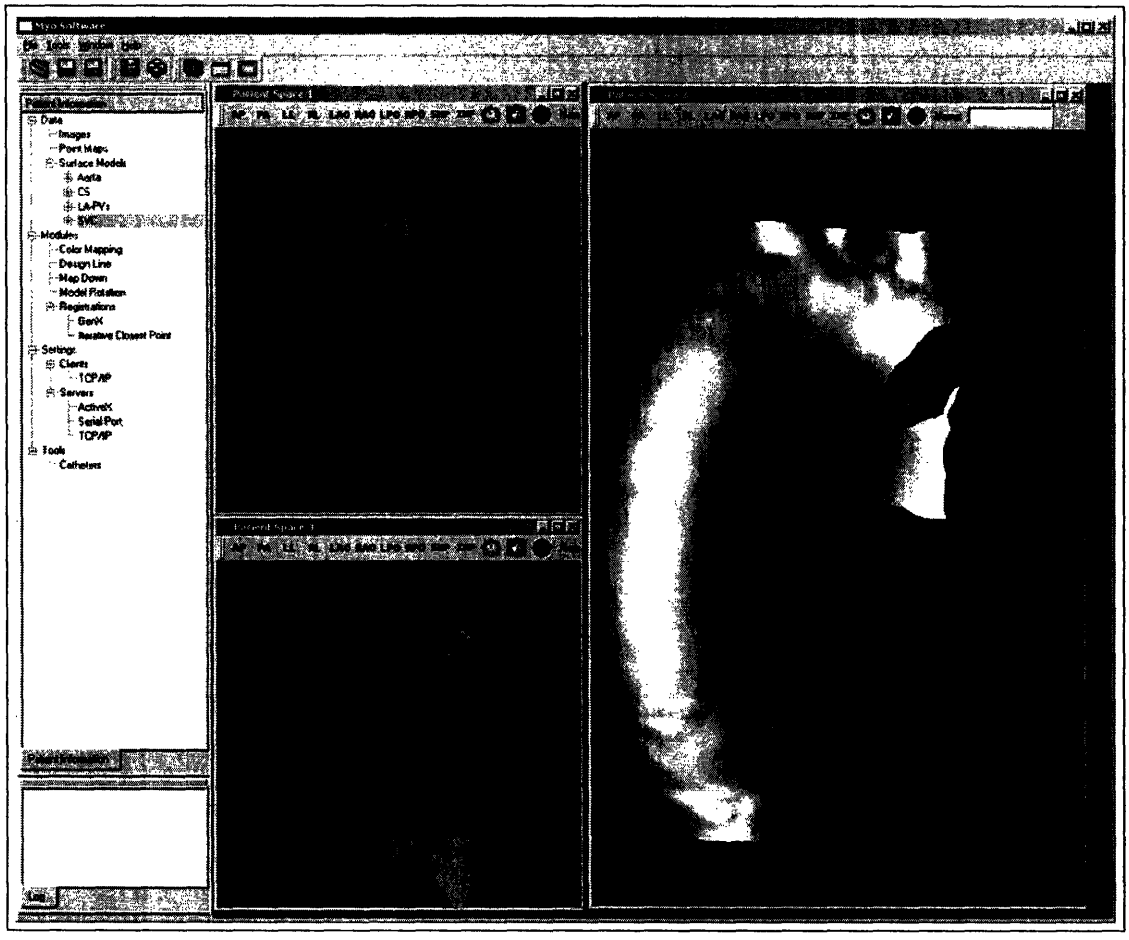

Figure 2-5: Myo Application. The Myo application is a data-centric program that supports a multiple document interface (MDI) for several different views of the same data. The left-hand portion of the application is the Patient Tree, which allows for rapid yet powerful interactions with patient data, client and server connections, and various modules for data processing within the application. The two windows contain several 3D surface models of various cardiac structures. At the top of each window, there is a toolbar which has preset anatomical views as well as functions for setting individual characteristics of the window and data seen each 3D window.

Interactions with the PatientTree are accomplished through context menus which appear when an object is right-clicked. These context menus are typically sub-classed from relevant but more generic context menus such that the sub-classed menu provides additional, specific options. The context menus have been designed such that most user-interactions

are limited to two-level menus. While the context menus minimize the clutter of the application workspace, the right clicking can sometimes be cumbersome when a large number of operations must be performed.

The Myo GUI also includes a log window, which text events from any module. These events report connection errors, indicate the completion of a threaded operation, and record results of data processing such as a performing a registration between two data types.

The Myo system supports the multiple document interface (MDI) style which allows a parent window to have many children window objects contained within the graphical space of the application. For convience within the electrophysiology lab, the Myo application was extended to support two operating modes for window layout, floating and integrated. During floating mode, the PatientTree is contained within an individual window, and all MyoWindows act as top-level windows, which permit screen layouts with other applications. When the windows are integrated, the PatientTree is docked on the left side of the application, and all MyoWindows are re-parented to be children of the MyoApplication. This feature allows for dual screen interactions where the electrophysiologists are able to see a screen with only MyoWindows showing the real-time combination of electroanatomical data and patient-specific imaging models while data operations are being perfomed on a separate screen.

In terms of serialization, the application contains methods for serialization of base data contained within patient tree. However, all derivative data such as a transformation resulting from a registration between pre-operative imaging models and intra-operative electroanatomical data is not stored currently. The application also has an auto-save feature which ensures that in the event of an unhandled exception, there will be minimal data loss.

2.4.2 Data Types

The Myo application has been designed to handle several data types, and the framework is easily extensible to incorporate additional types and sources of data. The major data types which the application currently supports include polygon surface model data in many common formats such as STL (stereolithography) models, imaging data using the DICOM standard medical imaging format, and manufacturer specific electroanatomical mapping information including interfaces to binary and ASCII mapping data files.

2.4.3 Visualization

The Myo system provides both 3D and 2D views of the various data types it handles. These views are provided by the MyoWindow class which accepts MyoVTKPipelines as inputs, but the MyoWindow allows a user to show different properties (color, representation, transparency) for each individual actor rendered within the window; this flexiblility allows for multiples views of the same data within each window. These views can include endoscopic views where a portion of the heart model is clipped away, exposing the endo-lumenal surface onto which RF ablation lesions are placed during a procedure.

Users can interact with the windows using a mouse to pan, zoom, and rotate the camera position. There are also preset anatomical views which are commonly used in the medical community (Anterior-Posterior, Left/Right lateral, Superior/Inferior, etc.). The user can also prescribe several clipping planes to review endoscopic (endo-lumenal) views of the patient-specific surface models. These views assist in accurate movement of the catheter within the chamber.

2.4.4 Registration

The original goal for the Myo system was to accurately register pre-operative, patient specific medical imaging data with intra-operative electroanatomical data. While extensive details and clinical results are presented in Chapter 3, we will review the registration functionality in terms of the Myo application. The Myo application is designed to provide registrations between: (1) electroanatomical mapping data and pre-operative CT or MR imaging information (2) different imaging data set (CT to MR, MR to MR, rotational angiography and MR or CT) and (3) different electroanatomical mapping systems (CARTO to LocaLisa).

In terms of the Myo application user interface, the Myo application allows for the creation of a hierarchy of registrations using the modified Iterative Closest Points (mICP) algorithm described in Section 3.3.2. Each node in the tree of the registration hierarchy represents a pairing of data (Figure 2-6). Children of nodes compute a registration using the mICP algorithm, which minimizes the error between the current data pair as well as all of the parent data pairs. Children of the root node can use previous registrations for initializations; however, the previous pairs are not recomputed during the subsequent reg-

istration step. Therefore, children of the root node only use the previous registrations as an initialization, not as a constraint.

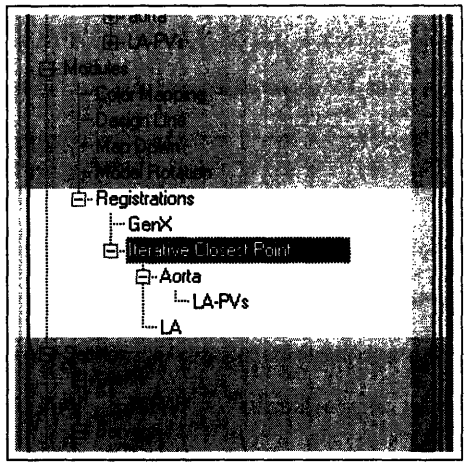

Figure 2-6: Myo Registration Hierarchy.

2.4.5 Modules

The Myo application consists of many modules which process, analyze, and modify the available information. We will now highlight several of the important modules within the application.

Warping

Methods for warping are discussed in detail in Chapter 4; however, relevant aspects of these methods and their use within the Myo application will be reviewed here. Warping or multivariate scattered data interpolation is used to deform the pre-operative surface models to more closely align with the registered electroanatomical mapping data. The residual differences between mapping and imaging datasets can be attributed to biological variations such as respiration, hydration, cardiac rate and rhythm. The algorithms used within the Myo application make use of several classes of radial basis functions, which depend solely on the Euclidean distance between the source point and target point. The resulting transformation is then applied to the entire surface model. As described in Chapter 4, warping via radial basis functions can be represented succinctly linear system of equations. Two significant advantage of these methods include continuity of the deformation across the surface model and computational efficency of these warping algorithms.

Coloring

Data interpolation is another important feature within the Myo application. Electroanatomical mapping points from the CARTO system are annotated with relevant electrophysiological information including local activation time (LAT), maximum unipolar voltage, and maximum bipolar voltage. However, electroanatomical mapping results in a relatively sparse sampling of the endocardial or epicardial surfaces of the heart. Therefore, interpolation methods are needed to represent data trends across the surface models.

Following a registration, the Myo application allows for this information to be mapped on the patient-specific surface model by two algorithms: volumetric and geodesic. Both algorithms for multivariate interpolation are based on Shepard's method, which is an inverse-distance weighting interpolation scheme [46]. The interpolation is calculated using the equation:

$$F(x,y) = \sum_{i=1}^{n} w_i f_i \tag{2.1}$$

where n is the number of points in the set being interpolated, f_i are the scalar values at each point, and w_i are the weights assigned to each point. In the classical form of Shepard's methods, the weighting function is given by:

$$w_i = \frac{h_i^{-p}}{\sum_{j=1}^{n} h_j^{-p}} \tag{2.2}$$

where p is the "weighting exponential" and is typically equal to 2. The parameter h_j is the distance metric. For the volumetric version of the interpolation algorithm, the distance metric is simply the Euclidean distance in three-space, give by:

$$h_i = \sqrt{(x-x_i)^2 + (y-y_i)^2 + (z-z_i)^2} \tag{2.3}$$

In the geodesic version of the algorithm, the geodesic distance is used for the distance metric. Geodesic distance is defined as the shortest path between two points in a connected domain. To calculate the geodesic distance, a modified version of Dijkstra's greedy breadth-first search algorithm is used. While the volumetric calculation requires much less computation, the algorithm is not ideal for regions of the patient-specific model with high curvature, such as the ridge between the left atrial appendage and left superior pulmonary vein (Figure 2-7). In regions of high curvature, the surface distance between two points is

Figure 2-7: Myo color mapping. In this posterior-anterior (PA) view of the left atrium, the Myo software has created a color interpolation from the maximum bipolar voltage annotations recorded at the white points on the surface of the atrium model. The color mapping

much larger than the Euclidean distance measured directly between the points. The combination of this data has interesting implications for more advanced processing and analysis of electrophysiology information.

Catheter

The catheter module is responsible for rendering of the real-time catheter position and orientation. This module has evolved to address an on-going problem encountered in surgical planning and image-guided therapies: depth perception. While there are many commercial systems available to create 3D effects using stereoscopic shutter glasses, polarized glasses, or anaglyphic (red/blue) glasses, these methods are largely impractical in the electrophysiology laboratory due to the procedure length, multiple information sources (Figure 2-1), and resulting eye strain. While auto-multiview monitors are an emerging technology with strong potential for 3D visualization, the technology remains expensive, and there is need for development of efficient methods for real-time rendering to these monitors.

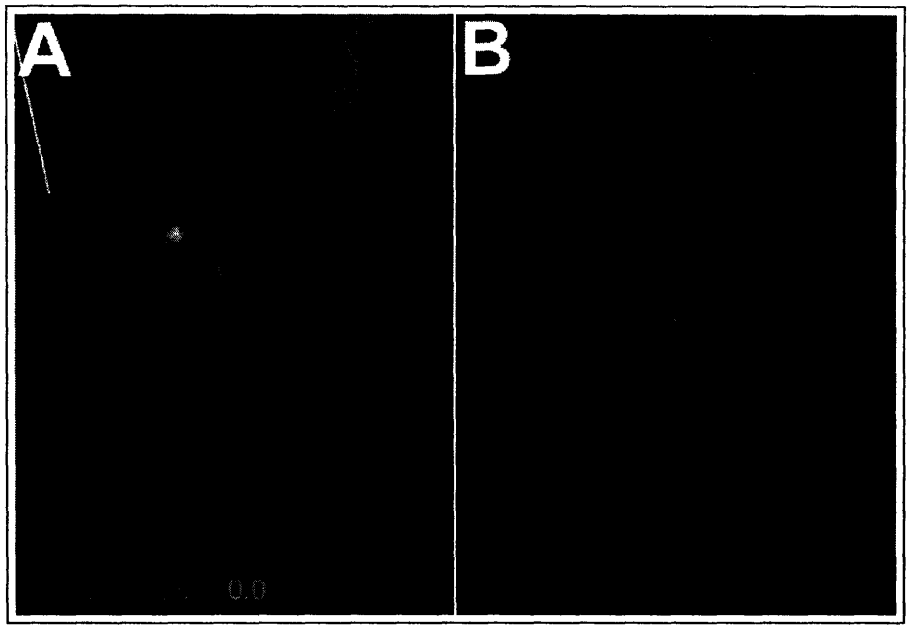

Figure 2-8: Myo catheter visualization.

To improve depth perception of the 3D visualization being rendered on a 2D monitor, we have incorporated several methods into the catheter module. First, the catheter has a 2D semi-transparent projection displayed on the viewport in front of the 3D render scene. Therefore, this projection is always visible even when the catheter is obscured by other objects within the scene, such as the patient-specific anatomical imaging model. When the catheter protrudes through and obscuring surface, the 3D rendering is visible to the operate, and it largely obscures the 2D translucent projection (Figure 2-8).

In addition to the catheter projection, the Myo system has several other methods to assist in visualization of the catheter within the patient specific models. The "Tip-to-surface" measurement is real-time calculation and visualization of the distance between the catheter tip and the closest point on the select surface model. Every time the catheter position is updated, the Euclidean distance to the closest surface point is recalculated, and it is displayed as both a numeric value (in millimeters) as well as with a small, bright color sphere located on the surface model (Figure 2-8). The Myo application also has the ability to create a spline to represent the shaft of the catheter; this method is useful to identify the position of the catheter shaft. However, it is limited in its accuracy, as the spline is calculated from a small number of control points at the transseptal puncture location. If additional

position information of the proximal catheter shaft was provided by the electroanatomical mapping system or via another means, the accuracy and usefulness of this method could be greatly improved.

Map Down and Design Line

Similar to the warping methods described above, the Map Down module is used to perform a point-wise movement of electroanatomical points. During this operation, one or more electroanatomical point sets are chosen. For each point contained within the point sets, the closest point on the target surface model is determined, and each point is translated to reside at the closest point on the surface model. The effect of this non-linear filter is largely visual; from internal (endoscopic) and external views of the surface models, the electroanatomical points are visible. However, a major limitation of this method is the fact that the catheter movements are not effected, and therefore, can be confused by the transformed points.

The Design Line module allows for pre-operative surgical planning to be performed on the patient-specific imaging models. This feature can be used to chose an optimal ablation lesion while minimize the risk of pulmonary vein stenosis and the number of necessary RF ablations.

2.4.6 MyoApps

The MyoAPI, which has been described above, has been used to derive several applications related to the Myo application. These applications can be executed on a single workstation or distributed among many workstations to increase available computational power. A short description of these applications will be include. For additional details, the reader is referred to [47].

Ablation

Currently, the Ablation application interfaces with the Stockert 70 radio frequency (RF) ablation generator via a serial port connection to the Global Port interface. After the program registers itself with the Global Port, measurements of power, catheter tip temperature, impedance, and voltage are reported every 100 ms. In addition to these standard parameters, derived parameters including the derivative of impedance with respect to time are reported. Through real-time communication and synchronization between both the EAM system and the RF generator, the "RF Pepper" function represents each ablation lesion not a single operator chosen point but as distribution of points representing the catheter

location over the entire RF lesion application. This functionality aims to provide a more accurate assessment of lesion formation by including the small catheter movements which are not reflected by operator-selected points which typically represent the prescribed ablation lesions. Further extensions of the ablation application are being made which model ablation lesion formation based on the parameters reported by the RF generator.

Signal

To perform advanced signal processing on electrogram data, a MyoAPI-derived application was designed to interface with a 16-channel data acqusition PCI card (NI-6220, National Instruments). This application provides real-time display of the digitized electrograms. In addition, it allows for variable-length recording of these signals, which can be subsequently processed using fast fourier transforms, signal averaging, cross-correlation, and additional methods. This application can send this information back to the Myo application, which can annotate electroanatomical mapping point data with this additional information.

Imaging

The Myo Imaging application is still under active development. Currently, the application allows for loading of DICOM imaging data. The application provides basic imaging view capabilities, and segmentation capabilities are being prototyped and implemented within the application. While the target of the imaging application is segmentation, the application will also communicate with the main Myo application for catheter position. Using this catheter position information with the registration between imaging data and mapping data, the Myo Imaging application will provide multi-slice reconstruction views showing the location of the mapping catheter within the imaging volume.

In conclusion, the Myo application is a extensible platform for integration, processing, and visualization of wide variety of information for cardiac electrophysiology procedures.

Chapter 3

Registration Strategies

3.1 Introduction

Registration is a process to determine a spatial transformation which will bringing corresponding points being registered into alignment. In terms of catheter ablation of cardiac arrhythmias, registration is performed to align the pre-operative imaging information with the intra-operative electroanatomical mapping information. In the ideal situation, the registration process would be fast, accurate, simple, and completed at an early stage of the intervention.

In this chapter, our focus will be on our main clinical strategy, which uses the aorta as a constraint for registration. We formalize the problem of image registration in the context of combining pre-operative imaging data with intra-procedural electroanatomical mapping data beginning with an outline of the workflow for registration. We will then compare strengths and weaknesses of multiple registration strategies and methodologies using both *in vitro* and *in vivo* data from phantoms, pre-clinical, and clinical procedures. Throughout this chapter, we will identify limitations and clinical considerations which may affect the registration process or complicate the clinical workflow.

3.2 Clinical Workflow

Image integration or registration of pre-operative MR/CT imaging data with intra-procedural electroanatomical mapping information is a multi-step process (Figure 3-1). These steps include: 1) image acquisition 2) segmentation 3) catheter mapping 4) registration 5) error

analysis evaluation and 6) visualization. It is important to examine each step within this workflow, as the accuracy of a registration is dependent on the preceding steps.

3.2.1 Physiological Variables

Throughout the entire workflow, there are patient-specific physiological variables which must be considered. Per patient variation of 1) heart rate 2) heart rhythm and 3) respiration between the steps in the clinical workflow defined above can decrease the overall accuracy of the resulting registration. To minimize motion-related artifacts, electroanatomical mapping is performed at end-diastole, the moment at which the heart muscle is relaxed and full of blood but before it contracts. Variations of heart rate and rhythm can affect end diastolic chamber volume, which would result in an altered representation in terms of size of the chamber during image acquisition and subsequent segmentation of the imaging data. In addition, an arrhythmia such as atrial fibrillation results in an irregular spacing between ventricular heart beats; therefore, cardiac gating of CT or MR image acquisition based on the 12-lead ECG is difficult. The resulting images may contain problems such as cardiac motion artifacts.

The effects of respiration on the registration process are another important consideration. During an average cardiac CT or MR imaging study, a patient is instructed to hold his/her breath at end-inspiration, which approximates total lung capacity. This maneuver has several important effects on the registration process and on the resulting anatomical representation [48]. Electroanatomical mapping is typically performed during "quiet" respiration, and map points are acquired at end-expiration, which approximates the functional residual capacity of the lungs. In terms of registration, when a patient inspires, the heart translates anterior and inferior within the thorax. This movement alters the geometric relationship between the heart and the great cardiac vessels such as the aorta and superior vena cava. In addition, respiration has an effect on the geometry at the ostium of the pulmonary veins entering the left atrium.

3.2.2 Image Acquisition

For anatomical information, the choice of imaging modality is dependent on the radiology department at an individual's institution and any patient specific contraindications such as pacemaker or ICD implant, renal insufficiency, or contrast allergy. Both MR and CT

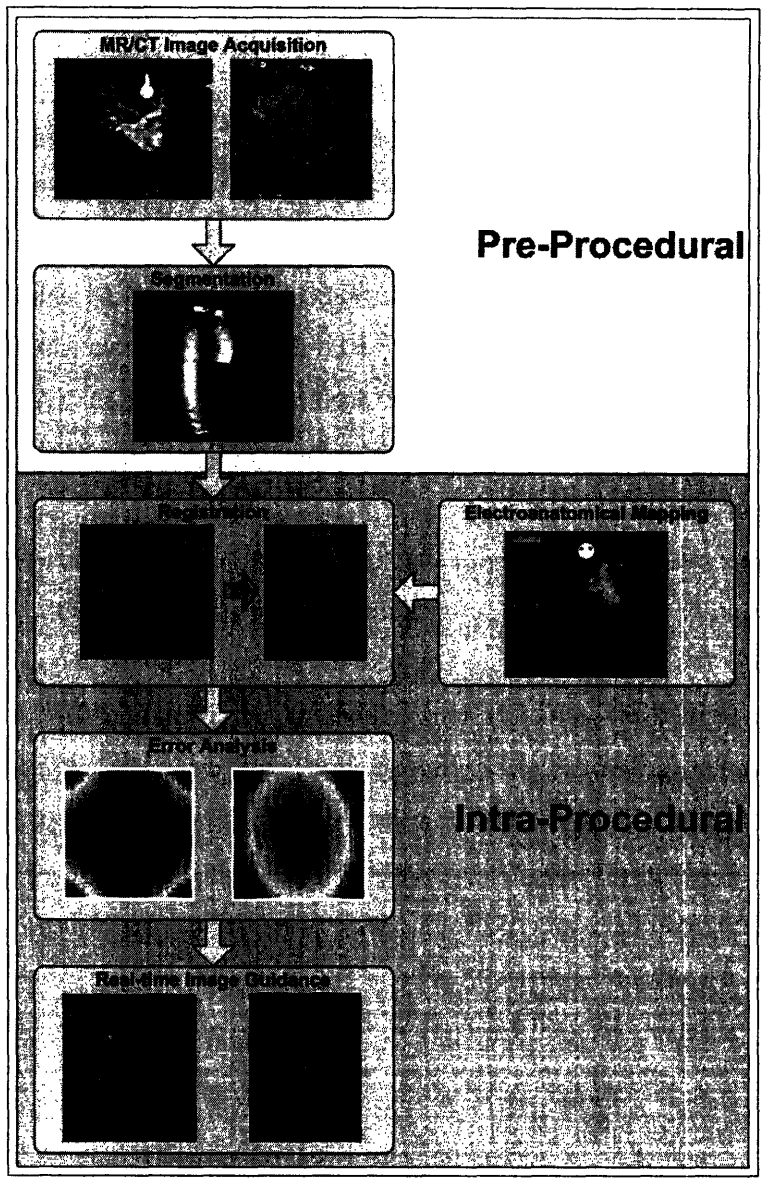

Figure 3-1: Registration workflow. The figure outlines the important steps for the registration electroanatomical mapping data with pre-operative imaging for catheter guidance. After the pre-operative CT or MR imaging data is acquired, the data is segmented offline for the relevant cardiac chambers and vascular structures. During the electrophysiology intervention, electroanatomical mapping is performed to define chamber geometry and underlying pathophysiology. Ideally, registration between the imaging and mapping would be performed early in the procedure. Following the registration process, it is important to understand the accuracy of the registration (Error Analysis). Following the registration process, catheter-based ablation is performed within the patient-specific anatomy provided by the pre-operative imaging information.

imaging provide high resolution data for segmentation, registration, and subsequent catheter guidance.

Magnetic Resonance Imaging

For catheter mapping and ablation within the left atrium, 3D contrast-enhanced MR angiography (MRA) is performed to delineate the endocardial boundaries of the left atrium and pulmonary veins. The scans are typically performed in a 1.5 Tesla (T) cardiac MR system using gadolinium-DPTA as a contrast agent (Signa CVi 1.5T, GE Healthcare, Waukesha, WI). This imaging sequence is not cardiac-gated; therefore, the resulting imaging information is an average over the cardiac cycle; however, in our experience, it does not grossly affect the geometric representation of the left atrium or subsequent registration.

Computed Tomography Imaging

Computed tomography, or computed axial tomography, uses two-dimensional x-ray images from a large number of rotational angles about a subject to compute three-dimensional imaging information. Modern cardiac CT systems accelerate image acquisition through the use of solid-state multiple detector arrays. These 4-, 16-, 32-, and 64-"slice" CT scanners can acquire the entire thoracic cavity in a single 10-second breath hold. The reconstructed image volume has an average voxel size on the order of 0.5 mm x 0.5 mm x 0.3 mm. The high resolution and rapid acquisition times have made CT imaging popular for cardiac related imaging including coronary artery obstruction. In addition, pacemakers, ICDs, and other implants are not contraindicated by CT imaging. However, CT imaging does use ionizing radiation, and in terms of radiation dose, one multi-detector CT imaging examination (6.7-13.0 mSv, effective radiation dose) is equivalent to approximately 500 chest X-rays (0.02 mSv) [49].

For the pre-operative imaging information required for registration with electroanatomical mapping, studies were performed on 16- and 64-slice CT scanners using an iodinated contrast agent bolus via peripheral intravenous (IV) access (Sensation 16 and Sensation 64, Simens Medical Solutions, Erlangen, Germany). CT reconstruction were then performed at the cardiac phase most closely approximating end-diastole of the chamber of interest.

3.2.3 Segmentation

Following image acquisition, the imaging information is segmented to extract surface representations of relevant anatomical structures such as the endo-lumenal (inner) surface of the

left atrium or left ventricle, the epicardial (outer) surface of the ventricles, the aorta, and the coronary arteries and veins. Segmentation of imaging data can be performed with a variety of commercial and academic software packages. Segmentation is typically a multi-step process. The image processing can include smoothing, edge enhancement, thresholding, and morphology operators. Applications of segmentation include image-guided intervention or surgery, surgical planning including trajectory planning and prosthesis construction, therapeutic evaluation, and functional evaluation. The segmentation process can be manual, semi-automated, or automated; however, in most instances, even the best "automated" segmentation systems still require human input. Manual segmentation is time consuming, and it is prone to inter- and intra-operator variability even when performed by experts. Semi-automated and automated methods use a variety of methods leveraging statistical classification techniques and use of *a priori* information.

For the registration work presented here, a research tool (Cardiac++) from GE Global Research was used for segmentation under internal review board (IRB) approval at the Massachusetts General Hospital. Cardiac++ provides manual methods for thresholding, region of interest cutting, per-slice masking, and a semi-automated method using a combination intensity and morphology operator known as the bubble wave [50]. The bubble wave is designed to segment continuous vascular structures, which is ideal for the application under consideration here. Seeds are placed within the structure of interest, and the algorithm attempts to find all connected regions which pass both the intensity and morphology criterion. After performing operations on the slice data, a 3D object is then created, and cut can be applied from different view angles to eliminate unwanted structures.

3.2.4 Electroanatomical Mapping

The reader is referred to Chapter 1 for an overview to electroanatomical mapping; however, methods and techniques for catheter-based electroanatomical mapping are largely beyond the scope of this dissertation. We will discuss several key aspects which must be considered with regards to image integration. In terms of respiratory effects, map points should be acquired at the end of quiet expiration, and in areas which are particularly sensitive, it is often helpful to have the patient hold his/her breath at the end of quiet expiration to minimize respiratory effects.

Chamber deformation from catheter manipulation is another concern during electroanatom-

ical mapping. There is relatively little tactile feedback for an electrophysiologist to determine catheter contact with a region of interest. Since static pre-operative images are being used during registration and to render patient-specific anatomy, catheter deformation of the chamber can effect the registration process and cause confusion when using the imaging data for catheter guidance. In regions of scarred or thinned myocardium, small catheter forces against the surface of the heart can result in large (1-2 cm) deformations of the anatomy, which adversely impact the registration process [51].

Aorta EAM Acquisition

Based on *in vitro* and *in vivo* experiments comparing internal versus external fiduacial structures for registration, our main strategy for fusion of EAM and MR/CT data is through the use of vascular structures as internal fiducials [52, 53]. For this clinical strategy, mapping the descending and ascending aorta is performed after gaining percutaneous access to the femoral artery (Figure 3-2). While the description here explicitly references the aorta, these methods and concepts are easily adaptable for the mapping of any vascular structure as an aid for registration. Additionally, the method presented here has been optimized for speed, accuracy, and ease of point acquisition; however, if erroneous points are acquired, they can be deleted individually before computing the registration.

Prior to acquiring the first electroanatomical mapping point, it is important to understand the spatial extent of the aorta that has been segmented from the pre-operative imaging information. Catheter mapping points must only be acquired within the extent of the aorta represented by the segmented model, as this data can adversely effect the results of the registration algorithms employed here. It is often helpful to acquire two points - one point defines the inferior boundary and the other defines the start of the aortic arch. These points can then serve as guides in the next steps.

To acquire the descending portion of the aorta, the catheter is advanced up the descending aorta to the beginning of the aortic arch. The tip of the catheter is then deflected in one of four "cardinal" directions to maintain contact with the vessel wall in this general order: 1) anteior 2) left lateral 3) posterior and 4) right lateral (Figure 3-2). The catheter is slowly withdrawn, and EAM points are acquired as it moves towards the inferior boundary point acquired initially. This process is repeated for each of the four directions indicated above.

To complete the EAM point acquisition, the arch of the aorta is mapped in a similar

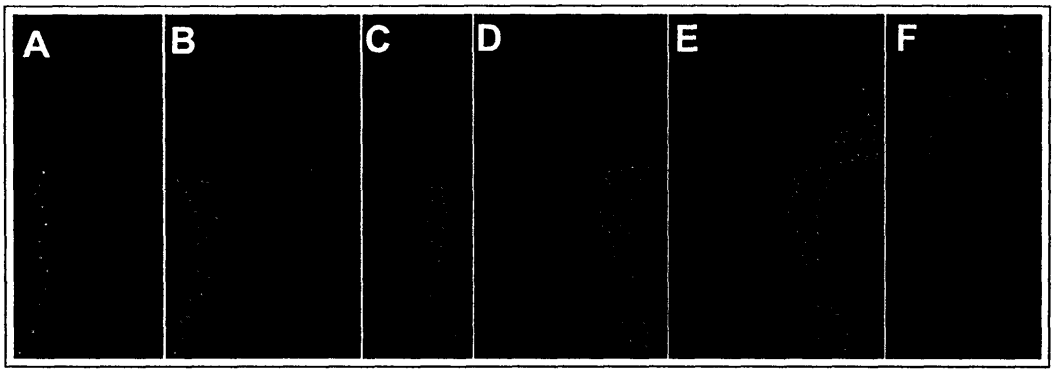

Figure 3-2: Acquisition of EAM points within the aorta. The frames depict a simple, reliable method to facilitate the electroanatomical mapping of the aorta (or other vascular structures) for use during the EAM-imaging registration process. To acquire the aorta, the catheter is advanced retrograde to the based of the aortic arch. The catheter tip is then deflected in one of four directions: anterior (A), left lateral (B), posterior (C), or right lateral (D). After deflecting the catheter tip, the catheter is slowly retracted, and points are acquired. The process is then repeated for the remaining directions. After acquiring the descending aorta, the ascending aorta (E) is acquired in a similar fashion. This EAM data (F) is then used to register to the EAM data to the segmented imaging data.

fashion. The catheter is advanced towards the aortic root with care taken to stay within the boundary of the segmented model of the aorta. Points are then acquired with the catheter tip deflected toward the lateral, inferior, and superior walls of the aortic arch. However, with the superior deflection and withdrawal of the catheter within the arch, there is a tendency for the catheter to "jump" into the brachiocephalic, subclavian, or common carotid arteries, which depart the aorta at the superior aspect of the aortic arch. To avoid acquiring points within these structures, the catheter can be deflected in an superior-lateral direction. Finally, respiratory effects must also be considered when mapping the aortic arch.

3.3 Registration

Registration is the general term for the process of aligning two sets of data, U and V, to an underlying, common coordinate space. In an abstract sense, a registration problem is one by which parameters are determined to optimize some a cost functional between the two data sets (Figure 3-3). The resulting registration is often a spatial transformation between two disparate coordinate systems. Registration is used in a wide variety of medical applications including multi-modal image fusion, time-varying series processing, warping (see Chapter

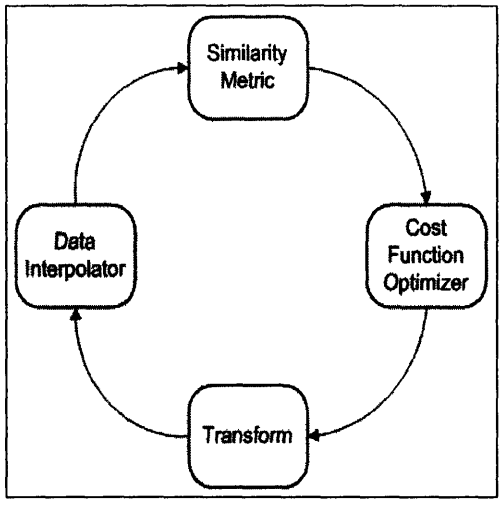

Figure 3-3: Conceptual registration framework.

4).

Depending on the algorithm and parameters, the registration may be closed-form by which the solution can be calculated with a single iteration over the framework. The solution may also be found iteratively, such that the algorithm continues to minimize the cost function within the registration framework until a stop criterion such as an minimum error threshold is reached.

The type of resulting spatial transformation used for transformation between the data should be chosen based on the characteristics of the system and the registration problem being addressed. In general, there are three types of spatial transformations used for registration. The transformations are composed of translations, rotational, and scaling parameters, which can be compactly represented as a single homogenous 4×4 matrix.

$$\begin{bmatrix} x\prime \\ y\prime \\ z\prime \\ 1 \end{bmatrix} = translations * yaw * roll * pitch * scaling \begin{bmatrix} x \\ y \\ z \\ 1 \end{bmatrix} \tag{3.1}$$

$$\begin{bmatrix} x\prime \\ y\prime \\ z\prime \\ 1 \end{bmatrix} = \begin{bmatrix} \cos\theta_z \cos\theta_y & \cos\theta_z \sin\theta_y \sin\theta_x - \sin\theta_z \cos\theta_x & \sin\theta_z \sin\theta_x + \cos\theta_z \sin\theta_y \cos\theta_x & t_x \\ \sin\theta_z \cos\theta_y & \cos\theta_z \cos\theta_x + \sin\theta_z \sin\theta_y \sin\theta_x & \sin\theta_z \sin\theta_y \cos\theta_x - \cos\theta_z \sin\theta_x & t_y \\ -\sin\theta_y & \cos\theta_y \sin\theta_x & \cos\theta_y \cos\theta_x & t_z \\ 0 & 0 & 0 & 1 \end{bmatrix} \begin{bmatrix} x \\ y \\ z \\ 1 \end{bmatrix} \tag{3.2}$$

Rigid-Body Model In 3-dimensional space, a rigid body transformation consists of six parameters which allow for rotation and translation within the coordinate system. Using such a transformation, an assumption is made that the coordinate spaces are of the same spatial scale. It should be noted that the order of the rotations is not, in general, commutative; a rotation about the x-axis, then y-axis, then z-axis does not equal a rotation about z-axis, then the y-axis, and then the x-axis. This class of spatial transformation is also length preserving.

Global Rescaling Transformation This transformation is very similar to the rigid-body model transformation; however, in addition to the six-degrees of freedom discussed above, a seventh parameter is included which specifies an isotropic or global scaling factor.

$$\begin{bmatrix} m & 0 & 0 & 0 \\ 0 & m & 0 & 0 \\ 0 & 0 & m & 0 \\ 0 & 0 & 0 & 1 \end{bmatrix} \tag{3.3}$$

Affine Model The nine-parameter affine model allows for anisotropic rescaling along the three cardinal axes. In this case, the scaling matrix is represented by:

$$\begin{bmatrix} mx & 0 & 0 & 0 \\ 0 & my & 0 & 0 \\ 0 & 0 & mz & 0 \\ 0 & 0 & 0 & 1 \end{bmatrix} \tag{3.4}$$

There are additional methods for warp transformation and locally-varying transformations. These methods allow for non-linear variation over different regions of space. The reader is referred to Chapter 4 for further details specifically dealing with interpolation using elastic transformations. Other parametric transformation classes use finite element methods.

There are two classes of objective function used for evaluation during the registration process: 1) intensity-based or 2) model-based. Intensity-based objective are commonly used for intra- and inter-modality image registration. These type of functions measure the agreement between two pixels or voxels based on their intensities. Model-based registration

methods are commonly used to align information based on global and local shape information. The objective function is usually based on a distance criterion (chamfer distance). Model "mismatch" is one limitation of model-based objective functions; if a significant portion of a structure is missing, a large penalty will adversely affect the registration process.

3.3.1 Iterative Closest Points Algorithm

The iterative closest point (ICP) algorithm is commonly used for rigid registration of imaging-derived models. The ICP algorithm minimizes the sum of squares distance between two data sets via an iterative descent method until a convergence criterion is met or an iteration limit is exceeded [54]. From Besl and McKay, the algorithm is stated [54]:

- The source point dataset P with N_p points $\{\vec{p_i}\}$ and model shape target X consisting of geometric primitives (with N_x points, lines, and triangles) are given.
- Initialize the iteration by setting $P_0 = P$, $\vec{q_0} = [1, 0, 0, 0, 0, 0, 0]^t$, and $k = 0$. The following Steps 1-4 are performed until convergance within a tolerance τ or the maximum iteration limit is exceeded:
  1. Compute the closest points: $Y_k = C(P_k, X)$
     Cost: $O(N_p N_x)$ worst case; $O(N_p log N_x)$ average
  2. Compute the rotation: $(\vec{q_k}, d_k) = Q(P_0, Y_k)$
     Where $(\vec{q}, d) = Q(P, Y)$ is the least squares registration.
     Cost: $O(N_p)$
  3. Apply the registration: $P_{k+1} = \vec{q_k}(P_0)$
     Cost: $O(N_p)$
  4. Check convergence criterion and iteration count versus iteration limit where mean-square error falls below preset threshold ($\tau > 0$) such that the precision of the registration is $d_k - d_{k+1} < \tau$

In general, the ICP algorithm is extremely fast; however, it does have certain limitations. The algorithm works in an iterative-descent type fashion, which tries to minimize the error metric at each step. Therefore, the capture range of the algorithm is limited; if the initialization is not reasonably close to the final solution, the algorithm will converge

on local-minimal solutions instead of the global minimum. The original implementation proposed by Besl and McKay noted the limitation of the ICP algorithm to robustly handle outliers or unequal uncertainty among points [54]. There have been several extension to the original ICP algorithm including regional weighting, outlier classification, and the robust generalized total least squares ICP method [55, 56, 57, 58, 59].

3.3.2 Modified Iterative Closest Points Algorithm

We propose a modified iterative closest point (mICP) algorithm to improve convergence of the registration process in its application to pre-operative image integration in cardiac electrophysiology. The modification is the addition of class information into the algorithm. Classes are assigned to both the point data acquired during electroanatomical mapping of different regions of the heart and great cardiac vessels as well as during image segmentation and 3D surface model reconstruction. A hierarchy of registrations can then be performed; at each point in the hierarchy, a source-target pair is assigned. The mICP algorithm then iterates to minimize the overall sum squared error; however, at each step, the source-target distance (error) is calculated only within the source-target class assignment.

For example, electroanatomical mapping is performed in the left atrium as well as in the aorta, which represents two classes of EAM point information. Likewise, the pre-operative CT or MR imaging data is segmented for these same structures; however, two separate structures are created to reflect the two EAM point classes. In the subsequent registration process, the mICP algorithm simultaneous optimizes the point-to-surface error of the aorta data and the point-to-surface error of the left atrium data.

In terms of the ICP algorithm statement above, the mICP algorithm can be stated as follows:

- One or more pairs of source point dataset P_i with N_{p_i} points $\{\vec{p_i}\}$ and model shape target X_i consisting of geometric primitives (with N_{x_i} points, lines, and triangles) are given:

- Initialize the iteration by setting $P_0 = P$. $\vec{q_0} = [1, 0, 0, 0, 0, 0, 0]^t$, and $k = 0$. The following Steps 1-4 are performed until convergance within a tolerance τ or the maximum iteration limit is exceeded:

  1. For each source-target pair, compute the closest point within the pair: $Y_k =$

$C(P_k, X)$

Cost: $O(N_p N_x)$ worst case; $O(N_p log N_x)$ average

2. Compute the rotation: $(\vec{q_k}, d_k) = Q(P_0, Y_k)$

   Cost: $O(N_p)$

3. Apply the registration: $P_{k+1} = \vec{q_k}(P_0)$

   Cost: $O(N_p)$

4. Check convergence criterion and iteration count versus iteration limit where mean-square error falls below preset threshold ($\tau > 0$) such that the precision of the registration is $d_k - d_{k+1} < \tau$

3.4 Clinical Registration Strategies

To assess the accuracy of the registration methods described above, a series of *in vitro* and *in vivo* studies were performed. In this first study, the registration methods will focus on registration strategies for the left atrium for use during a catheter-based pulmonary vein isolation. The second study will focus on registration strategies for the endo-lumenal surface of the left ventricle for use during ventricular tachycardia ablation. The third study will explore registration strategies for use during epicardial ablation, that is ablation performed on the outer surface of the heart which can be used during both atrial and ventricular ablation procedures.

3.4.1 Left Atrial Registration Strategies

Overview

To evaluate registration strategies for the left atrium, a three phase study was conducted. First, an *in vitro* study was performed using a 3D phantom constructed from a human MR imaging dataset. In the second phase, registration between pre-operative MR and CT imaging and catheter-based electroanatomical mapping data was *retrospectively* performed to assess the utility of curved vascular structures in the registration process. The third phase was a prospective *in vivo* clinical evaluation of a rapid registration strategy which uses the ascending and descending aorta to rapidly align the pre-operative imaging data with real-time catheter mapping information with minimal information required within the

left atrium. The clinical portions of this study were performed in accordance with the guidelines of the Massachusetts General Hospital Human Research Committee.

Atrial Phantom

A 3D cardiac phantom was created using standard solid-modeling and rapid prototyping methods. Briefly, a human MR imaging dataset was segmented for the left atrium, pulmonary veins, and aorta (Figure 3-5A). From this segmentation, 3D surface models were created, which were then embedded into a simple block. The surface model was positioned within the block to allow for access to the distal pulmonary veins, descending and ascending portions of the aorta, and the anterior portions of the left atrium via the mitral valve annulus (Figure 3-5B). A static, fully rigid phantom was then 3D printed using a starch powder and binder process (ZCorp, Burlington, MA).

Following phantom creation, the CARTO electroanatomical mapping system was used to acquire multiple mappings (n=5) of: 1) the endo-lumenal surface of the descending aorta 2) the endo-lumenal surface of the aortic arch and 3) the endocardial surface of the left atrium (Figure 3-5C).

Using the MR imaging data used to create the phantom as well as the catheter-based electroanatomical mapping information, registration experiments were performed using either the descending aorta or aorta including the arch of the aorta as the first step in the registration process. Following the aorta registration, EAM points within the left atrium were incrementally added to the registration process. That is, after each additional left atrial point, the registration was recalculated. The point-to-surface error statistics were calculated using a 30-50 point "validation set" within the atrium which were not used during the registration process (Table 3.1).

Retrospective Simulation Experiments

In this portion of the evaluation, patients underwent pre-procedural (1 day to 5 months prior) contrast-enhanced CT (n=13) or MR (n=25) angiography to image the left atrium, pulmonary veins, and additional structures. Because of its high spatial resolution, cardiac CT was used to image the coronary sinus (CS) and superior vena cava (SVC) (see Figure 3-7). These two peri-vardiac vascular structures were chosen because they can be readily mapped with a catheter and because both structures have branching structures which add unique information for the registration process. The SVC is minimally curved itself; however, the left brachiocephalic vein, which extends leftward, and the azygous vein which

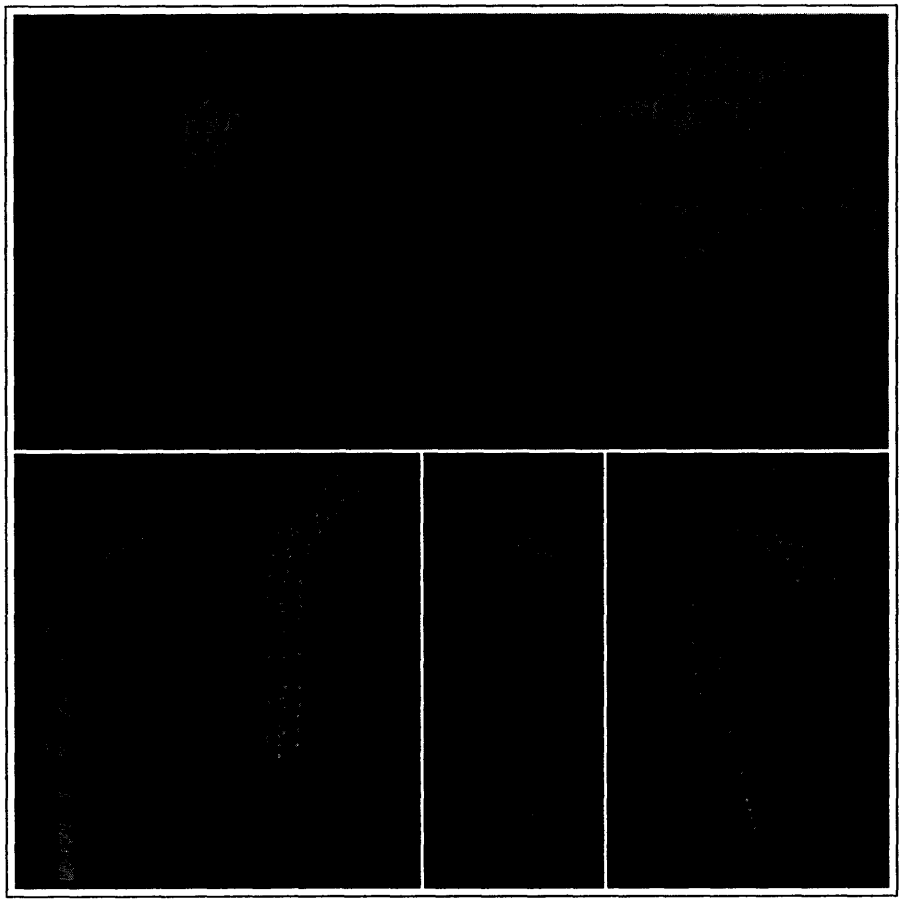

Figure 3-4: Atrial phantom registration. (A) MR imaging of the left atrium, pulmonary veins, and aorta were segmented and surface reconstructions were made. (B) A 3D phantom was then made from this patient-specific anatomy using rapid prototyping methods (C) Electroanatomical mappings (n=5) of the aorta (white points) and left atrium (green points) were then acquired. (D) Registration was then performed using the aorta for initial registration with the addition of (E) points within the left atrium.

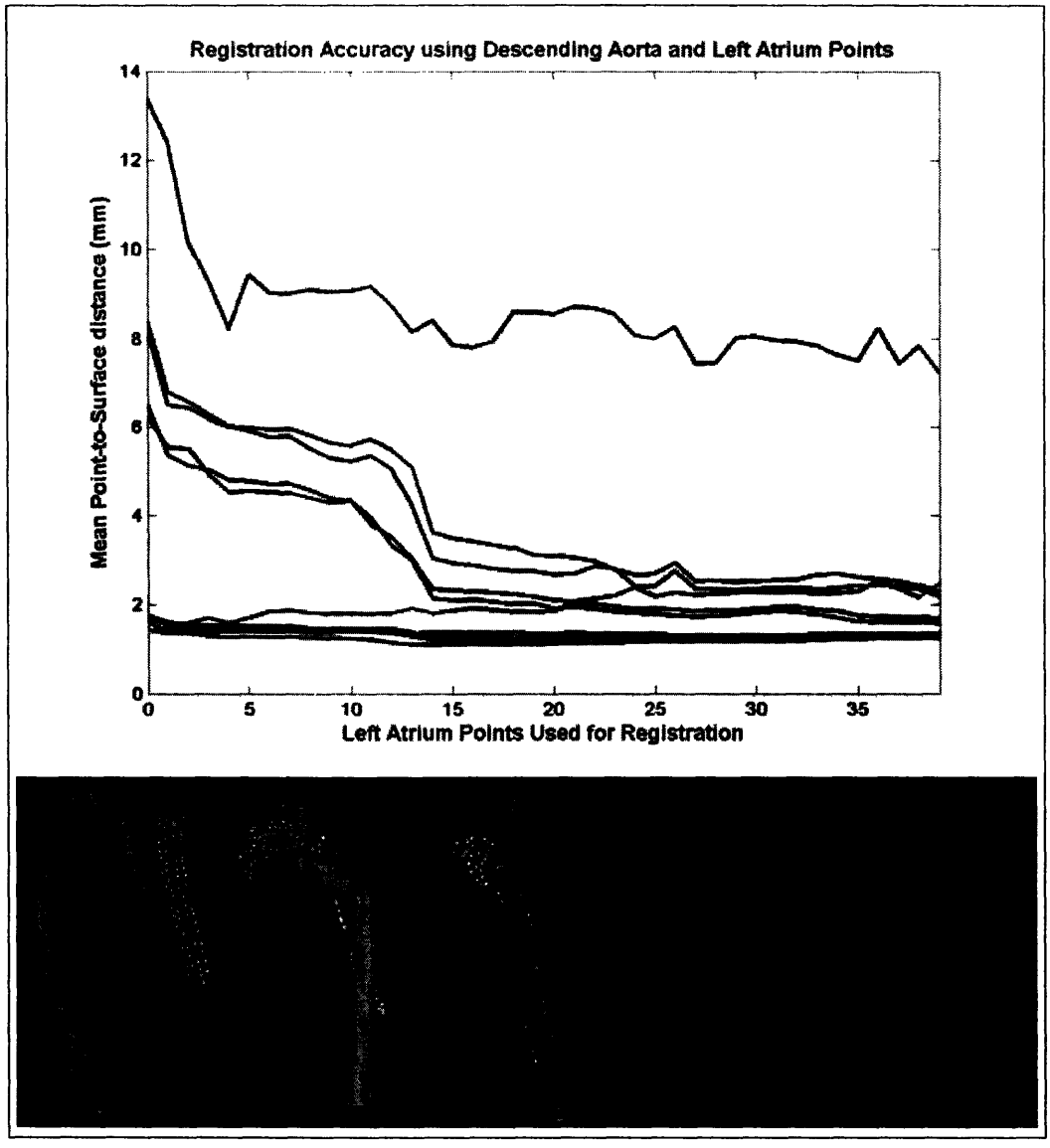

Figure 3-5: Atrial phantom registration simulations. Image integration was based upon registering the descending aorta points. Then, LA points were sequentially incorporated into the registration process (horizontal axis). The accuracy of registration (vertical axis) was defined as the mean distance of 30 additional LA points not included in the registration process (blue lines; the red lines represent the mean distance for the aorta points). Five simulations were performed. Note that inaccurate local minimal solutions occurred when using the descending aorta alone, requiring a number of LA points to correct (A). The bottom series of frames portray a representative registration using only information in the descending aorta. In frame (E) notice the location of the green atrium points with respect to the atrium.

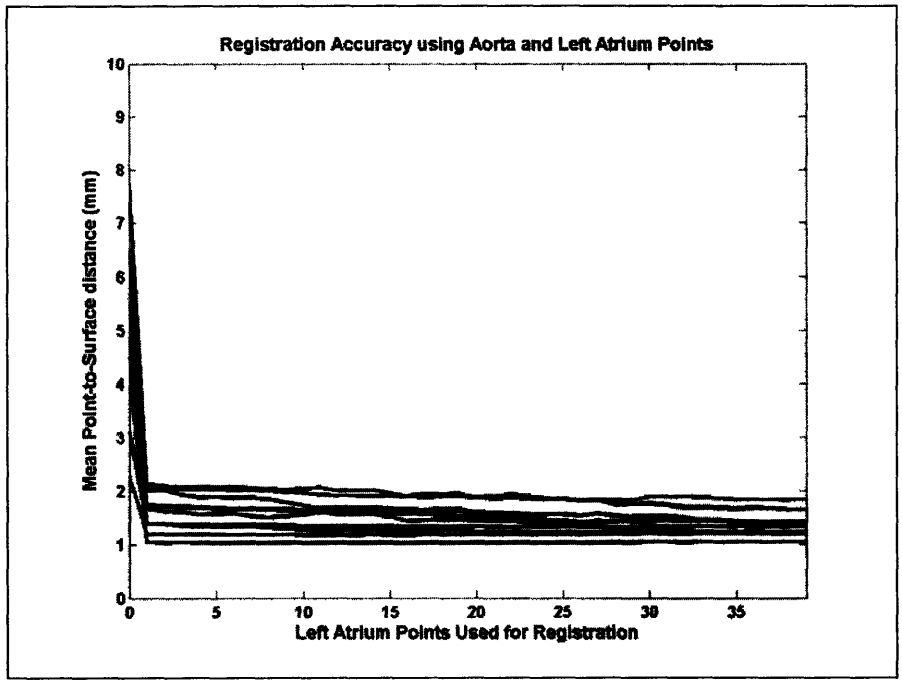

Figure 3-6: Atrial phantom registration simulations with aorta including arch. Five simulations were performed. Registration was initially computed using aorta including arch information. Then, LA points were sequentially added to the registration process (horizontal xis). The accuracy of registration was defined as the mean distance of 30 additional points within the left atrium, which were not used during the registration process (blue lines; red lines reprsent mean dstiance for the aorta points). Note the rapid convergance to a robust solution with minimal information from the left atrium (approximately 3 points).

Acquisition	Desc Ao Points	All Ao Points	LA Points	Reg. Error w/ Desc Ao + LA. Mean ± Std (mm)	Reg Error w/ All Ao + LA Mean ± Std (mm)
#1	67	172	5	9.80 ± 6.44	2.12 ± 1.44
#2	101	204	5	4.58 ± 2.99	1.63 ± 1.09
#3	101	250	5	5.65 ± 3.53	2.07 ± 1.27
#4	98	257	5	5.54 ± 3.40	1.87 ± 1.15
#5	84	221	5	4.38 ± 2.88	1.67 ± 1.12

Table 3.1: Atrial phantom registration strategies using the aorta. In these simulations, EAM data acquired from the phantom was registered to MR imaging data using one of two strategies: (1) register using descending aorta, then add 5 points within the left atrium and recalculate the registration and (2) register using all of the aorta, then add 5 points within the left and recompute the registration using the additional information. As can be seen in the results, there was significantly lower point-to-surface error (mm) when the aorta including the arch was used as a fiducial structure for registration. While the inclusion of additional left atrium points may increase the precision of the registration when using the descending aorta, the goal of image integration is a fast and accurate solution, which does not require extensive mapping within the chamber of interest.

extends posteriorly and inferiorly form the unique shape of the SVC. Likewise, the curvature of the CS as well as its proximity to the left atrium make it potential candidate for use during the registration process. The imaging data was then segmented to extract the relevant anatomical structures and 3D endo-lumenal surface reconstructions were made (see Section 3.2.3). The MR imaging data was segmented for the left atrium, pulmonary veins, and aorta including the ascending arch and descening portion within to the bottom of the heart shadow.

These patients subsequently underwent catheter-based pulmonary vein isolation for treatment of atrial fibrillation. During these interventions, pre-RF ablation mappings of the left atrium, pulmonary veins, and aorta were acquired using a 3.5 mm or 8 mm-tip radio frequency ablation catheter. Mapping of the aorta was performed via a femeral retrograde aorta approach (described in detail above in Section 3.2.4). In addition to the aorta, two additional vascular structures were chosen to as internal fiducial structures for the registration process: the coronary sinus (CS) and the superior vena cava (SVC) (Figure 3-8).

As seen in Figure 3-8, registration with only the aorta provides an accurate registration without additional information within the left atrium. In addition, with the incremental use of left atrium points, a registration based on the aorta changes in a minimal fashion.

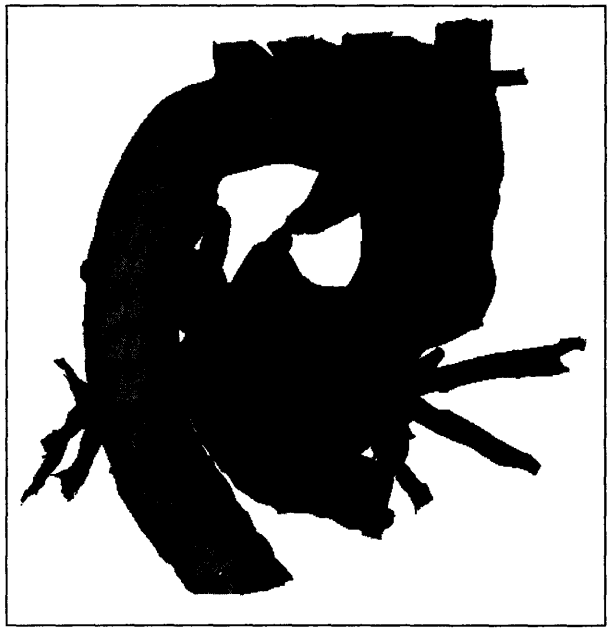

Figure 3-7: Left atrium and great cardiac vessels. A right posterior-oblique (RPO) view of the left atrium (blue), aorta (purple), superior vena cava (orange), and coronary sinus (green). Both the coronary sinus (CS) and the superior vena cava (SVC) are thin-walled venous structures while the aorta has thicker walls to handle the greater arterial pressues. These structural differences of the vessels may cause an increase residual error due to catheter deformation of the thin-walled structures.

Figure 3-8: Registration of LA using the great cardiac vessels. In the top three frames (A-C), registration between EAM and CT imaging models is performed using only the coronary sinus (green structure). In (B), the aorta points (purple), superior vena cava points (orange), and left atrial points (blue) are also shown to demonstrate the relatively poor registration resulting from only information within the coronary sinus. In the bottom three frames (D-F), registration is performed using only information from the superior vena cava (orange). In (E) and (F), points within the other structures are shown. The better performance of the SVC (D-F) for registration is likely related to the additional and unique information from the azygous and brachiocephalic veins.

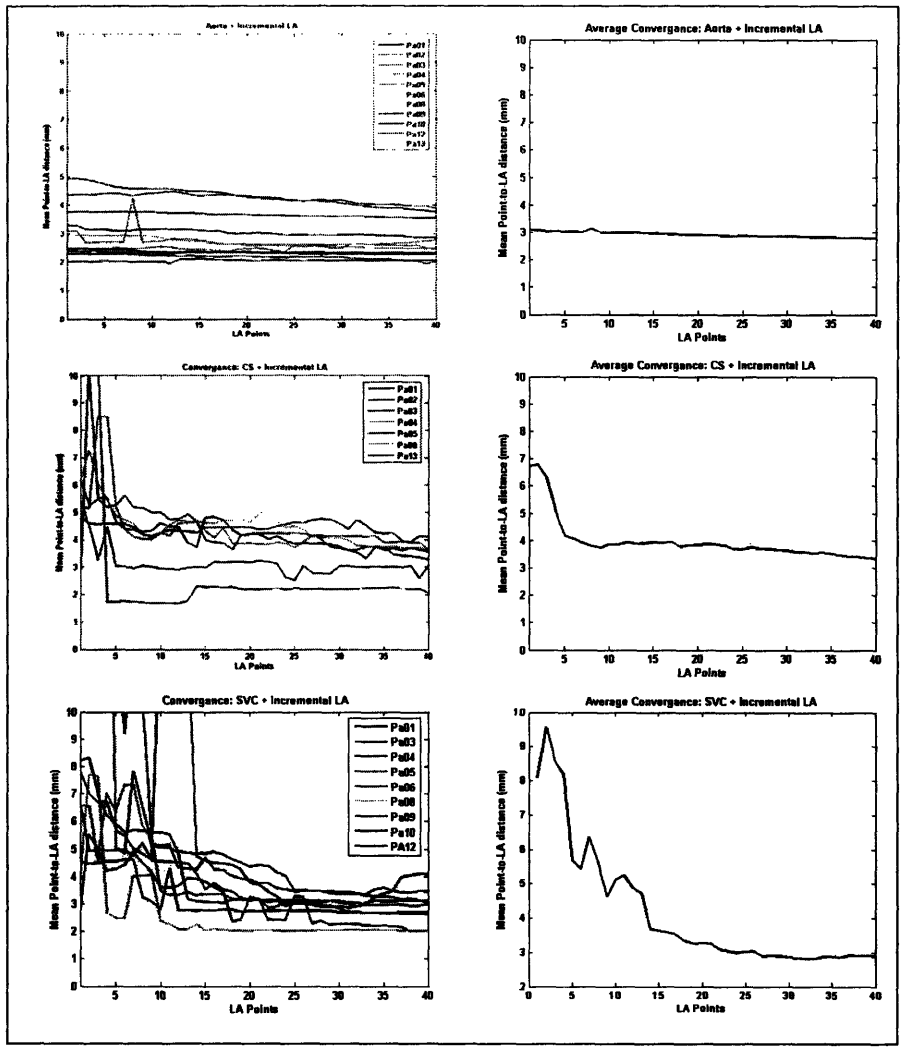

Figure 3-9: Registration convergance of LA using the great cardiac vessels.

In comparison, reigstration strategies which initially used the CS or SVC alone were likely to fall into a local minimum (3-9). Examples of these erroneous registrations are shown in Figure 3-8B. The addition of points within the left atrium did eventually improve the registration; however 15-20 points were needed to converge to a better solution. Therefore, the use of the aorta as an internal fiducial structure during registration provided the most rapid and accurate solution for aligning the imaging information with catheter-mapping data.

Prospective Evaluation of Aortic Registration

In the third phase of this study, a prospective evaluation of the utility of the aorta as an

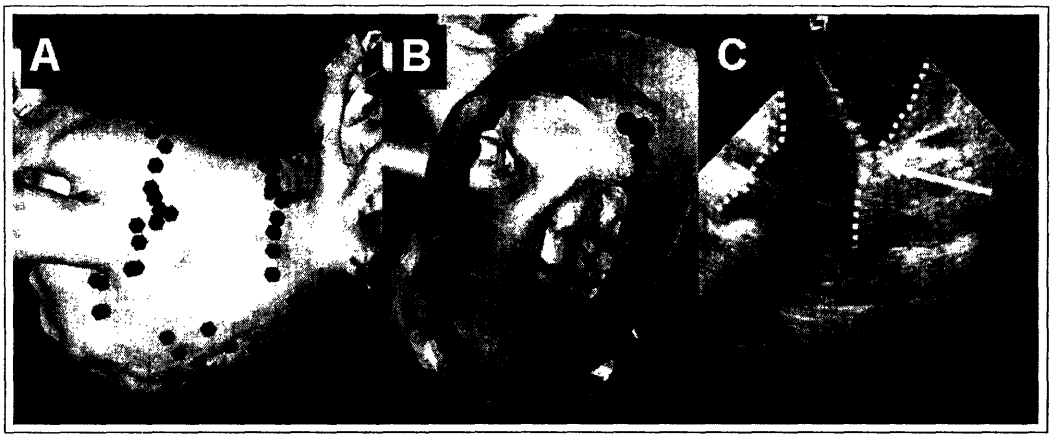

Figure 3-10: EAM + Pre-operative image registration. Pulmonary vein isolation is performed under image guidance using pre-operative image. (A) Posterior-anterior view of catheter during ablation on right side of left atrium. (B) Endo-lumenal veiw of right half of left atrium showing same catheter position as (A). Accuracy of image registered is verified by intracardiac ultrasound; the yellow dashed lines outline the right-sided pulmonary veins. Note the contact of the catheter with the left atrial wall.

internal fiducial structure to aid in rapid registration of the left atrium was performed. A series of consecutive patients (n=25) undergoing catheter ablation of atrial fibrillation were pre-operatively imaged use MR angiography. Segmentation and reconstruction were performed prior to the catheter ablation procedure. After gaining arterial and venous access during the subsequent electrophysiology procedure, catheter mapping (described above) was performed first within the aorta. On average mapping of the aorta took 5 minutes to complete.

The Myo software system was then used to register the pre-operative imaging data with this real-time catheter mapping information. Following the aortic registration, the catheter was manipulated into all 4 pulmonary veins using the Myo software which showed the real-time mapping catheter position within the patient-specific anatomy (Figure 3-10). During these manipulations neither fluoroscopy nor intracardiac echocardiography was used to assist in catheter manipulation. In the second step of the registration process, additional information acquired within the left atrium was used to further refine the alignment; however, this additional information only provided a minor improvement in the overal registration.

During this prospective evaluation, the accuracy of registration was confirmed use available imaging technology including fluoroscopy, contrast-enhanced fluoroscopy, and intracardiac echocardiography. In addition, to assess the accuracy of Aorta registration alone

in comparison to the final solution incorporating both the Aorta as well as the complete LA EAM points, the centroid movement in this alignment was quantified (n=24 cases). In comprison to registration using the Aorta along, there was an average shift of 0.2±1.0 mm horizontally (to the patients' right; ranges -2.3 to 2.8 mm), 0.1±1.4 mm inferiorly (range -2.1 to 3.3 mm), and 0.1±0.9mm anteriorly (range -1.6 to 3.1 mm).

3.4.2 Left Ventricular Registration Strategies

For ablation procedures of scar-related ventricular tachycardia, we investigated strategies for the rapid and accurate registration of the left ventricle. For this study, two strategies were evaluated using an *in vitro* left ventricular / aorta phantom and *in vivo* using a porcine model of healed myocardial infarction and a normal model with putative sites for ablation [51].

Phantom Experiments

In this portion of the study, a human-scale phantom of the left ventricle and aorta was filled with a diluted solution of gadolinium-DPTA. MR imaging was then performed on the contrast-filled phantom. These images were then segmented, and a endo-lumenal surface model was created from the 3D imaging data set. Electroanatomical mapping of the aorta and left ventricle was then performed in the phantom using a retrograde aortic approach. Using the three separate acquisitions, a series of simulation experiments were retrospectively performed to combine the pre-operative imaging information with the catheter-based mapping information (Figure 3-11).

***In Vivo* Experiments**

In this portion of the study, left ventricular registration strategies were evaluated in two phases. In the first phase, normal animals underwent an iron oxide injection procedure to place targets for catheter ablation under image guidance (Figure 3-13). Following the injections, MR imaging was performed to define chamber geometry and location of the injection sites. During a subsequent electrophysiology study, registration between the pre-operative MR imaging data and electroanatomical mapping information was performed, and RF ablation lesions were placed as close as possible via image guidance from the combined electroanatomical and imaging data.

Injections were perfomed using an 8 French mapping catheter with a 27-gauge, retractable needle which protrudes from the tip of the catheter (Noga-Star, Biosense-Webster,

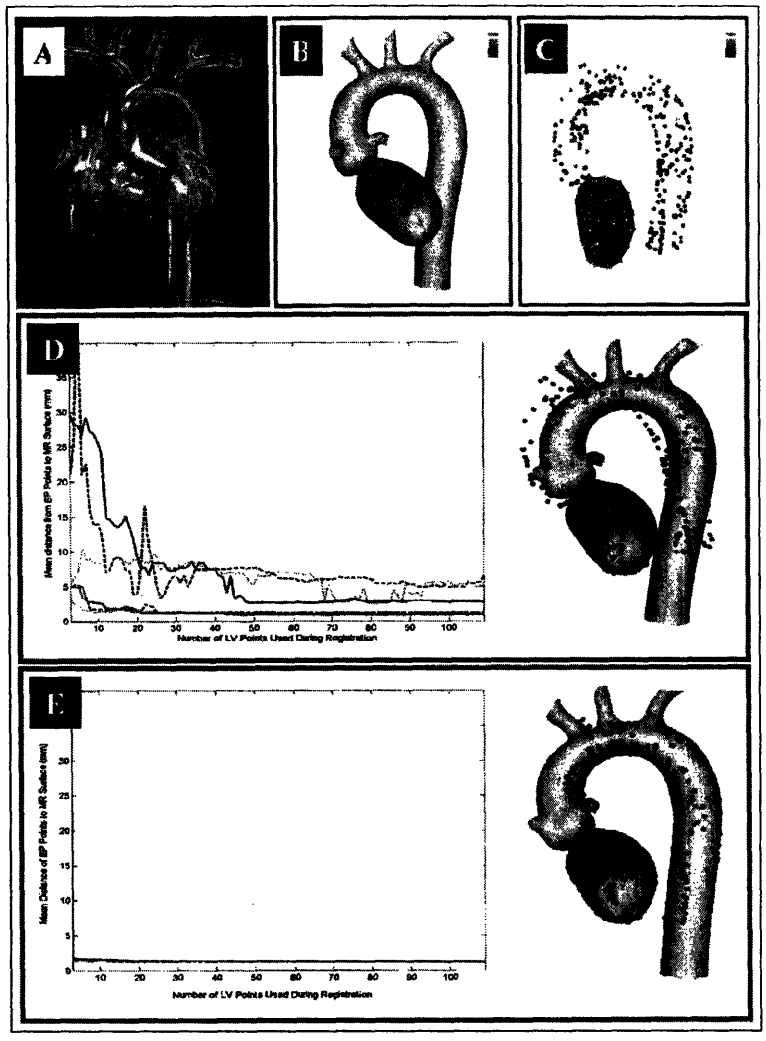

Figure 3-11: In vitro left ventricular (LV) phantom experiments. After filling a hollow plastic model of the heart (A) with a dilute solution of gadolinium, magnetic resonance imaging (MRI) scans were performed. The aorta and LV were manually segmented to generate a three-dimensional (3D) surface reconstruction (B). (C) After electroanatomic mapping of this phantom, the locations of the endoluminal aortic (blue points) and endocavitary LV (white points) points were registered with the 3D MRI. Strategies to register these MRI and magnetic electroanatomical mapping (MEAM) datasets were then evaluated. (D) Image registration was based solely upon registration of the MEAM LV points with the MRI-based LV surface. After a coordinate transformation, each MEAM LV point was sequentially incorporated into the registration process (horizontal axis). The level of accuracy of the registration process (vertical axis) was defined as the mean distance of either: 1) the complete MEAM LV point dataset to the MRI-based LV surface (red lines), or 2) the complete MEAM aorta point dataset to the MRI-based aorta surface (blue lines). Five simulations were performed with each of three separate dataset acquisitions; each line represents an average of each set of five simulations. This reveals that the MEAM LV point to MRI surface distance (red lines) can be minimized to 1 mm error, after only 30 points. However, the high level of inaccuracy in the MEAM aorta point to MRI surface distance (blue lines) demonstrates that the registration was simply a local minimal solution. Videlicet, in the registered image (right), the LV points appear to be well-aligned, but the misalignment of the aorta points indicates that this is an inaccurate solutionapparently as a result of rotation about the LV long axis. (E) Image integration was based upon first registering all of the MEAM aorta points with the MRI surface, followed by sequential incorporation of each MEAM LV point into the registrations process (horizontal axis). The level of accuracy of the registration process (vertical axis) was again defined by the mean distance of the complete MEAM LV point dataset to the MRI-based LV surface (red lines). The results show that after first registering the aorta, the MEAM LV point to MRI surface distance (red lines) can be minimized to 1 mm error after incorporating the first three LV points into the registration process.

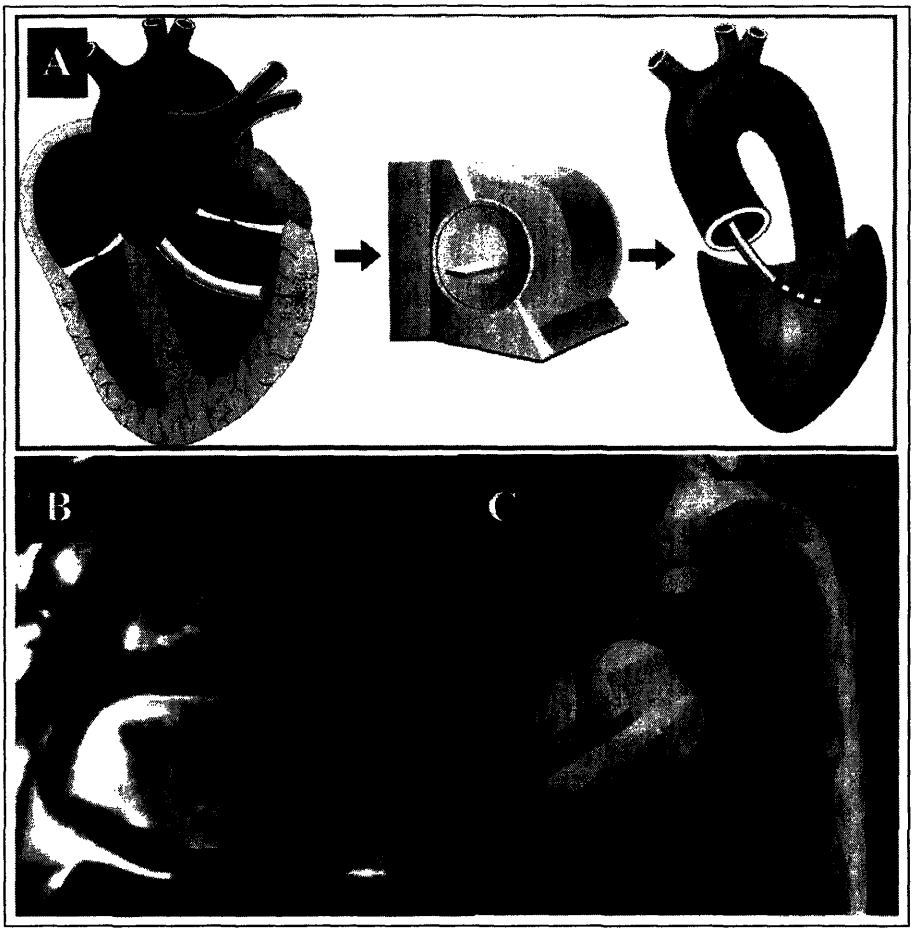

Figure 3-12: In vivo iron oxide injection experiments. (A) As shown in this procedure flow map, a solution of iron oxide particles and tissue dye (either methylene blue or India ink) was injected into the myocardium of normal animals at two to three discrete LV locations (left). Because the iron oxide particles are visible to MRI (middle), these injections served as "targets" (shown by an arrow in B) to test the registration strategy. The animals underwent MRI, and manual segmentation was performed to delineate the endoluminal surface of the aorta, the endocardial border of the LV, and the locations of the iron oxide injections (shown in C; each group of three blue dots represents an injection site). During the subsequent electroanatomic mapping procedure, these 3D datasets were registered with the MEAM system. Because the iron oxide injections do not leave any electrophysiologic signature, the locations of the ablation lesions were entirely based upon the registered MR images.

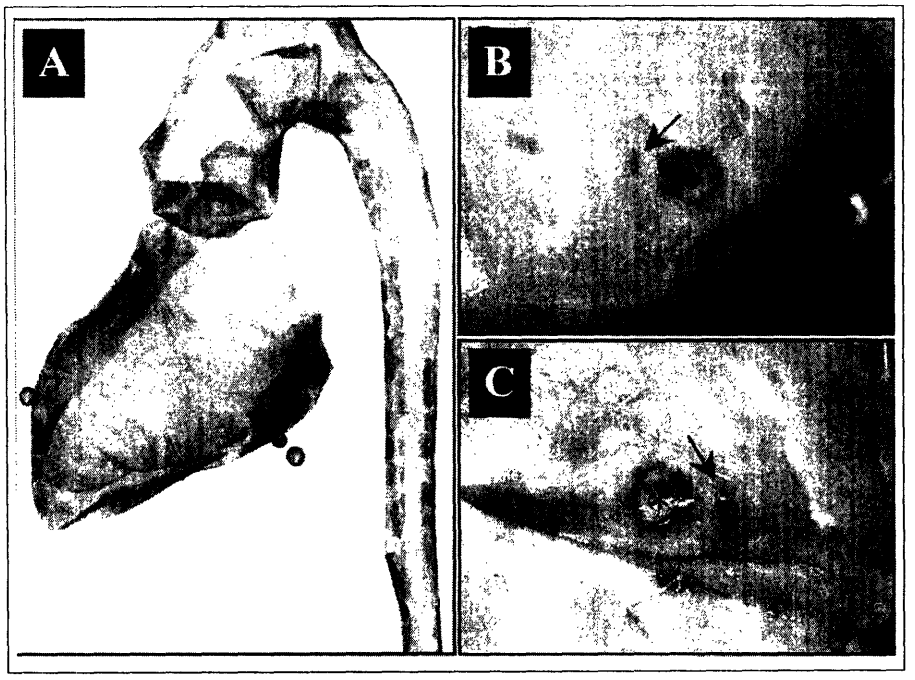

Figure 3-13: Accuracy of image integration based upon the iron oxide injection experiments. (A) As described in the legend of Figure 2, the register magnetic resonance imaging was used to guide movement of the catheter tip (green icon) to the iron oxide injection targets (yellow dot). (B and C) After catheter ablation at this point, the animal was killed and distance from the ablation lesion (blue asterisk) to the injection (arrow) noted.

Inc). The injection catheter was advanced into the left ventricle in a retrograd-aortic approach, and the needle was then extended 4 to 6 mm into the myocardium. An injection of 0.2 ml of iron oxide particles (0.4 mg/ml Feridex; Advanced Magnetics, Inc.) were injected at each site. The sites were chosen to be at least 20 mm apart from each other. In addition, injections were not placed at the apex of the left ventricle because relatively reproducibility of this location during catheter manipulation. To facilitate gross pathological review following image-guided ablations, either methylene blue or India ink was mixed with the iron oxide solution for use as a visual indicator.

In the second phase of the *in vivo* experiments, a porcine model of healed myocardial infarction underwent MR imaging to define the chamber geometry as well as the location and extent of scarred myocardial tissue (Figure 3-14).

The location and extend of the infarcted myocardial tissue was determined by two-dimensional myocardial delayed-enhancement (TR/TE/θ = 5.7ms/1.5ms/20°) 15- to 25-minutes status-post gadolinium-diethylene triamine pentacetic acid (gadolinium-DPTA) in-

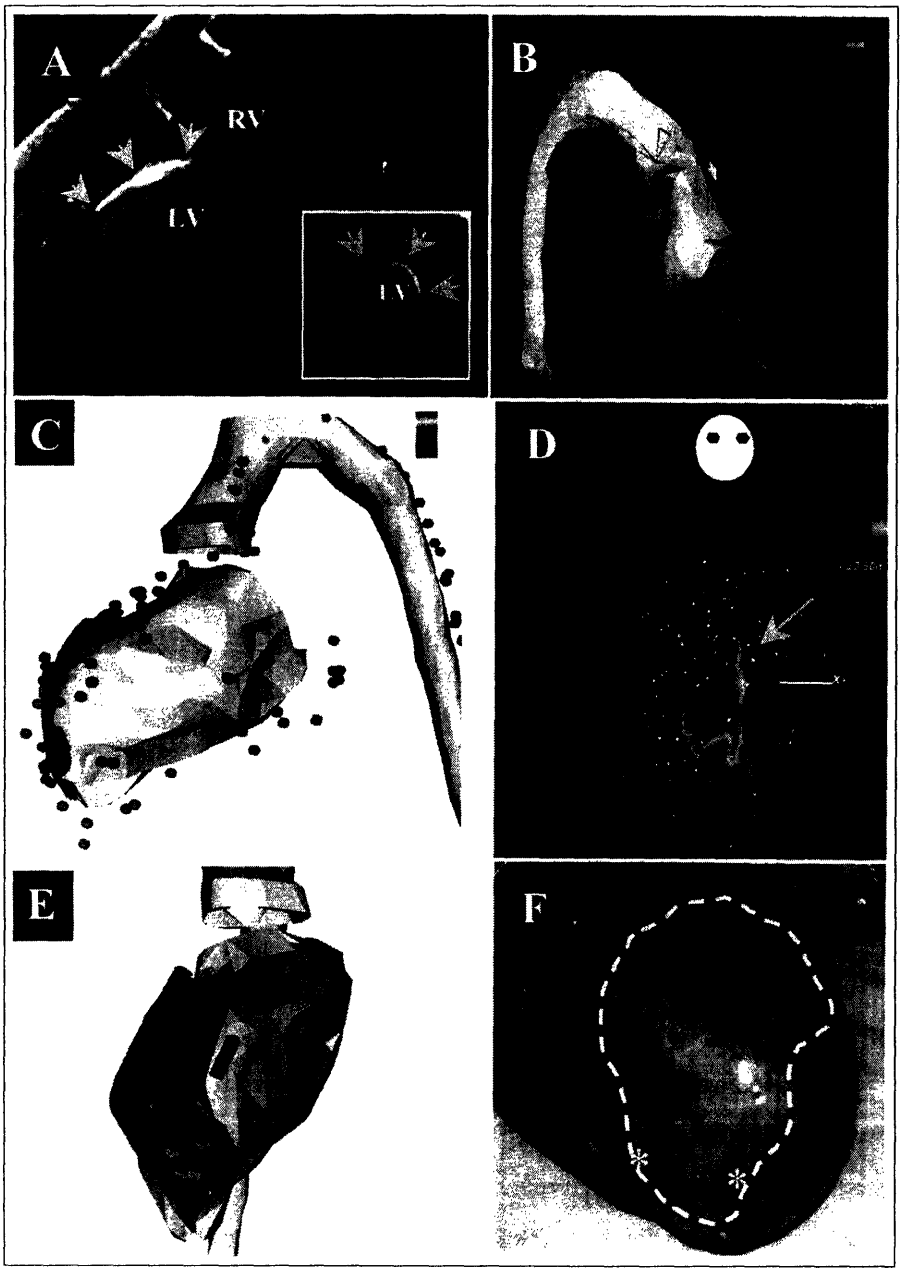

Figure 3-14: MRI-guided catheter navigation in vivo to the myocardial infarct borders. (A) The porcine infarct models underwent MRI 4 months after the anterior wall infarction procedure. The gadolinium-enhanced scarred myocardium (yellow arrows) is shown in these long- and short-axis (inset) delayed enhancement magnetic resonance images. (B) The aorta, LV endocardium, and myocardial scars were manually segmented and compiled into 3D datasets. During MEAM, the chamber geometries were constructed without displaying the corresponding electrophysiologic information. Radiofrequency ablation lesions were subsequently targeted to the borders of the scar solely on the basis of the registered MR image. Shown are the re-compiled surface reconstructions of the segmented LV, aorta, and scarred myocardium (in brown). (C) The registered 3D MRI of the porcine infarct model is shown: orange dots LV points; blue dots aorta points. (D) The electroanatomic bipolar voltage map depicts the anterior wall myocardial infarct; the color range was set such that the purple color represents normal tissue (i.e., 1.5 mV). The ablation lesions are shown as red dots; the yellow arrow denotes the ablation corresponding to the catheter position shown as a green icon in (E). (F) The corresponding ablation lesion (blue asterisk) was noted upon gross pathologic examination to be situated at the scar border; two other ablation lesions placed near the LV apex (yellow asterisk) were also appropriately localized to the scar borders. Abbreviations as in Figure.

	Injection Target	Expected Distance (mm)	Measured Distance (mm)	Residual Error (mm)
Animal #1	#1	4.3	1	3.3
	#2	1.2	1	0.2
Animal #2	#1	3.1	2	1.1
	#2	4.6	3	1.6
	#3	5.4	3	2.4
Animal #3	#1	3.9	4	0.1
	#2	6.9	3.5	3.4
Animal #4	#1	3.7	6	2.3
	#2	1.1	4	2.9
Animal #5	#1	7.5	5	2.5
	#2	5.1	4	1.1
	#3	1.6	1	0.6
Mean $\pm$ StdDev				1.8 ± 0.5

Table 3.2: Registration accuracy based up iron oxide injection experiments.

travenous infusione [60, 61, 62]. The post-QRS gating was timed to coincide as closely as possible with late diastole which matches the phase of the cardiac cycle during which EAM points are acquired. MR imaging of the porcine model of healed myocardial infarction was performed 119 ± 12 days (range: 102 to 133 days) after the infarction procedure.

Following image acqusisition, the MR images were segmented for the aorta, left ventricular endocardial surface, and the scarred myocardium within the left ventricle. Three-dimensional surface reconstructions were then created of these structures. The animals subsequently underwent catheter-based electroanatomical mapping. During this procedure, the electroanatomical mapping information displayed only ventricular geometry without additional electrogram annotation at each point. After acquiring the aorta and points within the left ventricle, reigstration of the pre-operative imaging and catheter mapping information was performed using the mICP algorithm described above.

Using the image integration, the catheter was then manipulated to the borders of the scarred myocardium, and a series of RF ablation lesions were created. At the conclusion of each electroanatomical mapping and ablation procedure, the animals were sacrificed, and the heart was immediately explanted for gross pathological examination (Figure 3-14E,F). For this series of experiments, the proximimity of the ablation lesion to the border of the scarred myocardium was determined, and it was compared to the locations recorded on the electroanatomical mapping system (Figure 3-14).

Results and Conclusions

During both the injection experiments and the delayed-enhancement scar-imaging studies, there was a consistent difference in left ventricular volume between the pre-operative imaging data and the real-time catheter mapping data. As discussed above, there are several physiological variables which could contribute to these differences including cardiac rate, cardiac rhythm, and fluid status during the long, anesthesized procedures. Despite these errors, these studies have demonstrated that the registration process can still have clinical utility. Based on the pre-operative MR imaging information, the electrophysiologist was able to: 1) manipulate and ablate within approximately 2 mm of iron oxide targets identified only by the imaging 2) ablate at the border of the scarred myocardial tissue based on delayed-enhancement imaging and 3) manipuate the catheter to anatomical structures such as the mitral valve, which has a unique electrical characteristic of both a atrial and ventricular activity on the electrogram recording. These results are particularly meaningful because the catheter manipuation and therapy was based only on the imaging information presented by the registration software. In a clnical setting, the addition of electrical and timing information recording from the mapping catheter would further assist a electrophysiologist during targeting and application of therapy; this additional information is expected to increase the accuracy and utility of the image integration paradigm. These results have important clinical implications for the treatment of ventricular tachycardia.

There are several limitations of these studies which must be addressed prior to widespread use of image integration during left ventricular electrophysiology procedures. In this portion of the work, manual segmentation of the pre-operative imaging information was performed. This process is time consuming as well as being prone to intra- and inter-observer variability. While general methods for semi- and full-automated segmentation exist, these methods should be adapted to specifically address segmentation of left ventricular MR imaging to be most useful. Furthermore, the slice-thickness of the pre-operative MR imaging was relatively large, and this resulted in artifacts on the surface reconstructions. While more images could be acquired, this extends the already significant MR imaging time required. A balance between the time require for MR imaging and the fidelity of the data must be reached.

Finally, a major limitation of this study is the contraindication of MR imaging in patients with pre-existing pacemakers or ICDs. Patients with ventricular tachycardia are at

a signficant risk for sudden cardiac death, and patients are being treated with these devices at an increaing rate. Although technology is evolving and initially research studies have demonstrated safety, there are not devices or leads approved for cardiac MR imaging. In addition, legacy current pacing and defibrillation leads and devices will be a problem for several years following the implantation of MR-compatible devices. In the meantime, cardiac CT is an alternative imaging modality for this work; it provides high resolution chamber geometry; however, CT imaging cannot directly distinguish scarred myocardial tissue from healthy tissue. Therefore, secondary indicators such as wall-thinning at regions of transmural myocardial scarring must be used instead.

3.4.3 Epicardial Registration Strategies

To evaluate registration for use during epicardial catheter mapping and ablation, a series of clinical strategies were evaluated to assist in registration. First, a retrospective evaluation of a porcine model of normal and healed myocardial tissue is perfomed to evaluate registration strategies using combinations of the left ventricular endocardial surface, the epicardial surface of the heart, and the aorta. Based on these results, registration of the epicardial surface was performed using the aorta as an internal fiducial structure to assist in registration.

The epicardial portion of the heart has significant implications for patients with scar related ventricular tachycardias. Electroanatomical mapping systems are commonly used to identify important entrance and exit sites for a reentry arrhythmia and to dilineate the scarred portion of the ventricle based on bipolar electrogram voltage. Substrate based mapping and ablation are effective in eliminating these reentrant circuits. However this approach of endocardial substrate mapping and ablation in the precense of transmural scar tissue, hypertrophic cardiomyopathies, and Chaga's disease have often failed. In each of these pathogies, typical RF ablation lesions placed on the endocardial surface of the ventricle may not result in a transmural lesion; therefore, the a malignant reentry circuit will persist following the electrophysiology study.

Faced with these difficulties, Sosa and collegues pioneered the percutaneous, sub-xyphoid approach to the pericardial space, which allows catheter-based mapping and ablation of the epicardial surface of the heart. Using nearly identical mapping and entrainment methods, this approach can be used to interrupt reentrant circuits previously untreatable by standard

endocardial mapping and ablation.

Preclinical, retrospective registration strategy evaluation

This protocol was approved by the Massachusetts General Hospital Subcomittee of Rsearch Animal Care and was performed in accordance to institutional guidelines.

Porcine Infarct Generation

In this portion of the study, a porcine model of healed myocardial infarction was used to during image integration. Briefly, a closed-chest infarction procedure was performed in 25- to 35-kg pigs [63, 64]. After an overnight fast and premedication with 1.4 mg/kg Telazol, 1.1 mg/kg acetylpromazine, and 0.05 mg/kg IM atropine, the animals were intubated and ventilated with oxygen. General anesthesia was maintained with inhaled 1.5% to 2.5% isoflurane. Arterial access was obtained, and a JR4 guide catheter was placed in the left main coronary artery. A 2.5- to 3.5-mm PTCA balloon was advanced to the mid left anterior descending coronary artery (LAD), and the balloon was inflated to 4 atm. Twenty seconds after balloon inflation, 60 to 80 L dry volume of Contour 75 to 150 m emboli (Boston Scientific) diluted in 4 mL of sterile saline was injected through the central lumen of the PTCA catheter. Continuous ECG and hemodynamic monitoring was performed during the infarction and during recovery. After extubation, the animals were observed and monitored for 1 to 3 hours until able to ambulate without assistance. The pigs were housed in the animal facility for a minimum of 4 weeks before the follow-up imaging and electrophysiology studies.

MR Imaging Study

The animals were placed on the gantry for MRI in a similar position as during the EAM procedure to minimize distortions in the shape and curvature of the torso. These animals underwent MRI and EAM on the same day, whereas the porcine infarct models were imaged 2.4±3.7 days (range 0 to 9 days) before EAM. The animals were mechanically ventilated, and the images were acquired at end-expiration. All MR images were acquired in a 1.5-T GE CV/I scanner (GE Medical Systems Inc., Waukesha, Wisconsin) equipped with a surface cardiac array coil. A breath-held 3D contrastenhanced MR angiogram was used to image the descending aorta (repetition time [TR]/echo time [TE]/6.6 ms/2.4 ms/45deg, field of view [FOV] 28 28 cm, 192 256 matrix, 2.2 mm slice width (sw), 32 slices/scan, 1 number of excitations [NEX]; 0.44 cc/kg gadolinium). Short-axis and long-axis cardiac images were acquired with sequential, breath-held two-dimensional SHARK-FEISTA (GE Medical

Systems Inc.) (TR/TE/ 6.3 ms/1.9 ms/50deg, 8 to 12 views per segment, FOV 26 26 cm, 256 224 matrix, 4 to 5 mm sw, 1 to 2 NEX, 20 phases/R to R interval, electrocardiographic gating). The location and extent of the infarcted tissue in the six animals with healed MI was determined by two-dimensional myocardial delayed enhancement (TR/TE/theta 5.7 ms/1.5 ms/20, 12 to 16 views per segment, inversion time 90 to 170 ms, FOV 26 26 cm, 256 224 matrix, 4 to 5 mm sw, 2 to 3 NEX, acquired 15 to 25 min post injection of gadoliniumdiethylene triamine pentacetic acid) (810) and a modified two-dimensional double-inversion recovery fast spin echo (TR/TE 3 R to R interval [2,500 to 3,500 ms]/144 ms, echo train length 32, FOV 26 x 26 cm, 256 x 224 matrix, 4 to 5 mm sw, 1 to 2 NEX). The prescribed post-QRS delays were selected to coincide as best possible with late diastole in order to match the cardiac phase during EAM.

Pericardial Access

Catheter access to the pericardial space was obtained via nonsurgical transthoracic puncture approached [65, 66, 67, 68]. Briefly, a 17-gauge Tuohy needle (1.5-mm OD, 98.4-mm length) is advanced under fluoroscopic guidance from the subxyphoid region of the thorax. As the needle approaches the pericardial space, small amounts of iodinated contrast are injected to determine proximity to the pericardial sac. After the needle has punctured and crossed the pericardium, a guide wire is passed through the needle. The needle is subsequently withdrawn, and a standard short, hemostatic sheath and introducer is then advanced over the guide wire. A mapping catheter is then passed through the sheath and easily maneuvered within the pericarrdial space. Once the mapping catheter is introduced, the catheter can be manipulated around the epicardial portion of the ventricles as well as the atrium. However, the epicardial regions surrounding the atria are divided into the transverse sinus, the superieor sinus, and the oblique sinus (Figure 3-15).

Electroanatomical Mapping

In addition to the pericardial access, standard femoral and arterial access was also gained to permit endocardial mapping of the left ventricle via a retrograde aortic approach. Before entering the left ventricle, the aorta was mapping using the technique described above (Section 3.2.4).

Then, magnetic electroanatomical mapping (MEAM) of the aorta and left ventricular (LV) endocardium were performed using CARTO (Biosense-Webster, Inc.) which allows for 3D mapping using a low-intensity magnetic field to localize the mapping catheter in space.

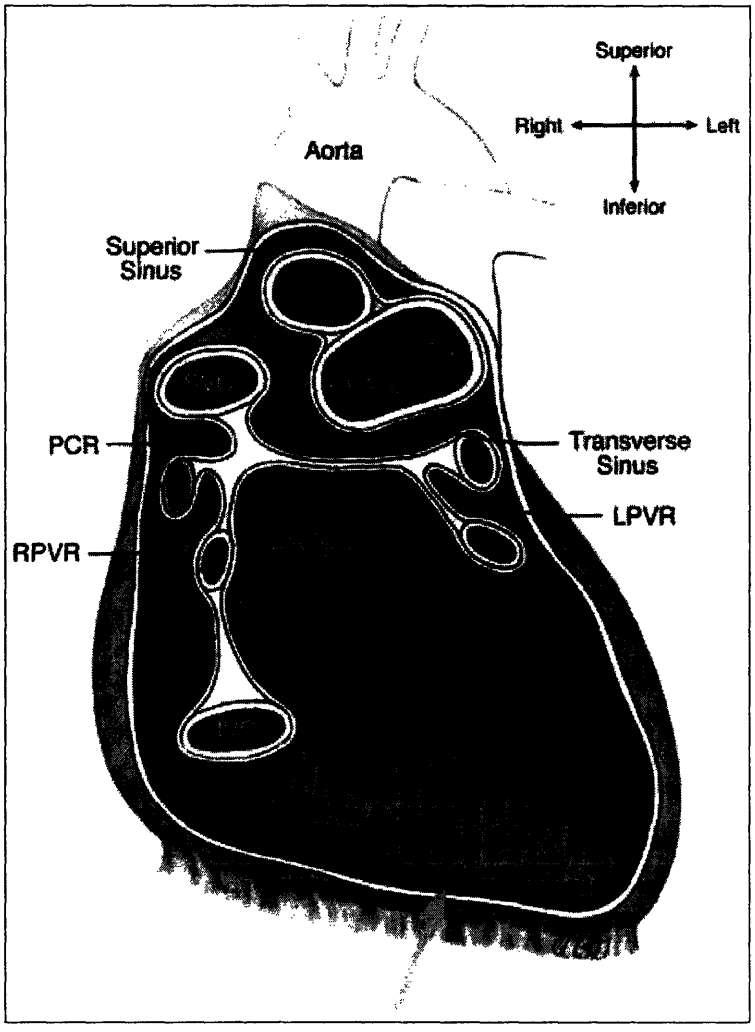

Figure 3-15: Epicardial catheterization. To access the pericardial space, a needle is advance from the subxyphoid region. The yellow arrow above represents the approximate location of access when the pericardium is crossed. (Figure adapted from [69].)

The LV endocardium was fully mapped during sinus rhythm to achieve a fill threshold of 15 mm. During pericardial mapping, the electroanatomical map was displayed as a solid geometric shell without any superimposed electrical information. Using the registered MRI dataset for catheter guidance (see below) radiofrequency ablation lesions were applied in a temperature-controlled mode limit of 55°C with up to 50 Watts for 30-60 seconds. During retrospective post-processing analyses, electroanatomical identification of the infarcted myocardium was delineated by bipolar voltage amplitude criteria; scar is defined as bipolar voltage amplitude $\leq$1.5 mV, and a color scale range of 0.5 mV to 1.5 mV was displayed.

Real-time Experiments

Before each real-time experiment, the MRI datasets were manually segmented using customized Matlab software (The MathWorks, Inc. Natick, MA). The Myo software was then used to receive the MEAM data and perform the registration algorithms and visualization. As described in Chapter 2, this software: i) displays and allows one to electronically manipulate the segmented MRI dataset, ii) re-creates the electroanatomical map based upon the transmitted spatial coordinates and electrogram information (including a simulation of the interpolations of the electrogram data performed by the MEAM system), iii) registers the two datasets based upon selected features of each dataset, and iv) allows real-time visualization of the catheter tip atop the real time MRI image. The epicardial and scar anatomy were used to guide catheter ablation in the pericardial space.

Registration

At the beginning of each in vivo procedure, contours from the segmented MR datasets were loaded into the registration software. Surfaces representing the left ventricular endocardium, ventricular epicardium and the myocardial scar, were generated for electronic display and manipulation. Points acquired in the aorta and left ventricular endocardium were used to register the MRI and MEAM datasets using the iterative closest points (ICP) algorithm. The real time catheter location is projected onto the endocardial, scar and epicardial MR images and used to guide the catheter in the pericardial space.

Gross Pathological examination

The animals were finally sacrificed and gross pathological examination was performed to determine whether the delivered lesion corresponds to the scar border.

Results and Conclusions

In the following sections, results from the real-time, *in vivo* experiments and from retrospec-

Strategy	Aorta Error (mm) Mean ± Std. Dev	Endo Error (mm) Mean ± Std. Dev	Epi Error (mm) Mean ± Std. Dev
Aorta	1.65 ± 1.27	7.71 ± 4.49	6.96 ± 4.33
20 Endo	9.95 ± 5.68	5.81 ± 3.95	7.06 ± 4.83
40 Endo	7.96 ± 4.56	4.34 ± 2.91	6.21 ± 4.27
20 Epi	10.99 ± 8.27	7.42 ± 4.68	5.75 ± 4.08
40 Epi	6.93 ± 4.23	5.07 ± 3.79	3.83 ± 3.61
Aorta + 20 Endo	1.51 ± 1.14	5.88 ± 3.40	6.00 ± 3.73
Aorta + 40 Endo	2.13 ± 1.40	5.18 ± 3.17	5.17 ± 3.50
Aorta + 20 Epi	2.11 ± 1.34	5.40 ± 3.64	5.61 ± 3.71
Aorta + 40 Epi	2.31 ± 1.49	5.03 ± 3.42	4.91 ± 3.70
20 Endo + 20 Epi	8.72 ± 6.21	4.67 ± 2.99	4.71 ± 3.60

Table 3.3: Evaluation of epicardial registration strategies.

tive simulations of registration strategies using the data from the *in vivo* experiments are discussed. The retrospective evaluation will be presented first to discuss plausible clinical registration schemes.

Retrospective Registration Simulations

Following the real-time experiments, the EAM data and pre-operative imaging data were used in a series of retrospective registration experiments to determine the optimal clinical strategy for registration and image-guidance on the epicardium of the heart.

Real-time Experiments

A total of 8 animals underwent an anterior infarction procedure. MR imaging was performed 88±38 days (range 42-133 days) after the infarction. The electroanatomical mapping and registration procedure was performed 4±3 days (range 1-9 days) after the MRI. During LV endocardial mapping, 114±25 points (range 74-155) were acquired during electroanatomical mapping. During ventricular epicardial mapping, 121±35 points (range 84-187) were acquired during electroanatomical mapping. Using the registered epicardial image, pericardial radiofrequency ablation lesions were targeted to the epicardial borders of the scar; a total of 2.9±1.7 lesions were delivered per animal (range 1-6). In two animals, only one lesion could be delivered in each since ventricular fibrillation occurred and the animals could not be resuscitated. Upon gross pathological examination, the ablation lesions were uniformly situated at the borders of the scar.

These experiments establish the proof-of-principle that pre-acquired cardiac MR images can be properly registered with intra-procedural electroanatomical mapping data to guide catheter ablation along epicardial borders of the scarred myocardium. This strategy of

Figure 3-16: After registration of the ventricle using LV endocardial and aortic points, mapping of the ventricular epicardium was guided by the registered image. In A and B, the segmented reconstructed MR images of the ventricular epicardium (in gray) and the scarred myocardium (in brown) are shown along with the real-time location of the mapping/ablation catheter tip (green-blue icon). The green points represent electroanatomical point locations acquired on the ventricular epicardium. The projections in B and C are AP and Left-Lateral, respectively. In the right anterior oblique view shown in C, the red dot represents an ablation lesion.

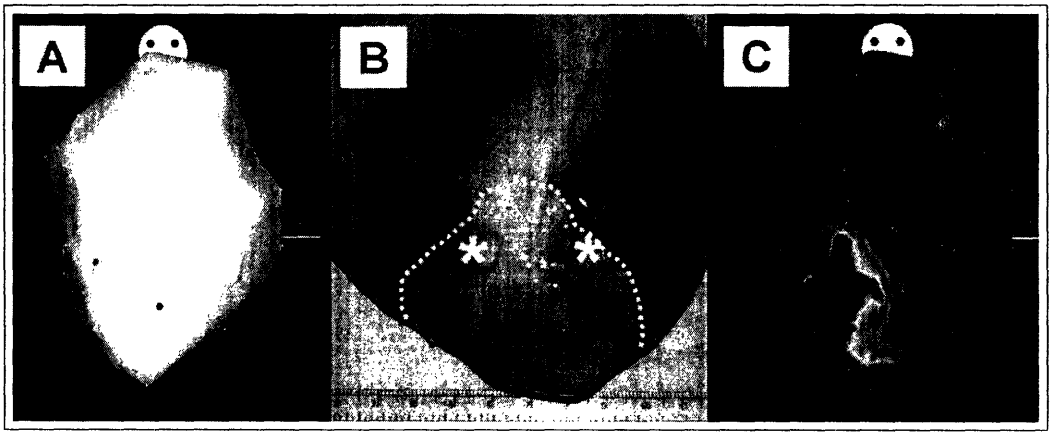

Figure 3-17: Epicardial ablation results. Using the registered ventricular epicardial construct, the ablation catheter was manipulated in the pericardial space to place lesions along the scar border. In A, the electroanatomical map is shown in an AP projection as a solid geometric shell without any annotated electrical information; the two red dots represent the locations of two ablation lesions delivered to the scar border (as defined by the registered MR image). In B, the ablation lesions (yellow asterisks) are indeed present at the scar border (dotted yellow line). In a C, the epicardial bipolar voltage amplitude map was displayed in a post-hoc fashion; the ablation lesions (red dots) were again situated at the scar border (as defined by a bipolar voltage amplitude of 1.5 mV.

image-guided therapy might demonstrate clinical utility in guiding catheter ablation of epicardial VT circuits.

3.5 Error Analysis

In the studies presented above to evaluate registration strategies for the left atrium, left ventricle, and epicardial surface of the heart, error following the registration process was assessed using the Euclidean distance between electroanatomical mapping points and the closest corresponding points on the surface model. Stastical properties including the minimum error, maximum error, mean error, and standard deviation of the error distributions were calculated. While phantom studies and pre-clinical experiments were specifically designed to assess the *accuracy* of registration, it is difficult to assess true accuracy in patients, where the "ground-truth" is not known. Fluoroscopy, electrograms recorded from the catheter tip, impedance measurements, and intracardiac ultrasound can be used in an attempt to assess accuracy; however, individually each of these methods has limitations including limited soft tissue contrast (fluroscopy), 2D imaging (ultrasound), and possible catheter deformation of the anatomy.

Therefore, the point-to-surface statistics are useful to assess error, but this information is an adjunct measure of accuracy. To assess the accuracy of registration between pre-operative MR or CT imaging data and intra-operative EAM data, a retrospective study was performed to evaluate convergance of the ICP and mICP registration algorithms. In the following study, an EAM point sets of both the Left Atrium and Aorta were generated for a series of patients (n=5). These "synthetic" point sets were chosen from points which defined the surface of the aorta or left atrium; therefore, it is possible for a resulting registration to have zero error as measure by point-to-surface distance. A known rotation was applied to the point set. Following the rotation, a registration was performed, and the transformation resulting from the registration was compared to the rotation initially applied to the "synthetic" EAM point. The process was repeated of a grid of rotations to assess the "capture range" of the ICP algorithm. The registration was performed in two ways: (1) only data from the left atrium was used for registration and (2) the aorta and left atrium data was used for the registration process.

Results and Conclusions

In the first series of registration convergance trials, the synthetic EAM data sets (80 points) were generated from patient-specific left atrium models (n=5) and registered using only the left atrium. Pertubations were then applied about the X-, Y-, and Z-axis ranging from -60 to 60 degrees in 4 degree steps in the X- and Y- axis and 15 degree steps for Z-axis rotations. After each perturbation, a registration between the EAM and imaging models was calculated, and the resulting transformation was comapred to the known perturbation (Figure 3-18).

In the second set of experiments, synthetic EAM point data of the (1) aorta and (2) left atrium (80 points in each data set for 160 points total) was generated from patient-specific imaging models (n=5). Again, a known rotational perturbation was applied (Rotation X: -60 to 60 degrees in 4 degree increments; Rotation Y: -60 to 60 degrees in 4 degree increments; Rotation Z: -60 to 60 in 30 degree increments), and a registration was subsequently calculated using the mICP algorithm. The error between the known perturbation and the resulting transformation following the registration calculation was then calculated (Figure 3-19).

The capture range of the ICP and mICP algorithms is limited even in the "no noise" experiments performed above. With the addition of the aorta using the mICP algorithm, there was a larger capture range during the registration process. While these experiments indicate that the aorta or another fiducial structure could be used to assist in registration of the left atrium, left ventricle, or epicardial surface, there are several limitations. First, 4,805 to 8,649 registrations were computed to estimate the convergance regions shown (Figures 3-18 and 3-19). This number of computations requires a significant amount of processing, and therefore, limits the availability and utility of this information during an electrophysiology procedure. In addition, the ground truth and perturbation are known, and therefore, we can asssess the accuracy of the resulting registration; however, this information is not avialable during *in vivo* interventions. Therefore, these results can be used a indication of robustness or precision of a registration, but they will not assess the actual accuracy of a registration.

To make these methods useable intra-operatively during an electrophysiology procedure, a pyramid scheme could be used in the following way. After registering the EAM data with the pre-operative imaing models, a thread would compute numerous perturbations about this registration – starting with small and increasingly larger rotation angles until the perturbations do not coverge back to the registration solution initially found. In this case,

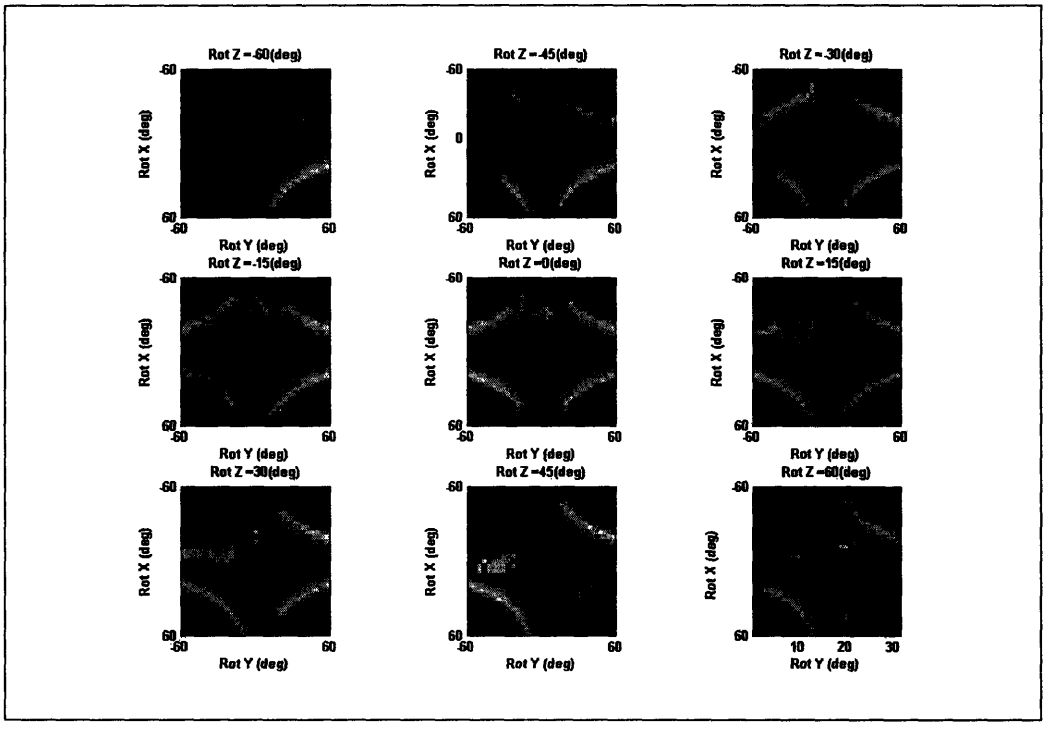

Figure 3-18: Registration convergance analysis using left atrium. Dark blue pixels represent small difference between the resulting registration and the applied perturbation of the data (ie an accurate registration), and dark red represents rotation error difference greater than 50 degrees. In this series of images, a grid evaluation of registration convergance was performed. A "synthetic" set of EAM points were generated from a patient-specific imaging model. These points were then perturbed by applying a known rotation about the X, Y, and Z axes. A registration was performed, and the resulting transformation was compared to the known rotation applied to the data. The results are shown above. Each image above represents a known rotation about the Z-axis. A pixel represents a single registration result, where the perturbation angle is given by the x-axis and y-axis for the Z-axis rotation indicated above each image. Notice the relatively small capture range of the ICP algorithm in this case with no-noise added to the synthetic EAM dataset.

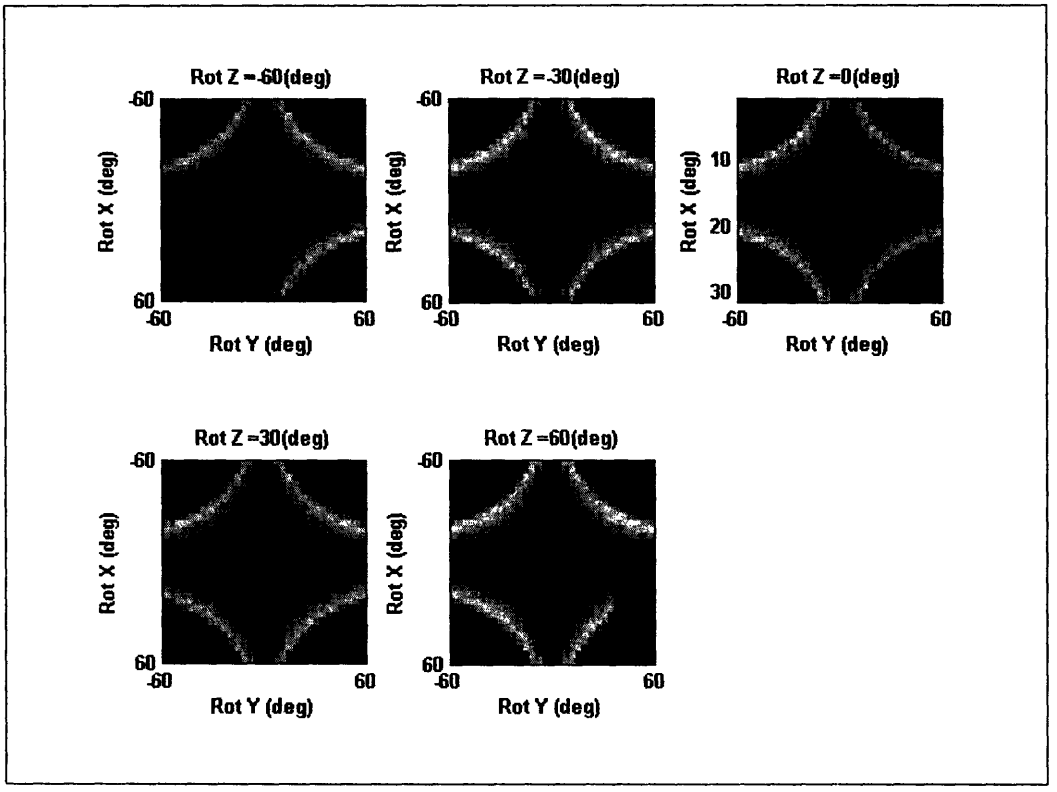

Figure 3-19: Registration convergance using left atrium and aorta. In this figure, as above, a known rotation was applied to a "synthetic" EAM point set, which was generated by sampling a patient-specific imaging model. Registration was then performed using the mICP algorithm describe above, where there are two classes assigned: aorta and left atrium. Note the broader regions of convergance even with large rotational pertubrations.

an extensive grid evaluation of convergance would not be available; however, the calculation would estimate the size of the minimum to which the ICP or mICP algorithm converged.

3.6 Chapter Summary and Conclusions

In this chapter, we have described the typical clinical workflow for image integration of pre-operative MR/CT imaging information with real-time catheter-based mapping data. These steps include: 1) image acquisition 2) segmentation 3)electroanatomical mapping 4) registration 5) error analysis and 6) visualization. Physiological variation between steps (such as image acquisition and electroanatomical mapping) of the clinical workflow can result in poor registrations or large residual errors betwen the two data types. The physiological variations include changes in heart rate, heart rhythm, respiratory effort.

Accurate registration of a highly-resolution pre-acquired 3D CT/MR image with real-time electroanatomical mapping can facilitate left atrial, left ventricular, and epicardial mapping and ablation, and has the added advantage of minimizing the amount of fluoroscopy exposure. However, these benefits are rendered irrelevant if the time required to achieve an accurate registration solution is prohibitively long. Indeed, the practical utility of image-guided therapy is highly dependent on achieving an accurate registration, but in a short amount of time. To this end, the major findings of this chapter include: 1) the curvature of vascular structures is highly-featured enough to accurately register chambers of the heart, 2) the curvature of the full Aorta is unique enough to rapidly and accurately register the LA-PVs, and 3) while potentially useful, registration using either the CS or SVC was less accurate than the Aorta and had a propensity to result in inaccurate local minima solutions

Registration using a vascular structure: It is important to recognize that the ICP registration algorithm employed in the custom system used in this study (as well as the system currently available for clinical use, CartoMerge, Biosense-Webster, Inc.) is a rigid body registration algorithm. This algorithm assumes that there is no deformation of any individual structure being mapped, nor distortion in the relationship between various structures. Accordingly, if a vascular structure outside the chamber of interest is in a fixed relationship with the heart, registration of one structure in theory should in effect register the 3D CT/MR image with the EAM system frame of reference.

The *in vitro* phantom experiments clearly demonstrated the power of incorporating a curved vascular structure, the arch-descending aorta, into the registration process. However, this in vitro model does not account for the various biological factors (including changes in respiration, volume, cardiac motion, and catheter-related anatomical deformation) that are present during in vivo mapping. Accordingly, the utility of registering a number of curved vascular structures was assessed in a detailed retrospective evaluation

In theory, any highly featured curved vascular structure should suffice to accurately register the LA-PVs, left ventricle, or epicardium. But in practice, only the Aorta provided a near-accurate solution without the need for acquiring additional EAM information within the LA-PVs; however, when using the aorta to register the left ventricle or epicardial surface of the heart, it appears that some additional information is necessary. One reason for this is likely related at least in part to the difference in mapping a relatively rigid arterial structure versus more distensible venous structures. It is easy to obtain a constellation of contact endovascular EAM points in the Aorta, but mapping the SVC and CS each have their own unique challenges. For example, mapping the CS from a femoral venous approach has a tendency to distend the vein. While not assessed in this study, it is possible that use of an internal jugular approach may attenuate this deformation. Similarly, the SVC is relatively easy to map, but it is a relatively straight structure that in itself does not provide enough unique information to achieve an accurate registration solution for the LA-PVs (unpublished data). The azygous and left brachiocephalic branches provide a unique shape, but entering these vessels using the standard mapping catheters (particularly the former) can cause a significant distortion in anatomy. It remains possible that more flexible specialized mapping catheters could be developed to overcome these limitations in SVC or CS mapping. But from a practical perspective, it is hard to imagine an economical solution save the use of a system like the magnetic navigation system recently developed for clinical use. Additional future work is required to assess whether the more flexible nature of this catheter might make it a more forgiving tool for accurate venous mapping.

Segmentation of the Aorta, Coronary Sinus and Superior Vena Cava: For any registration paradigm to be practical, it is important to be able to rapidly and accurately segment the relevant structures. To this end, the aorta is typically not a difficult structure to segment because: 1) it is relatively large and discretely located away from other contiguous structures by at least several millimeters, and 2) the timing of the contrast bolus to best

visualize the LA-PVs and LV is also able to visualize the aorta. Thus, the same CT or MR imaging scan can adequately visualize all the relevant structures (both the LA-PVs or LV and Aorta) even when the scan is of poor quality because of patient movement, breathing, etc. One important caveat to the image acquisition is that inspiration results in movements of both the LA-PVs or LV and the Aorta. As we have previously described: i) the heart moves inferiorly and anteriorly, ii) the ipsilateral PVs diverge, iii) the descending aorta doesn't move, iv) the arch of the aorta moves inferiorly, v) and the ascending aorta moves inferiorly and left-ward.

To mitigate against this potential source of error, it is important to recognize that intracardiac electroanatomical mapping is typically performed during quiet respiration and specifically at the end of 'quiet expiration' (the level of the functional residual volume). Thus, in order to properly employ the Aorta to register the LA-PVs, the CT or MR imaging should also be performed at this same respiratory state the level of the functional residual volume. In the authors' experience, this is easily achievable in virtually all patients with proper instruction during the imaging scan.

Unlike the Aorta, segmentation of the CS can be challenging because of its small size and proximity to the left atrium. Multi-detector CT scanning systems can largely overcome this issue; however, the scan cannot be of poor quality and the patient cannot be in atrial fibrillation. Furthermore, since the MR imaging protocol typically used to visualize the LA-PVs is not cardiac-gated and of somewhat lower spatial resolution, the CS cannot be adequately visualized in the same series of images. A separate MR pulse sequence can be used to visualize and then segment the CS (unpublished observation). However, 1) this increases the MRI scanning time, and 2) since the LA-PVs and CS are acquired in separately, there exists the possibility of mis-alignment of the LA-PVs with the CS MRI. This could happen, for example, if the phases of respiration of the breath-holds during image acquisitions for the LA-PVs and CS are different.

Similarly, preparation of the SVC and its azygous and brachiocephalic branches can be challenging. For CT imaging, the timing of the contrast bolus to visualize the LA-PVs is not necessary optimal for visualizing the branches of SVC; during the bolus infusion of contrast from the left arm, the SVC and brachiocephalic branches would be well seen, but the azygous branch would not be seen. Both the azygous and LA-PVs would contain adequate contrast with either a two-step contrast infusion protocol or a longer infusion

time so that either i) contrast is still infusing at the time of imaging, or ii) the contrast has completely passed though the circulation and all of the vascular structures can be visualized. Unfortunately, the latter typically results in a lower than preferable contrast-to-noise ratio and the CT acquisition must be of high quality (no movement or respiration during imaging) and cannot have any artifacts (e.g. pacing leads). For MR imaging, just like for the CS, separate pulse sequences are required to individually image the LA-PVs and the SVC with its branches; and the same limitations exist.

From a practical perspective, if either the CS or SVC were able to accurately and reliably register the LA-PVs with a level of accuracy comparable to use of the Aorta, the difficulties attendant with proper CS / SVC image acquisition and segmentation could be overcome. However, the image acquisition / segmentation difficulties are compounded by the lack of good registration with either of these structures alone. The post-hoc registration experiments in this study indicate that use of the CS or SVC for registration is dependent on acquiring a significant amount of mapping information from within the LA-PVs. And if this further LA-PVs EAM information is required (and may still result in a local minimal solution without a full LA-PVs EAM dataset), the utility of CS or SVC mapping to quickly register the CT/MR image is highly questionable.

Clinical Implications:

At the time this study was performed, there was no commercially-available software to integrate EAM and imaging information; accordingly, custom software was written to conduct this study. However, commercially-available software now exists to perform image integration for catheter ablation procedures (CartoMerge, Biosense-Webster, Inc.) and can be employed for any of the registration strategies described in this study.

It is important to recognize that the clinical utility of this image-guided therapy as described in this study is highly-dependent on the catheter ablation strategy employed by the operator. It would be most useful for an ablation strategy that relies heavily on the use of electroanatomical mapping to guide LA-PV catheter mapping and ablation. On the other hand, a PV isolation strategy that employs only the use of fluoroscopy, or the use of a combination of ICE and fluoroscopy would likely benefit little from CT/MR image integration. These ablation strategies would likely benefit more from the integration of CT/MR imaging with fluoroscopy itself.

But for electrophysiologists that employ electroanatomical mapping to guide the ab-

lation procedure, the Aorta can be used to rapidly register the LA-PVs. Of note, it is certainly true that the combination of the descending + arch of the aorta provided the optimal information for rapid registration, but accurate registration may also be achieved by mapping the descending aorta alone if this provides enough unique information. For example, the descending aorta may provide adequately unique information in patients with a 'sigmoid'-shaped aorta; alternatively, even in patients with a 'normal' aorta, accurate registration may be achieved by acquiring some EAM information from only the proximal (curved) region of the aortic arch, and not the full arch.

The location of the aorta between the two sets of pulmonary veins confers a unique advantage to the use of this structure for registering the LA-PVs. While small errors are certainly seen by use of the Aorta alone or even with the further incorporation of LA-PV EAM information, this error is less likely to result in a left-right translation error. This would be expected to make more unlikely the inadvertent placement of ablation lesions within the PVs resulting in PV stenosis.

Since the heart is relatively rapidly registered using the Aorta, it should be noted that this registration paradigm may also be used for aiding in the mapping and ablation of other chambers of the heart including catheter ablation of ventricular tachycardia, or catheter ablation of arrhythmias in patients with abnormal cardiac anatomy, such as in patients with congenital heart disease.

Limitations of Aorta Registration: One disadvantage of Aorta registration is that by necessity this requires a femoral arterial puncture using a 7 or 8Fr introducer sheath. This disadvantage is mitigated in part by the fact that retrograde aortic access does confer the ability to perform LA mapping using a different approach from simply transseptal mapping. This can allow the operator to place the ablation electrode against left atrial tissue using a different orientation and stability factors that can at times offer an advantage to the transseptal approach at certain LA locations (such as the mitral annulus).

In patients with severe atherosclerotic aortic disease, extensive catheter manipulation within the aorta is undesirable because of the risks of cerebral or peripheral embolization. Fortunately, such patients with extensive atherosclerotic aortic disease are less common in patients referred for AF ablation, and in any event, the pre-procedure CT or MRI scan can easily detect luminal irregularities; when a severely diseased Aorta is recognized in a particular patient, Aorta mapping can be foregone from the registration strategy.

This study did not evaluate the use of other structures to register the LA-PVs such as the right atrium or pulmonary artery. In preliminary work, the pulmonary artery was found to be a difficult structure to map; while easy to place a catheter within the vessel, it proved difficult to reliably collect luminal EAM points contacting the various walls of the vessel. And mapping the right atrium in order to register the left atrium was also not preferable from a workflow perspective. Similarly, this study did not assess the simultaneous use of multiple structures to register the LA-PVs.

While both CT and MR images are typically acquired in sinus rhythm, only the CT images are gated to the cardiac cycle. The inability to perform cardiac gating during MR angiography results in the MR images approximating the end-diastolic volume of the chamber that is, the largest size of the chamber. Since electroanatomical mapping was also performed gated to the QRS complex, the diastolic dimension of the atrium is again expected. Also, because the regions of the left atrium most relevant for performing a PV isolation procedure do not tend to have large movements during the cardiac cycle (that is, these regions are tethered to the body near the PVs), the phase of the cycle would not be expected to have an overly negative/dramatic impact on the quality of registration. However, additional studies are warranted to better understand the effects of cardiac gating and cardiac rhythm on image processing and registration.

Until the development of real-time imaging modalities such as 3-dimensional ultrasound imaging or real-time interventional MRI that may obviate the need for image integration, there is a need for the development of a clinically-relevant approach to rapidly and accurately register pre-acquired CT/MR images with real-time electroanatomical mapping to guide catheter ablation procedures. To this end, this study establishes that the curvature of the aorta allows it to serve as an internal fiducial structure capable of rapidly registering the 3D imaging with electroanatomical mapping even before entering the left atrium. The accuracy of this image integration can then be further refined by the incorporation of additional left atrial information into the registration process. How this translates into improvements in the safety, efficacy and speed of the catheter ablation procedure remains to be determined.

Chapter 4

Multivariate Scattered Data Interpolation for Model Warping

Following a registration of pre-operative MR or CT imaging data with intra-operative electroanatomical mapping information, there are many reasons for residual errors to exist. The reader is referred to Chapter 3 for an in-depth examination of error sources throughout the clinical workflow. In addition, it is not uncommon for a patient under conscious sedation to move from discomfort during the electroanatomical mapping and ablation procedure. This movement corrupts the electroanatomical mapping information as well as any registration which uses the now-corrupt information.

Whatever the underlying reason for residual error following registration, it is important to have methods which can compensate for these differences, and if possible, recover from patient movement. If an interpolation scheme is not used, the actual position of a catheter could easily be misinterpreted, possible resulting in the application of therapy to an undesired location within the heart.

In the following sections we will develop and compare methods to warp the pre-operative CT or MR image model to the intra-operative electroanatomical mapping data. The main focus will apply radial basis functions to perform the data interpolation. Following the development of these methods, we will evaluate the methods through retrospective analysis of clinical data.

Figure 4-1: Residual error following registration.Mean point error 1.922 mm. Std Dev. 1.61 Min: 0 Max: 8.3.

4.1 Motivation

Patient movement and physiological variations are two common causes for gross residual errors following registration between imaging and mapping information. The reader is referred to Chapter 3 for a discussion of the physiological variations and their effects on the registration process (Figure 4-1).

Besides physiological differences, patient movement is another significant cause of residual errors; however in this case the errors affect the accuracy of the electroanatomical mapping with which a registration is computed. In a typically situation, a patient under conscious sedation will move due to positional discomfort or pain associated with radio-frequency ablation application. The electroanatomical mapping system references points acquired within the heart to a reference patch adhered to the mid-back of a patient. Therefore, patient movement can alter the relationship of the heart to the reference patch through soft-tissue deformation of the skin or through changes within the thorax. These changes do not have to be significant ($\geq$3 mm), and often, the smaller changes are harder for the clinician to recognize and respond to appropriately.

At this time, there are only two options available to the clinician, and both options have significant limitations. The electrophysiologist can repeat the electroanatomical mapping process again. While this is the safest and most accurate way to understand changes

resulting from patient-movement, this process is extremely time consuming and labor intensive. In addition, there is no current method for identify ablation lesions placed before the patient movement; therefore, the physician must constantly interpolate the changes between the pre-movement and post-movement mapping data in his/her mind. The display of both pre-movement and post-movement electroanatomical maps can also be visual confusing from the large regions of overlap and difficulty in distinguishing the difference between the pre-movement and post-movement maps. A minimal improvement can be made by changing the representation of the pre-movement map to a point cloud representation without an interpolating 3D surface. The second option is to continue the electrophysiology procedure without remapping the cardiac chamber and repeating the registration process. In this option, the transformation resulting from the movement is poorly understood.

Ideally, the methods developed here would be able to compensate for these changes without the need for repeating the electroanatomical mapping system. In addition, methods to adapt electroanatomical mapping and ablation information acquired before patient movement would greatly enhance the clinical utility of the interpolation methods.

4.2 Methods

Given a set of zero-valued surface points (on a pre-operatively derived heart model) and a non-zero off-surface points of catheter based EAM points following registration, we are trying to solve the a scattered data interpolation problem. Multivariate interpolation of scattered data is a common problem encountered throughout science and engineering, and there are multiple methods available with individual advantages and limitations. Radial basis functions will be our predominant focus; however, we will briefly review other methods available for interpolation. The abstract problem description is similar to that of the registration process, and elastic transformations are commonly used in 2D and 3D domains for registration as well as for warping of atlas information for intersubject registration problems.

4.2.1 Warping Algorithms

Warping algorithms for 3D deformation of data are broadly classified into two types: 1) intensity-based algorithms and 2) feature-based algorithms. Model-based approaches constrain the warping algorithms through the use of control points, curves, surfaces, and other

corresponding geometric feature information extracted from both data sets. In contrast to model-based methods, intensity-based approaches match intensity patterns based on mathematical or statistical criteria [70].

4.2.2 Interpolation Problem Statement

In terms of our application, following rigid-body registration between pre-operative MR or CT imaging data and intra-operative catheter-mapping data, there will be residual errors from catheter deformation and physiological variations (Figure 4-1). To compensate for these residual errors, an interpolation is desired:
Given a set of distinct nodes $X = \{x_i\} \subset \mathbb{R}$ *and a set of desired function values* $\{f_i\}$ *we would like to find an interpolant* $s : \mathbb{R}^3 \rightarrow \mathbb{R}^3$ *such that*

$$s(x_i) = f_i, i = 1, \ldots, n \tag{4.1}$$

where $x_i = (x, y, z)$ *for points* $x \in \mathbb{R}^3$.

When warping the pre-operative imaging-derived surface models to the intra-operative electroanatomical mapping information, the set $X = \{x_i\}, i = 1, \ldots, n$ are the locations of the electroanatomical mapping points following registration to the pre-operative imaging model using the ICP or mICP algorithm (Chapter 3). Likewise, following the registration process, the set of $\{f_i\}, i = 1, \ldots, n$ points are the set of points lying on the surface model which are closest to the EAM points (Figure 4-1).

4.2.3 Radial Basis Function Interpolation

From the problem statement above, we will consider interpolants, s, which take the form of radial basis function expansions. In general, an RBF expansions take the two-part form:

$$s(x) = p_m(x) + \sum_{i=1}^{n} \lambda_i \phi(\|x - x_i\|) \tag{4.2}$$

where p_m is a low-degree polynomial or absent, $\|\cdot\|$ denotes the Euclidean norm on $\mathbb{R}^3$, and $\phi(r)$ for $r \geq 0$ is a fixed, real-valued, univariate function known as the *basic function* [71]. The *basic function* is usually unboudned and of global (non-compact) support.

The interpolation or approximation is a combination of radial basis functions centered

around the landmark points x_i. If the polynomial in Equation (4.2) is of degree m, then additional constraint on the coefficents are

$$\sum_{i=1}^{n} \lambda_i q(x_i) = 0, \text{for all polynomials } q \text{ of degree at most } m \tag{4.3}$$

This constraint along with the interpolation statement in Equation (4.1) lead to a system of linear equations for the coefficents which specify the RBF:

$$\begin{bmatrix} \mathbf{A} & \mathbf{P} \\ \mathbf{P}^T & \mathbf{0}_{4\times4} \end{bmatrix} \begin{bmatrix} \lambda \\ \mathbf{c} \end{bmatrix} = \begin{bmatrix} \mathbf{f} \\ \mathbf{0}_{4\times3} \end{bmatrix} \tag{4.4}$$

where the submatrices $\mathbf{P}$,$\mathbf{A}$, $\mathbf{f}$, λ, and $\mathbf{c}$ are:

$$\mathbf{A} = (a_{ij}) = (\phi(\|x_i - x_j\|)) \tag{4.5}$$

$$\mathbf{P} = \begin{bmatrix} 1 & x_1 & y_1 & z_1 \\ 1 & x_2 & y_2 & z_2 \\ \vdots & \vdots & \vdots & \vdots \\ 1 & x_n & y_n & z_n \end{bmatrix} \qquad \mathbf{f} = \begin{bmatrix} f_1 \\ f_2 \\ \vdots \\ f_n \end{bmatrix} \tag{4.6}$$

$$\lambda = (\lambda_1, \lambda_2, \ldots, \lambda_n)^T \tag{4.7}$$

$$\mathbf{c} = (c_0, c_1, c_2, c_3)^T \tag{4.8}$$

$$p_1(x) = c_0 + c_1 x + c_2 y + c_3 z \tag{4.9}$$

Solving this linear system determines the λ and c, and hense, the interpolator $s(x)$.

Properties of radial basis functions

Perhaps the most widely-known and researched RBF is the 2D and 3D thin-plate spline, given by:

$$\phi(r) = U(r) = r^2 \log r^2 \tag{4.10}$$

This function $U(r)$ satisfies the equation:

$$\Delta^2 U = \left(\frac{\partial^2}{\partial x^2} + \frac{\partial^2}{\partial y^2} \right)^2 U \tag{4.11}$$

Therefore, $U(r)$ is a *fundamental solution* of the biharmonic equation: $\Delta^2 U = 0$ [72]. The function control points minimize the energy functional given by:

$$E(f) = \int\int\int \left[\frac{\partial^2 f}{\partial x^2} + \frac{\partial^2 f}{\partial y^2} + \frac{\partial^2 f}{\partial z^2} + 2\left(\frac{\partial^2 f}{\partial x \partial y}\right) + 2\left(\frac{\partial^2 f}{\partial x \partial z}\right) + 2\left(\frac{\partial^2 f}{\partial y \partial z}\right) \right] dxdydz \tag{4.12}$$

The choice of the radial basis function $\phi(r)$ determines important characteristics of the resulting interpolation. Three important characteristics are [73]:

- **Locality.** The definition of locality here is referring to the global extent to which a radial basis function centered at one interpolation position influences other radial basis functions. Depending on the RBF choice, each landmark pair used for the approximation effects the entire transformed space. Other RBFs allow for parameter variation to limit the effects to a region surrounding the landmark pair.

- **Solvability.** In order to solve the linear system of equations defined in Equation (4.4), the left-hand terms must be invertible or non-singular. Therefore, for thin-plate spline interpolation, the landmarks must not be coplanar. However, the Gaussian and multiquadric RBFs place no restrictions. In particular, the evaluation of RBFs does not require the data to lie on a regular grid. A discussion of solvability and the choice of RBF and singularity conditions is below.

- **Efficiency.** The computational efficiency of the interpolation scheme depends on both the radial basis function choice as well as the number of landmark pairs. While the ever increasing computational speed of computers may reduce concern regarding computational efficiency, there are two important factors to consider. First, variation of the constant parameters in the radial basis functions below require recalculation of the solution to the linear system in Equation (4.4). Second, the warping algorithms are being used in a multi-threaded, real-time system during cardiac electrophysiology procedures; therefore, these methods must be extremely fast (on the order of 10-15

seconds).

Common radial basis functions

There are several commonly used radial basis functions. These are linear, thin-plate splines, Gaussian, multiquadric, and inverse multiquadrics [74, 75, 73, 71].

$$\begin{aligned}
&\phi(r) = r && \text{(linear)} \\
&\phi(r) = r^2\log(r), r^2\log(r^2) && \text{(thin-plate spline)} \\
&\phi(r) = r^3 && \text{(triharmonic)} \\
&\phi(r) = e^{-\alpha r^2}, (\alpha > 0) && \text{(Gaussian)} \\
&\phi(r) = \sqrt{r^2 + c^2}, (c > 0) && \text{(multiquadric)} \\
&\phi(r) = \frac{1}{1+(cr)^2} && \text{(inverse quadric)}
\end{aligned} \tag{4.13}$$

Compactly supported radial basis functions

One limitation of the radial basis functions listed above is the global support or influence of all landmark pairs on the warping. Radial basis functions with compact support are an attractive alternative. The Wendland functions (sometimes known as the ψ-functions of Wendland) are a set of univariate, piecewise polynomials. The general form of these functions is given by:

$$\psi(r) = \begin{cases} p(r) & 0 \leq r \leq 1 \\ 0 & r > 1 \end{cases} \tag{4.14}$$

Therefore, outside some range of r the function will be identically zero. The resulting linear system in Equation (4.4) will then have sparse matrices, and well-known methods can be exploited in the evaluation of the equation.

4.3 Results and Discussion

Using the radial basis functions explained above, a series of simulations and retrospective evaluations was performed on patient data from catheter-based pulmonary veins isolation procedures conducted under image-guidance using the Myo software system. For the following evaluations, registration between EAM and imaging data was performed for a series of 10 patients. Following the registration using a combination of the entire aorta and left atrial points, point-to-surface distance was calculated for the left atrium points as well as separately for the ablation point set (Table 4.1). The pre-operative imaging model was

Patient ID	LA Error (mm) Mean (±Std.Dev.)	Abl. Error (mm) Mean (±Std.Dev.)
Patient #1	1.59 (±1.59)	2.74 (±1.90
Patient #2	1.56 (±1.04)	2.50 (±1.55)
Patient #3	2.16 (±1.67)	2.55 (±2.14)
Patient #4	1.70 (±1.39)	2.05 (±1.40)
Patient #5	1.35 (±1.37)	2.16 (±1.50)
Patient #6	2.42 (±1.99)	4.46 (±2.82)
Patient #7	1.41 (±1.18)	1.33 (±1.09)
Patient #8	1.68 (±1.25)	2.24 (±2.17)
Patient #9	1.84 (±1.79)	2.82 (±2.03)
Patient #10	1.36 (±1.11)	1.88 (±1.61)
Mean:	**1.69**	**2.47**

Table 4.1: Registration error using aorta + left atrium prior to warping.

then warped to compensate for the residual errors following the registration process. The points used during the calculation were only points within the left atrium and one fifth of the ablation point set. The entire point set could be used; however, in this case there would be no error, as the radial basis functions would interpolate all points. The warping was repeated for multiple radial basis functions. After each new transformation was applied to the imaging model, the point-to-surface error was recalculated for the ablation point set.

Registration was performed using the aorta and left atrium in 10 patients. The resulting point-to-surface errors were then calculated for both the left atrial points and the ablation point set (Table 4.1). Two radial basis functions were then used to deform the surface to compensate for the residual errors following the registration process. In the first set of simulations, a linear radial basis function was used (Table 4.2). The second set a warping was performed using a thin-plate spline radial basis function (Table 4.3). In both cases, these radial basis functions have global support; therefore, the resulting warp transformations result in deformations of the entire surface model.

4.4 Summary and Conclusions

Residual errors following the registration of pre-operative CT or MR imaging data with real-time catheter mapping information can be visually confusing to an electrophysiologist using image-guidance during a catheter intervention. There are many causes for these residual errors including catheter deformation of a cardiac chamber, patient movement, physi-

Patient ID	Baseline Error (mm) Mean (±Std.Dev.)	Post-Warp Mean (±Std.Dev.)
Patient #1	2.74 (±1.90)	1.23 (±1.02)
Patient #2	2.50 (±1.55)	1.54 (±1.27)
Patient #3	2.55 (±2.14)	1.77 (±1.93)
Patient #4	2.05 (±1.40)	1.69 (±1.19)
Patient #5	2.16 (±1.50)	1.46 (±1.30)
Patient #6	4.46 (±2.82)	1.64 (±1.51)
Patient #7	1.33 (±1.09)	1.42 (±1.11)
Patient #8	2.24 (±2.17)	1.49 (±1.45)
Patient #9	2.82 (±2.03)	1.98 (±1.44)
Patient #10	1.88 (±1.61)	1.52 (±1.33)
Mean:	**2.47**	**1.57**

Table 4.2: Warping results using linear radial basis function.

Patient ID	Baseline Error (mm) Mean (±Std.Dev.)	Post-Warp Mean (±Std.Dev.)
Patient #1	2.74 (±1.90)	1.17 (±0.98)
Patient #2	2.50 (±1.55)	1.46 (±1.20)
Patient #3	2.55 (±2.14)	1.83 (±2.08)
Patient #4	2.05 (±1.40)	1.60 (±1.16)
Patient #5	2.16 (±1.50)	1.50 (±1.31)
Patient #6	4.46 (±2.82)	1.67 (±1.43)
Patient #7	1.33 (±1.09)	1.57 (±1.17)
Patient #8	2.24 (±2.17)	1.38 (±1.26)
Patient #9	2.82 (±2.03)	1.75 (±1.22)
Patient #10	1.88 (±1.61)	1.65 (±1.50)
Mean:	**2.47**	**1.56**

Table 4.3: Warping results using thin plate spline radial basis function.

ological variations in heart rate, heart rhythm, and respiratory patterns; however, precise quantification of these changes and their impact on the registration process is extremely difficult. In this chapter, we have explored interpolation using radial basis functions as a means to correct for these residual differences. Interpolation using radial basis functions are computationally efficient and provide a smooth warping.

As an extension to this work, the incorporation of automatic estimate of spatial support extent would reduce the manual calibration required presently. Another extension would include regularization to relax the constraints of the interpolation scheme to allow for noise or inaccurate data without causing dramatic surface curvature effects (Figure 4-2).

Figure 4-2: High curvature surface warping region. Without regularization, the radial basis functions interpolate all controll points, and this interpolate can result in regions with high surface curvature as highlighted by the orange arrows seen in the figure above. High surface curvature is typically a result of internal and external points with respect to the surface model in close proximity.

Chapter 5

Conclusions

5.1 Summary

Cardiac arrhythmias arise from disturbances in the normal generation or conduction of electrical impulses within the heart, and these disturbances can result in significant morbidity and mortality. Atrial fibrillation and ventricular tachycardia are two types of complex arrhythmias with major clinical significance. Medical therapy can suppress these arrhythmias, and medical devices such as implantable cardioversion defibrillators can provide palliative care by reacting to life-threatening cardiac rhythms. However, minimally-invasive catheter-based ablation has become a preferred and curative method to eliminate these arrhythmias in patients. These catheter-based procedures have been greatly enhanced by the used of non-fluoroscopic electroanatomical mapping systems, which allow a physician to accurately and precisely track a catheter within a patient's beating heart. While the precise catheter tracking and mapping has facilitated treatment of complex arrhythmias, mapping is a time-consuming, effort-intense, and skill-dependent operation; the resulting maps are a sparse representation of both the patient-specific anatomy and pathology. To augment catheter-mapping procedures, we proposed the integration of pre-operative MR or CT imaging information. These modalities can provide high temporal- and spatial-resolution information regarding patient-specific anatomy and pathology.

To integrate the pre-operative imaging information with the intra-operative catheter-mapping information, in Chapter 2, we described the Myo system which handles several streams of data from the electrophysiology lab. These streams include pre-operative imaging and pre-operative planning data as well as real-time electroanatomical mapping positions

from one or more mapping system, ablation information from an RF generator, electrogram information from an EP recording system, and information from remote catheter manipulations systems. The software is robust platform for visualization, manipulation, and processing of these data streams with an ultimate goal of streamlining all of this information in such as way to improve the physicians understanding of both the disease as well as his or her applied therapies.

Using the Myo system, in Chapter 3 we proposed, tested, and compared methods to quickly and accurately register or align pre-operative CT or MR imaging data with sparse electroanatomical mapping points acquired during a catheter-based electrophysiology study. Internal fiducial structures provided a useful constraint to the registration process. After evaluating several candidates, the aorta was selected as an optimal constraint. Several clinical registration were also evaluated for registration in the left atrium, left ventricle, and epicardial surface of the heart.

In Chapter 4, we presented methods for warping or deforming the pre-operative imaging data to compensate for residual errors following registration. Radial basis functions were explored because of their desirable properties. These univariate funcions provide a computational efficent means for smooth interpolation of data.

5.2 Future Work and Extensions

While this work provides a robust framework for the integration of pre-operative imaging data with real-time electroanatomical mapping data, there are several further directions for this research to be extended. As the work has developed addition interfaces to the Myo system have been created. Remote catheter manipulation is rapidly developing in cardiac electrophysiology. Furthermore, rotational angiography is promising new imaging modality being developed and used within the Myo framework.

We are currently developing a system which combines information from two electroanatomical mapping systems. The first mapping system provides highly accurate data using pulsed electromagnetic signals to triangulate the position of the catheter. The second system can localize many catheter simultaneously through determination of bioelectrical impedance differences across three orthogonal fields imposed on a patient. By combining these two mapping systems, there a several desired advantages. The system will allow for simulta-

neous visualization and tracking of multiple catheters within a patient's heart. Using the Myo system, this data can be additionally annotated with frequency mapping information or used to more quickly determine entrance and exit sites for reentrant arrhythmias.

We are also examining methods to incorporate additional information regarding the application of RF ablation lesions. Currently information is available from the RF generator including several parameters characterizing a lesion. Using this information as well as the image integration paradigm developed in this dissertation could result in a better understanding of RF ablation application within the heart. This, in turn, could reduce the likelihood of breakthrough when treating arrhythmias.

Finally, the combination of patient-specific anatomy and electroanatomical mapping information could improve understanding of arrhythmogenic circuits. First, delayed-enhancement MR imaging can provided detailed information regarding scar tissue in the left ventricle. This imaging information could be correlated with electrophysiology stuides in an attempt to image the substrate for sudden cardiac death. Furthermore, patient specific imaging information could be used to model reentrant arrhythmias such as atypical flutters or ventricular tachycardia. However, near real-time methods or approximations would be needed to make use of this information during an electrophysiology intervention.

Bibliography

[1] Zipes DP and Wellens HJ. What have we learned about cardiac arrhythmias? *Circulation*, 102:IV–52–IV57, 2000.

[2] Kilge E, Weis FC, Geotz AE, Frey L, Kesel K, Schultz A, and Lamm P. Intensive care after minimally invasive and conventional coronary surgery: a prospective comparison. *Intensive Care Med.*, 27(3):534–9, 2001.

[3] Gray H. *Henry Gray's Anatomy of the Human Body.* 1918.

[4] Hoffman BF and Rosen MR. Cellular mechanisms for cardiac arrhythmias. *Circulation Research*, 49:1–15, 1981.

[5] Haissaguerre M, Jais P, and Sah DC et al. Spontaneous initiation of atrial fibrillation by ectopic beats originating in the pulmonary veins. *N Engl J Med*, 339(10):659–666, 1998.

[6] Page RL. Newly diagnosed atrial fibrillation. *N Engl J Med*, 351(23):2408–16, 2004. treatment of afib.

[7] Go AS, Hylek EM, and et al. Phillips KA. Prevalence of diagnosed atrial fibrillation in adults: national implications for rhythm management and stroke prevention: the anticoaguation and risk factors in atrial fibrllation (atria) study. *JAMA*, 285:2370–5, 2001.

[8] Gage BF, Waterman AD, Shannon W, Boechler M, Rich MW, and Radford MJ. Validation of clinical classification schemes for predicting stroke: results from the national registry of atrial fibrillation. *JAMA*, 285:2864–70, 2001.

[9] Rockson SG and Albers GW. Comparing the guidelines: anticoagulation therapy to optimize stroke prevention in patients with atrial fibrillation. *J Am Coll Cardiol*, 43:929–35, 2004.

[10] Packer DL. Clinical presentation, investigation and management of pv stenosis complicating pv ablation for af. In *Proc. Boston Atrial Fibrillation Symposium*, 2003.

[11] Huikuri HV, Castellanos A, and Myerburg RJ. Sudden death due to cardiac arrhythmias. *N Engl J Med*, 345(20):1473–82, 2001.

[12] Josephson ME, Horowitz LN, Farshidi A, and Kastor JA. Recurrent sustained ventricular tachycardia. 1. mechanisms. *Circulation*, 57:431–440, 1978.

[13] Downar E, Harris L, Michleborough LL, Shaikh N, and Parson ID. Endocardial mapping of ventricular tachycardia in the intact human heart: evidence for reentrant mechanisms. *J Am Coll Cardiol.*, 11:783–791, 1988.

[14] Morady F, Harvey M, Kalbfleisch SJ, El-Atassi R, Calkins H, and Lanberg JJ. Radiofrequency ablation of ventricular tachycardia in patients with coronary artery disease. *Circulation*, 87:363–372, 1993.

[15] Downar E, Kimber S, Harris L, and et al. Endocardial mapping of ventricular tachycardia in the intact human heart. ii. evidence for multiuse reentry in a functional sheet of surviving myocardium. *J Am Coll Cardiol*, 20(4):869–878, 1992.

[16] Harada T, Stevenson WG, Kocovic DZ, and Friedman PL. Exploring postinfarction reentrant ventricular tachycardia with entrainment mapping. *J Am Coll Cardiol.*, 29(6):1180–1189, 1997.

[17] Lilly LS. *Pathophysiology of Heart Disease: A Collaborative Project of Medical Students and Faculty.* "Lippincott Williams & Wilkins, third edition, 2003.

[18] Cox JL, Schuessler RB, and Boineu JP. The development of the maze procedure for the treatment of atrial fibrillation. *Semin Thorac Cardiovasc Surg*, 12(1):2–14, 2000.

[19] Cox JL, Ad N, Palazzo T, Fitzpatrick S, Suyderhoud JP, DeGroot KW, Pirovic EA, Lou HC, Duvall WZ, and Kim YD. *Semin Thorac Cardiovasc Surg*, 12(1):15–19, 2000.

[20] Khargi K, Hutten BA, Lemke B, and Deneke T. Surgical treatment of atrial fibrillation: a systematic review. *European Journal of Cardio-Thoracic Surgery*, 27(2):258–65, 2005.

[21] Gillinov AM, Bakaeen F, McCarthy PM, Blackstone EH, Rajeswaran J, Pettersson G, Sabik JF, Najam F, Hill KM, Svensson LG, Cosgrove DM, Marrouche N, and Natale A. Surgery for paroxysmal atrial fibrillation in the setting of mitral valve disease: a role for pulmonary vein isolation. *The Annals of Thoracic Surgery*, 81(1):19–28, 2006.

[22] Ferguson TB. Surgical approach to atrial flutter and atrial fibrillation. In Singer I, editor, *Interventional Electrophysiology*, chapter 19. Williams and Wilkins, Baltimore, first edition, 1997.

[23] Harken AN, Horowitz LN, and Jospheson ME. Comparison of standard aneurysmectomy and aneurysmectomy with directed endocardial resection for the treatment of recurrent sustained ventricular tachycardia. *J Thorac Cardiovasc Surg*, 80:527–534, 1980.

[24] Mason JW, Stinson EB, Winkle RA, Oyer PE, Griffin JC, and Ross DL. Relative efficacy of blind left ventricular aneurysm resection for the treatment of recurrent sustained ventricular tachycardia. *Am J Cardiol*, 49:241–248, 1982.

[25] Miller JM, Kienzle MG, Harken AH, and Josephson ME. Subendocardial resection for ventricular tachycardia: Predictors for surgical success. *Circulation*, 70:624–631, 1984.

[26] Garan H, Nguyen K, McGovern B, Buckley M, and Ruskin JN. Perioperative and long-term results after electrophysiologically directed ventricular surgery for recurrent ventricular tachycardia. *J Am Coll Cardiol*, 8(1):201–209, 1986.

[27] Haines DE, Lerman BB, Kron IL, and DiMarco JP. Surgical ablation of ventricular tachycardia with sequential map-guided subendocardial resection: Electrophysiologic assessment and long-term follow-up. *Circulation*, 77:131–141, 1988.

[28] Ostermeyer J, Breithardt G, Borggrefe M, Godehardt E, Seipel L, and Bircks W. Surgical treatment of ventricular tachycardias: Complete versus partial encircling endocardial ventriculotomy. *J Thorac Cardiovasc Surg*, 87:517–525, 1984.

[29] Miller JM, Rothman SA, and Addonizio VP. Surgical techniques for ventricular tachycardia ablation. In Singer I, editor, *Interventional Electrophysiology*, chapter 20. Williams and Wilkins, Baltimore, first edition, 1997.

[30] Guiraudon GM, Thakur RK, Klein GJ, Yee R, Guiraudon CM, and Sharma A. Encircling endocardial cryoablation for ventricular tachycardia after myocardial infarction: Experience with 33 patients. *Am Heart J*, 128:982–989, 1994.

[31] Frapier JM, Hubaut JJ, Pasquie JL, and Chaptal PA. Large encircling cryoablation without mapping for ventricular tachycardia after anterior myocardial infarction: Long-term outcome. *J Thorac Cardiovasc Surg*, 116:578–583, 1998.

[32] Sanders P, Berenfeld O, Hocini M, Jais P, Vaidyanathan R, Hsu LF, Garrigue S, Takahashi Y, Rotter M, Sacher F, Scavee C, Ploutz-Snyder R, Jalife J, and Haissaguerr M. Spectral analysis identifies sites of high-freqyency activity maintain atrial fibrillation in humans. *Circulation*, 112(6):789–97, 2005.

[33] Nadamanee K, McKenzie J, Kosar E, Schwab M, Sunsaneewitayakul B, Vasavakul T, Khunnawat C, and Ngarmukos T. A new approach for catheter ablation of atrial fibrillation: mapping of the electrophysiologic substrate. *J Am Coll Cardiol*, 43(11):2044–53, 2004.

[34] Gepstein L, Hayam G, and Ben-Haim SA. A novel method for nonfluoroscopic catheter-based electroanatomical mapping of the heart in vitro and in vivo accuracy results. *Circulation*, 95:1611–1622, 1997.

[35] Ganz LI and Friedman PL. Supraventricular tachycardia. *N Engl J Med*, 332(3):162–73, 1955.

[36] Rob RA, Heffernan PB, Camp JJ, and Hanson DP. A workstation for multi-dimensional display and analysis of biomedical images. *Computer Methods and Programs in Biomedicine*, 25:169–184, 1987.

[37] Robb RA. A multidimensional biomedical image display and analysis in the biotechnology computer resource at the mayo clinic. *Machine Vision and Applications*, 1:75–96, 1988.

[38] Robb RA, Hanson DP, Karwoski RA, Larson AG, Workman EL, and Stacy MC. Analayze: a comprehensive, operator-interactive software package for multidimensional medical image display and analysis. *Computerized Medical Imaging and Graphics*, 13(6):433–454, 1989.

[39] Gering DT. A system for surgical planning and guidance using image fusion and interventional mr. Master's thesis, Massachusetts Institute of Technology, 1999.

[40] Gering DT, Nabavi A, Kikinis R, Grimson WEL, Hata N, Everett P, Jolesz F, and Wells WM. An integrated visualization system for surgical planning and guidance using image fusion and interventional imaging. *MICCAI, proceedings of second annual conference*, 1999.

[41] Pieper S, Lorensen W, Schroeder W, and Kinkinis R. The na-mic kit: Itk, vtk, pipelines, grids and 3d slicer as an open platform for the medical image computing community. *IEEE Symposium on Biomedical Imaging ISBI*, pages 698–701, 2006.

[42] Schroeder W, Martin K, and Lorensen W. *The Visualization Toolkit: An Object-Oriented Approach to 3-D Graphics.* Prentice Hall, 2004.

[43] Ibanez L, Shroeder W, Ng L, and Cates J. *The ITK Software Guide: The Insight Segmentation and Registration Toolkit.* Kitware, 2003.

[44] Halheimer MK. *Programming with Qt, 2nd edition.* O'Reilly Associates, 2002.

[45] Gamma E, Helm R, Johnson R, and Vlissides J. *Design Patterns: Elements of Reusable Object-Oriented Software.* Addison-Wesley, 1995.

[46] Shepard D. A two-dimensional interpolation function for irregularly-space data. *National Conference ACM, Proc. of 23rd*, 23:517–524, 1968.

[47] Vijaykumar R. Signal processing in cardiac electrophysiology. Master's thesis, Massachusetts Institute of Technology, 2006.

[48] Nosesworthy PA. Malchano ZJ, Ahmed J, Holmvang G, Ruskin JN, and Reddy VY. The impact of respiration on left atrial and pulmonary venous anatomy: implications for image-guided intervention. *Heart Rhythm*, 2(11):1173–8, 2005.

[49] Humold P, Vogt FM, Schmermund A, Debatin JF, Kerkhoff G, Budd T, Erbel R, Ewen K, and Barkhausen J. Radiation exposure duing cardiac ct: effective doses at multi-detector row ct and electro-beam ct. *Radiology*, 226:145–152, 2002.

[50] Cline HE and Ludke S. Magnetic resonance segmentation with the bubble wave algorithm. *Medical Imaging 2003, Proceedings of*, 5032:1658–1666, 2003.

[51] Reddy VY, Malchano ZJ, Holmvang G, Schmidt EJ, d'Avila A, Houghtaling C, Chan RC, and Ruskin JN. Integration of cardiac magnetic resonance imaging with three-dimensional electroanatomic mapping to guide left ventricular catheter manipulation: feasibility in a porcine model of healed myocardial infarction. *J Am Coll Cardiol*, 44(11):2202–13, 2004.

[52] Malchano ZJ, Chan RC, Holmvang G, Schmidt EJ, d'Avila A, Houghtaling C, Campbell LW, Ruskin JN, and Reddy VY. Real-time fusion of 3d electroanatomical cardiac mapping with contrast-enhanced cardiac mri. *SPIE Medical Imaging*, 2003.

[53] Malchano ZJ, Chan RC, Holmvang G, Schmidt EJ, d'Avila A, Brady TJ, Ruskin JN, and Reddy VY. Registration strategies for alignment of cardiac mr data with 3d electrophysiological maps. *ISMRM, 11th Scientific Meeting*, 2003.

[54] Besl PJ and McKay ND. A method for registration of 3-d shapes. *IEEE Transactions on Pattern Analysis and Machine Intelligence*, 14(2):239–256, 1992.

[55] Pulli K. *Surface reconstruction and display from range and color data.* PhD thesis, University of Washington, 1997.

[56] Rousseeuw P and von Zomeren B. Unmasking multivariate outliers and leverage points. *J American Statistical Association*, 85:633–655, 1990.

[57] Pajdla T and Gool LV. Matching of 3-d curves using semi-differential invariants. *ICCV, Proceedings of the 5th*, pages 390–395, 1995.

[58] Dalley G and Flynn P. Pair-wise range image registration: a study in outlier classification. *Computer Vision and Understanding*, 87:104–115, 2002.

[59] Brun A Estepar RSJ and Westin CF. Robust generalized total least squares iterative closest point registration. *Lecture Notes in Computer Science*, 3216:234–241, 2004.

[60] Simonetti OP, Kim RJ, Fieno DS, Hillenbrand HB, Wu E, Bundy JM, Finn JP, and Judd RM. An improved mr imaging technique for the visualizatio of myocardial infarction. *Radiology*, 218:215–23, 2001.

[61] Kim RJ, Wu E, Rafael A, Chen EL, Parker MA, Simonetti O, Klocke FJ, Bonow RO, and Judd RM. The use of contrast-enhanced magnetic resonance imaging to identify reversible myocardial dysfunction. *N Engl J Med*, 343:1445–53, 2000.

[62] Kim RJ, Fieno DS, Parrish TB, Harris K, Chan EL, Simonetti O, Bundy J, Finn JP, Klocke FJ, and Judd RM. Relationship of mri delayed contrast enhancement to irreversible injury, infarct age, and contractile function. *Circulation*, pages 1992–2002, 1999.

[63] Callans DJ, Ren JF, Michele J, Marchlinski FE, and Dillon SM. Electroanatomic left ventricular mapping in the porcine model of healed anterior myocardial infarction: Correlation with intracardiac echocardiography and pathological analysis. *Circulation*, 100:1744–50, 1999.

[64] Wrobleski D, Houghtaling C, Josephson ME, Ruskin JN, and Reddy VY. Use of electrogram characteristics during sinus rhythm to delineate the endocardial scar in a porcine model of healed myocardial infarction. *J Cardiovascular Electrophysiology*, 14(5):524–9, 2003.

[65] Sosa E, Scanavacc M, d'Avila A, and et al. A new technique to perform epicardial mapping in the electrphysiology laboratory. *J Cardiovasc Electrophysiol.*, 7:531–536, 1996.

[66] Sosa E, Scanavacca M, d'Avila A, and et al. Endocardial and epicardial ablation guided by nonsurgical transthoracic epicardial mapping to treat recurrent ventricular tachycardia. *J Cardiovasc Electrophysiol.*, 9:229–239, 1998.

[67] Sosa E, Scanavacc M, d'Avila A, and et al. Radiofrequency catheter ablation of ventricular tachycardia guided by non-surgical epicardial mapping in chronic chagasic heart disease. *PACE*. 22:128-130, 1999.

[68] Sosa E, Scanavacc M, d'Avila A, and et al. Nonsurgical transthoracic epicardial catheter ablation to treat recurrent ventricular tachycardia occuring late after myocardial infarction. *J Am Coll Cardiol.*, 35:1442–1449, 2000.

[69] d'Avila A, Scanavacca M, Sosa E, Ruskin JR, and Reddy VY. Peridcardial anatomy for the interventional electrophysiologist. *J Cardiovasc Electrphysiol*, 14:422–430, 2003.

[70] Thompson PM and Toga AW. Warping strategies for intersubject registration. In Bankman IN, editor, *Handbook of Medical Imaging*, chapter 36, pages 569–599. Academic Press, first edition, 2000.

[71] Carr JC, Fright R, and Beatson RK. Surface interpolation with radial basis functions for medical imaging. *IEEE Transactions on Medical Imaging*, 16(1):96–107, 1997.

[72] Bookstein FL. Principle warps: Thin-plate splines and the decomposition of deformations. *IEEE Transactions Pattern Analysis and Machine Intelligence*, 11(6):567–585, 1989.

[73] Fornefett M, Rohr K, and Stiehl HS. Radial basis functions with compact support for elastic registration of medical images. *Image and Vision Computing*, 19(1-2):87–96, 2001.

[74] Barré S, Fernandez C, Paume P, and Subrenat G. Simulating facial surgery. In *Visual Data Exploration and Anlysis VII, Proc. of SPIE*, volume 3960, pages 334–45, 2000.

[75] Barré S, Fernandez C, Paume P, and Subrenat G. Three-dimensional visualization as an aid for facial surgical planning. In *Visualization, Display, and Image-Guided Procedures, Proc. of SPIE*, volume 4319, pages 252–263, 2001.